Turun yliopisto
University of Turku

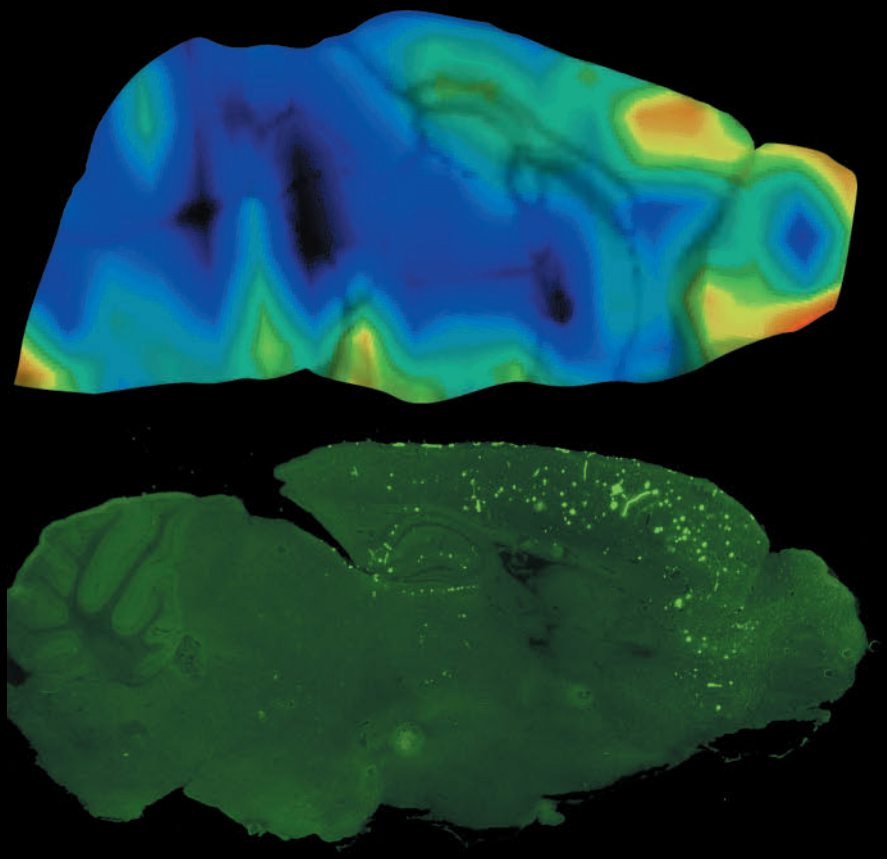

IMAGING ALZHEIMER'S DISEASE BETA-AMYLOID PATHOLOGY IN TRANSGENIC MOUSE MODELS USING POSITRON EMISSION TOMOGRAPHY

Anniina Snellman

TURUN YLIOPISTON JULKAISUJA – ANNALES UNIVERSITATIS TURKUENSIS
Sarja - ser. D osa - tom. 1294 | Medica - Odontologica | Turku 2017

Turun yliopisto
University of Turku

IMAGING ALZHEIMER'S DISEASE BETA-AMYLOID PATHOLOGY IN TRANSGENIC MOUSE MODELS USING POSITRON EMISSION TOMOGRAPHY

Anniina Snellman

TURUN YLIOPISTON JULKAISUJA – ANNALES UNIVERSITATIS TURKUENSIS
Sarja - ser. D osa - tom. 1294 | Medica - Odontologica | Turku 2017

University of Turku

Faculty of Medicine
Department of Clinical Physiology and Nuclear Medicine
Drug Research Doctoral Programme
Turku PET Centre
MediCity Research Laboratory

Supervised by

Adjunct Professor Merja Haaparanta-Solin, PhD
Turku PET Centre
University of Turku
Turku, Finland

Professor Olof Solin, PhD
Turku PET Centre
University of Turku
Turku, Finland

Professor Juha O. Rinne, MD, PhD
Turku PET Centre
Turku University Hospital and
University of Turku, Turku, Finland

Reviewed by

Dr. Hervé Boutin, PhD
Wolfson Molecular Imaging Centre
University of Manchester
Manchester, United Kingdom

Professor Heikki Tanila, MD, PhD
A.I. Virtanen Institute
University of Eastern Finland
Kuopio, Finland

Opponent

Dr. Sylvie Chalon, PhD
Inserm U930, Imaging and Brain
University of Tours
Tours, France

Cover: Anniina Snellman

The originality of this thesis has been checked in accordance with the University of Turku quality assurance system using the Turnitin OriginalityCheck service.

ISBN 978-951-29-6865-7 (PRINT)
ISBN 978-951-29-6866-4 (PDF)
ISSN 0355-9483 (Print)
ISSN 2343-3213 (Online)
Painosalama Oy - Turku, Finland 2017

To my family

ABSTRACT

Anniina Snellman

IMAGING ALZHEIMER'S DISEASE BETA-AMYLOID PATHOLOGY IN TRANSGENIC MOUSE MODELS USING POSITRON EMISSION TOMOGRAPHY

University of Turku
Faculty of Medicine
Department of Clinical Physiology and Nuclear Medicine
Drug Research Doctoral Programme
Turku PET Centre
MediCity Research Laboratory

Accumulation of beta-amyloid (Aβ) in the brain is known to have an important role in the complex chain of pathological events leading to Alzheimer's disease (AD). Based on current knowledge, Aβ is also seen as an interesting target for novel disease modifying therapies. Non-invasive and quantitative imaging of transgenic mouse models of AD by positron emission tomography (PET) would represent an ideal translational approach for evaluation of novel Aβ targeted therapeutics *in vivo* already during the preclinical phase of drug development.

The aim of this thesis was to evaluate the suitability of Aβ targeted PET tracers, [^{11}C]PIB and [^{18}F]flutemetamol, for small animal PET imaging and for longitudinal follow-up of β-amyloidosis in three AD mouse models, i.e. transgenic APP23, Tg2576 and APP_{swe}-$PS1_{dE9}$ mice. In addition, the effects of novel functionalized Aβ targeted nanoliposomes, known as mApoE-PA-LIPs, were investigated in APP23 mice exploiting longitudinal [^{11}C]PIB PET imaging.

A temporal increase in tracer retention reflecting increased Aβ-deposition could be detected *in vivo* only in the APP23 mouse model. Both tracers specifically bound Aβ in mouse brain sections, however, the higher non-specific binding of [^{18}F]flutemetamol to the white matter structures limited its sensitivity in comparison to [^{11}C]PIB. In the APP23 model, the mApoE-PA-LIP treatment showed a trend to reduce the increase in the [^{11}C]PIB binding ratios as compared to the saline-treated group; in addition, the binding ratios correlated well with the histologically-assessed amyloid load, further validating the method.

In summary, these results demonstrate that [^{11}C]PIB binding is a valid biomarker of Aβ deposition in the APP23 mouse – an animal model that expresses abundant, large and congophilic Aβ deposits. However, the sensitivity of the method is not sufficient for use in animal models with lower plaque loads and different plaque morphologies, nor does it seem capable of detecting early pathological changes in young AD mice.

Keywords: beta-amyloid, Alzheimer's disease, positron emission tomography, amyloid imaging, PET, [^{11}C]PIB, [^{18}F]flutemetamol, drug development

TIIVISTELMÄ

Anniina Snellman

BEETA-AMYLOIDIPATOLOGIAN PET-KUVANTAMINEN ALZHEIMERIN TAUDIN MUUNTOGEENISISSÄ ELÄINMALLEISSA

Turun yliopisto
Lääketieteellinen tiedekunta
Kliininen fysiologia ja isotooppilääketiede
Lääketutkimuksen tohtoriohjelma
Valtakunnallinen PET-keskus
MediCity-tutkimuslaboratorio

Alzheimerin taudin amyloidihypoteesin mukaan aivoihin kertyvällä beeta-amyloidilla (Aβ) on tärkeä rooli monimutkaisessa patologisten muutosten tapahtumaketjussa, joka johtaa lopulta hermosolukatoon, kognitiivisiin häiriöihin ja dementiaan. Positroniemissiotomografia (PET) on kajoamaton isotooppilääketieteen menetelmä, joka mahdollistaa Aβ-kertymien kuvantamisen elävässä tutkimuskohteessa. Pieneläinten PET-kuvantamisen ja Alzheimerin taudin muuntogeenisten eläinmallien avulla uusien Aβ-patologiaan vaikuttavien lääkkeiden tehokkuutta olisi mahdollista arvioida kajoamattomalla menetelmällä *in vivo* myös lääkekehityksen prekliinisessä vaiheessa.

Tämän tutkimuksen tavoitteena oli arvioida kahden Aβ-kertymiin sitoutuvan PET-merkkiaineen, [^{11}C]PIB:n ja [^{18}F]flutemetamolin, soveltuvuutta pieneläinkuvantamiseen ja patologisten muutosten seuraamiseen muuntogeenisilla APP23, Tg2576 ja APP_{swe}-$PS1_{dE9}$ hiirimalleilla. Lisäksi seurattiin uusien Aβ-kertymiin kohdennettujen nanoliposomien (mApoE-PA-LIP) vaikutuksia muuntogeenisten APP23-hiirten aivojen Aβ-kertymään [^{11}C]PIB PET-kuvantamisen avulla *in vivo*.

Merkkiainekertymän kasvua hiirten vanhetessa ja Aβ-kertymien määrän lisääntyessä pystyttiin seuraamaan molemmilla merkkiaineilla toistuvin *in vivo* PET-kuvauksin, mutta ainoastaan APP23-hiirimallissa. Molempien merkkiaineiden havaittiin sitoutuvan spesifisesti immunohistokemiallisesti varmistettuihin Aβ-kertymiin hiirten aivoleikkeillä, tosin [^{18}F]flutemetamolin voimakkaampi epäspesifinen sitoutuminen aivojen valkeaan aineeseen heikensi sen herkkyyttä verrattuna [^{11}C]PIB:iin. mApoE-PA-LIP-hoito johti APP23 hiirimallilla hitaampaan [^{11}C]PIB-kertymän kasvuun kontrolliryhmään verrattuna ja sitoutumissuhteet korreloivat hyvin immunohistokemiallisesti määritetyn Aβ-kertymän kanssa.

Tutkimuksen tulokset osoittavat, että aivojen [^{11}C]PIB-kertymä on luotettava biomarkkeri Aβ-patologian seuraamiseen APP23-hiirimallilla, joka ilmentää huomattavia määriä suuria ja tiiviitä Aβ-kertymiä. Menetelmän herkkyys ei kuitenkaan riitä havaitsemaan varhaisia Aβ-patologian muutoksia nuorilla hiirillä eikä kertymien lisääntymistä niillä hiirimalleilla, joilla kertymien määrä on pienempi ja rakenne on erilainen.

Avainsanat: beeta-amyloidi, Alzheimerin tauti, positroniemissiotomografia, PET, amyloidikuvantaminen, [^{11}C]PIB, [^{18}F]flutemetamoli, lääkekehitys

TABLE OF CONTENTS

ABBREVIATIONS

3D-OSEM	Three-dimensional ordered-subsets expectation maximization
[^{11}C]PIB	[^{11}C]Pittsburgh compound B
[^{18}F]FDG	2-deoxy-2-[^{18}F]fluoro-D-glucose
μPET	PET instrumentation for small animal imaging
Aβ	Beta-amyloid
AD	Alzheimer's disease
AICD	APP intracellular domain
ApoE	Apolipoprotein E
APP	Amyloid precursor protein
AChE	Acetylcholinesterase
AChEI	Acetylcholinesterase inhibitor
BBB	Blood-brain barrier
B/F	Bound-to-free ratio
BSA	Bovine serum albumin
CB	Cerebellum
CNS	Central nervous system
CSF	Cerebrospinal fluid
CT	Computed tomography
DVR	Distribution volume ratio
ELISA	Enzyme linked immunosorbent assay
EMA	European Medicines Agency
EOAD	Early onset Alzheimer's disease
FAD	Familial Alzheimer's disease
FBP	Filtered back projection
FC	Frontal cortex
FDA	Food and Drug Administration
HC	Hippocampus
Iba-1	Ionized calcium binding adaptor molecule 1
IF	Immunofluorescence
IHC	Immunohistochemistry
i.p.	Intraperitoneal
i.v.	Intravenous
K_d	Equilibrium dissociation constant
LIP	Liposome
LOAD	Late onset Alzheimer's disease
LRP-1	Low density lipoprotein receptor-related protein 1
MAPT	Microtubule associated protein tau
mApoE	Peptide residue modified from receptor binding domain of ApoE
MCI	Mild cognitive impairment
MRI	Magnetic resonance imaging

NC	Neocortex
NMDA	N-methyl-D-aspartate
NFT	Neurofibrillary tangle
NP	nanoparticle
p.i.	Post-injection
PA	Phosphatidic acid
PBS	Phosphate buffered saline
PET	Positron emission tomography
PO	Pons
PSEN	Presenilin
PSL/mm^2	Photo-stimulated luminescence per square millimeter
PVE	Partial volume effect
PVEC	Partial volume effect correction
RAGE	Receptor for advanced glycation end products
ROI	Region of interest
SA	Specific activity
sAPP	Secreted amyloid precursor protein
SPECT	Single-photon emission computed tomography
SUV	Standardized uptake value
TAC	Time-radioactivity curve
TLC	Thin layer chromatography
tg	Transgenic
ThS	Thioflavine S
VOI	Volume of interest
wt	Wild type

LIST OF ORIGINAL PUBLICATIONS

This thesis is based on the following four original publications, which are referred to in the text by their Roman numerals (**I–IV**).

I. **Snellman A***, Rokka J*, Lopez-Picon FR, Eskola O, Wilson I, Farrar G, Scheinin M, Solin O, Rinne JO, Haaparanta M. *Evaluation of amyloid imaging agent [^{18}F]flutemetamol in rodents: Pharmacokinetics and binding to amyloid deposits in mouse model of Alzheimer's disease.* Eur J Nucl Med Mol Imaging 2012; 39, 1784-95. *Equal contribution

II. **Snellman A**, López-Picón FR, Rokka J, Salmona M, Forloni G, Scheinin M, Solin O, Rinne JO, Haaparanta-Solin M. *Longitudinal amyloid imaging in mouse brain with ^{11}C-PIB: comparison of APP23, Tg2576, and APPswe-PS1dE9 mouse models of Alzheimer disease.* J Nucl Med. 2013;54(8):1434-41.

III. **Snellman A**, Rokka J, López-Picón FR, Eskola O, Salmona M, Forloni G, Scheinin M, Solin O, Rinne JO, Haaparanta-Solin M. *In vivo PET imaging of beta-amyloid deposition in mouse models of Alzheimer's disease with a high specific activity PET imaging agent [^{18}F]flutemetamol.* EJNMMI Research 2014;4:37.

IV. **Snellman A**, Rokka J, López-Picón FR, Helin S, Francesca Re, Löyttyniemi E, Pihlaja R, Forloni G, Salmona M, Masserini M, Solin O, Rinne JO, Haaparanta-Solin M. *Applicability of [^{11}C]PIB micro-PET imaging for in vivo follow-up of anti-amyloid treatment effects in APP23 mouse model.* Neurobiology of Ageing, in press.

In addition, some unpublished data are presented.

1. INTRODUCTION

Alzheimer's disease (AD) is a neurodegenerative disorder that begins with alterations in cognitive functions and ends with the patient suffering severe dementia and ultimately his or her death. The global prevalence of AD and other dementias is estimated today to number 36 million (Prince et al., 2013), and the amount of AD patients is predicted to triple to about 115 million in 2050 unless novel preventive or disease-modified medications can be introduced (Wimo et al., 2014). Alzheimer's disease is characterized by two key neuropathological processes in the brain: Accumulation of extracellular amyloid deposits composed of aggregated beta-amyloid (Aβ) peptides and intracellular formation of neurofibrillary tangles (NFT) consisting of hyperphosphorylated forms of the microtubule binding protein tau. The amyloid hypothesis presented already in the 1990s, postulated that Aβ deposition initiates the disease process, ultimately leading to other downstream changes such as NFT, synaptic defects, alterations in neurotransmitter systems, neuroinflammation and ultimately neuronal death (Hardy and Higgins, 1992).

Positron emission tomography (PET) is a non-invasive nuclear imaging method that allows the detection and temporal monitoring of various physiological and pathophysiological processes. PET method and generation of specific PET tracers by incorporating a positron emitting radionuclide, such as ^{11}C or ^{18}F, to a molecule targeting e.g. brain receptor systems, neurotransmitter transporters, inflammatory responses or pathological structures, have made it possible to obtain quantitative functional information about ongoing pathological alterations in the brain in different diseases non-invasively. In the cases of AD and mild cognitive impairment (MCI), PET imaging and targeting Aβ deposits with specific PET tracers, such as [^{11}C]Pittsburgh compound B ([^{11}C]PIB) and [^{18}F]flutemetamol, offer valuable tool for investigating Aβ pathology *in vivo* (Klunk et al., 2004; Koivunen et al., 2008; Li et al., 2008), for temporal monitoring of pathological changes (Kemppainen et al., 2014; Ossenkoppele et al., 2012; Scheinin et al., 2009), and for evaluation of novel Aβ targeted therapies (Rinne et al., 2010). Positive amyloid PET findings have been shown to correlate with Aβ pathology confirmed by brain biopsies (Leinonen et al., 2008; Rinne et al., 2012), and can thus be considered as a specific biomarker for Aβ deposition. As a result, amyloid PET has recently been added to the advanced research diagnostic criteria for AD proposed by the International Working Group (IWG-2) (Dubois et al., 2014).

When novel PET tracers are being developed for clinical purposes, initially the pharmacokinetic ADME profile (adsorption, distribution, metabolism and excretion) and binding to target molecules are investigated with *in vitro* methods, followed by *ex vivo* tests in experimental animals. Nowadays, PET systems have also been developed for small animal imaging (μPET) making possible *in vivo* animal experiments which can provide quantitative data and full kinetic profiling of the tracer over time in a single animal and permit longitudinal follow-up studies. Small animal PET imaging combined with Aβ targeted PET tracers would thus be a valuable tool in the preclinical development of novel anti-amyloid compounds, allowing non-invasive, quantitative and longitudinal evaluation of treatment effects in transgenic (tg) animal models. Even though early studies using tg animal models of AD and μPET generated contradictory information about the usability of this approach (Klunk et al., 2005; Maeda et al., 2007; Toyama et al., 2005), recently, cerebral Aβ accumulation has been successfully followed in various mouse models using [^{11}C]PIB and different ^{18}F-labeled Aβ targeting PET tracers (Manook et al., 2012; Poisnel et al., 2012; Rominger et al., 2013; Sérrière et al., 2015).

In AD, the pathological alterations in the brain have been shown to begin decades before the onset of clinical symptoms (Jack et al., 2013); unfortunately, the underlying causes and mechanisms are still not understood in detail and currently available medication can only retard the progression and relieve clinical symptoms of the disease. Despite vigorous research efforts to find novel therapeutic targets and ways to affect the underlying pathology, there is still no drug that would tackle the disease process (Doody et al., 2014; Eli Lilly and Company, 2016; Salloway et al., 2014). One novel therapeutic approach has been the design of functionalized nanoparticles targeting Aβ. Nanoparticles are more commonly used in brain drug delivery (Masserini, 2013; Saraiva et al., 2016) but recently, functionalized liposomes (LIPs) targeting Aβ have also been tailored for AD treatment (Balducci et al., 2014; Bana et al., 2014; Mancini et al., 2016; Re et al., 2011). These LIPs have been incorporated with a peptide residue derived from the receptor binding domain of apolipoprotein E (mApoE) to enhance the blood-brain barrier (BBB) penetration, and phosphatidic acid (PA) that has been shown previously to bind and disaggregate $A\beta_{42}$ *in vitro* (Bana et al., 2014; Gobbi et al., 2010). *In vivo*, these LIPs have been shown to cross the BBB, lower the Aβ load in the brain, increase its efflux from the brain and clearance in the periphery, and restore specific memory functions in a mouse model of AD (Balducci et al., 2014; Mancini et al., 2016).

The aim of this thesis work was to investigate the possibility to exploit μPET and tg mouse models in the evaluation of novel anti-amyloid treatments in the preclinical phase of the drug discovery process. The present thesis describes full preclinical characterization and pharmacokinetic profiling of two Aβ targeted PET tracers, i.e. [^{11}C]PIB and [^{18}F]flutemetamol, in experimental animals (**I**). In addition, longitudinal follow-up of cerebral Aβ deposition was performed in three different tg AD mouse models using both tracers (**II–III**). Subsequently, quantitative follow-up of treatment effects of novel Aβ targeted mApoE-PA-LIPs were performed in a tg AD mouse model utilizing μPET imaging (**IV**). The relationships of **I–IV** to each other are presented in Figure 1.

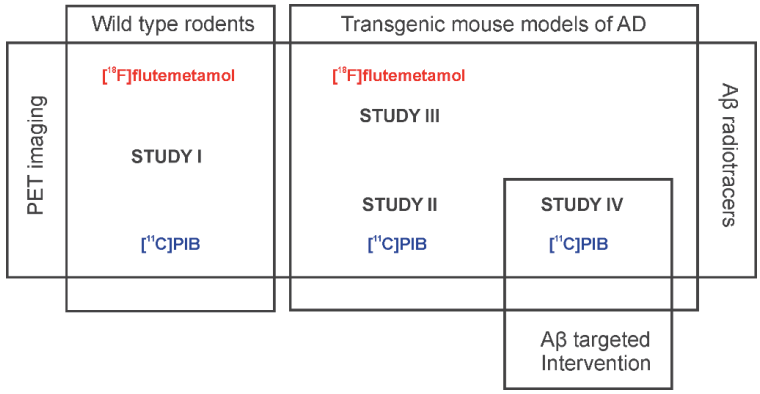

Figure 1. Relationship of studies **I–IV** to each other.

2. REVIEW OF THE LITERATURE

2.1. Alzheimer's disease

> "Nov 26, 1901.
>
> She sits on her bed with a helpless expression. What is your name? *Auguste*. Last name? *Auguste.* What is your husband's name? *Auguste, I think.* Your husband? *Ah, my husband.* She looks las if she didn't understand the question. Are you married? *To Auguste.* Mrs D? *Yes, yes, Auguste D.* How long have you been here? She seems to be trying to remember. *Three weeks.* --- When objects are shown to her, she does not remember after a short time which objects have been shown. --- When asked to write Auguste D she tries to write Mrs and forgets the rest. It is necessary to repeat every word…."
>
> Alzheimer's original notes (as quoted in Maurer et al., 1997)

AD was first described over 100 years ago by Alois Alzheimer, who presented the case of "Auguste D", a 51-year-old woman who had suffered a progressive cognitive impairment, hallucinations, delusions and histopathological lesions now known as Aβ plaques and NFTs (Maurer et al., 1997). AD is the most common neurodegenerative disease causing dementia, accounting for 60−70% of all cases, however, its complex and multifactorial pathological process is still partly unresolved in its molecular details (Blennow et al., 2006). Based on the revised clinical criteria, AD is characterized by three distinct phases; at first, a long and asymptomatic *preclinical phase*, when pathological processes in the brain are ongoing but clinical signs of the disease are missing, the subsequent *prodromal AD stage* with mild clinical symptoms usually not severe enough to meet the diagnosis criteria, and finally, the *AD dementia phase* (Dubois et al., 2014; McKhann et al., 2011). The AD dementia phase can be further divided into mild, moderate and severe AD according to the severity of the observed clinical symptoms.

The initial AD symptoms usually include difficulties in remembering new information, confusion about time and location, difficulties in finding words, understanding visual tasks and spatial relationships, and changes in personality seen as aggression, depression or even delusions (Alzheimer's Association, 2015). As the disease progresses, cognitive and functional abilities decline, the patient faces difficulties in performing even simple daily tasks and further loses the ability to remember places leading to him or her getting lost also in familiar environments. In the final severe phase of AD, patients are unable to handle daily activities alone, lose their ability to communicate and recognize their loved-ones, and become physically restricted. This further increases the risk of infections that often contributes to the death of AD patients (Alzheimer's Association, 2015).

2.1.1. *Pathogenesis*

Pathogenesis of AD is a complex interplay of various processes, and the causal and temporal relationship between them is still not understood in detail. However, in general, AD pathology can be divided into three types of lesions; lesions related to accumulation of proteins, lesions due to

changes in reactive processes, and lesions due losses of neurons and synapses (Duyckaerts et al., 2009).

Aβ deposition

Aβ plaques are extracellular protein deposits that are formed by the aggregation of Aβ peptide fragments. Neuritic plaques are composed of dense amyloid core surrounded by activated microglia, reactive astrocytes, and dystrophic neurites with NFTs (Fig. 2). Neuritic plaques are thought to be the pathologically relevant form of amyloid, but also diffuse deposits lacking a focal amyloid core, neuritic corona and gliosis, are present in large numbers (Braak et al., 1989). The Aβ deposition in the brain is initially found exclusively from the neocortex (NC), and its progression to other brain regions can be divided into five different phases (Fig. 3) (Thal et al., 2002). However, inter-individual variation is high in the early stages, making it difficult to evaluate the disease process based on the level of Aβ deposition.

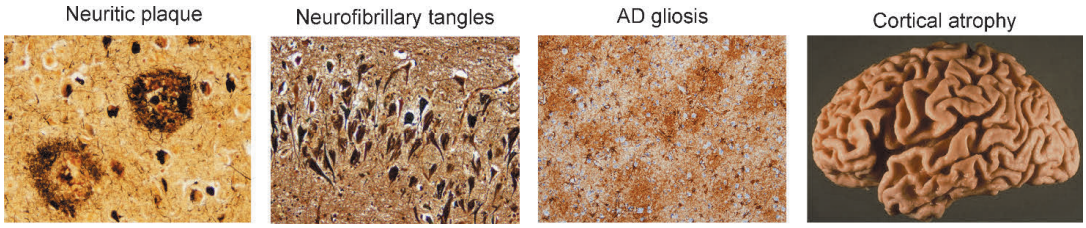

Figure 2. Pathological alterations in Alzheimer's disease. Alzheimer's disease is characterized by the accumulation of beta-amyloid into extracellular plaques and tau protein into intracellular neurofibrillary tangles. In addition, abundant gliosis is seen in the brain, in association with the plaque pathology. In advanced stages of the disease, macroscopic brain atrophy and enlargement of ventricles can be seen as a result of ongoing neuronal loss. Images were obtained from: http://neuropathology-web.org/chapter9/chapter9bAD.html#ad (9.12.2016).

Neurofibrillary changes

Tau proteins are members of the microtubule-associated protein family, and are normally expressed in neurons, where they have an important physiological role in maintaining the neuronal microtubule network (Buee et al., 2000). Intraneuronal neurofibrillary changes in AD, i.e. NFT in the cell soma, neuropil threads in the dendrites, and dystrophic neurites associated with senile plaques (Braak and Braak, 1997), are composed of paired helical filaments containing mainly hyper-phosphorylated tau proteins (Fig. 2). Even though NFTs are one of the pathological hallmarks of AD, abnormal tau aggregates are not specific for AD since they can also be found in young and non-demented individuals as well as in patients with other tauopathies, such as frontotemporal dementia, Lewy body disease and Parkinson's disease (Braak and Del Tredici, 2015; Tomlinson et al., 1968). In contrast to Aβ deposition, the distribution of NFTs in AD brain is highly characteristic with little inter-individual variation, and its progression has been divided into six different stages I−VI (Fig. 3)(Braak and Braak, 1991). Neuropathological evaluations have revealed that the early tau pathology in stages I−II precedes the Aβ pathology (Braak and Braak, 1997), and pre-tangle material has been recently found even in the brains of young individuals under 30 years (Braak and Del Tredici, 2015). Even after years of intense research, the molecular mechanisms linking Aβ and tau pathology have still not been resolved in detail.

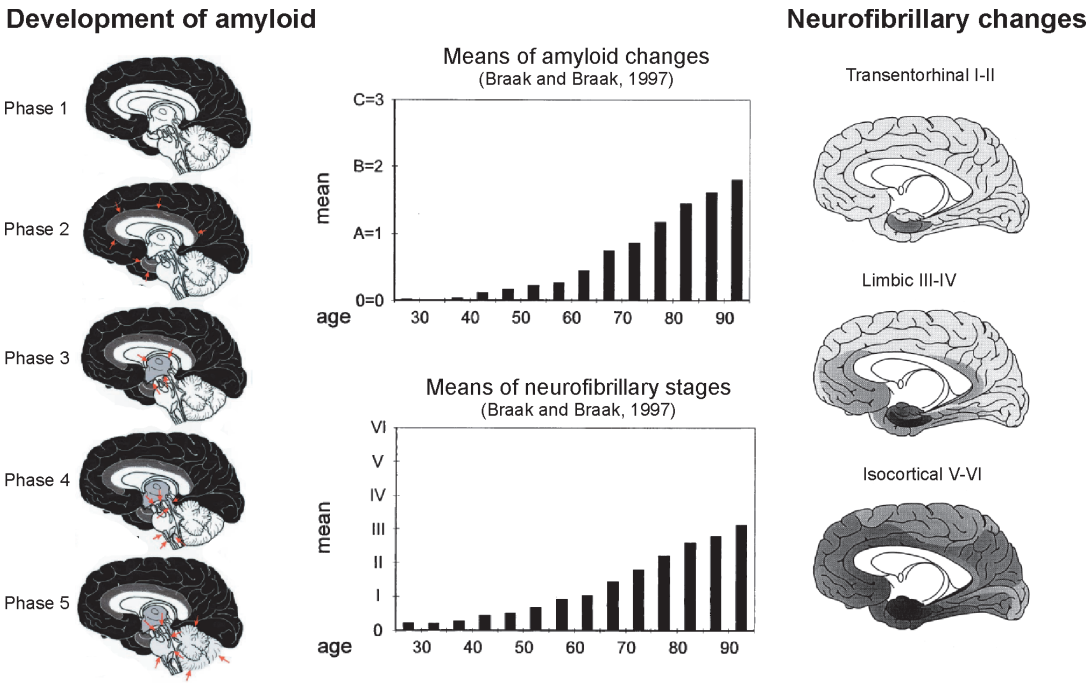

Figure 3. Development of β-amyloidosis (phases 1−5) and neurofibrillary changes (stages I−VI) in Alzheimer's disease. Aβ deposition begins from the neocortex (phase 1), further evolving to the allocortex (phase 2), subcortical structures (phases 3−4) and finally to cerebellum (phase 5). Neurofibrillary changes begin from the transentorhinal cortex, spreading to the hippocampus, and finally to other parts of the isocortex. Both changes increase with age, but stage I neurofibrillary changes can develop early and in the absence of Aβ pathology. Image modified from Braak and Braak, 1997 and Thal et al., 2002.

Inflammation

Abundant gliosis is one characteristic of AD brain (Fig. 2), and inflammatory processes are closely associated with Aβ pathology. Microglia cells and astrocytes can bind soluble forms of Aβ, which promotes the secretion of pro-inflammatory cytokines and chemokines. In addition, these immune cells can participate in the clearance of Aβ fibrils by phagocytosis (Heneka et al., 2015). However, controversial views about inflammation in AD exist, as the processes have been viewed either as damaging or beneficial (Boche and Nicoll, 2008). Recent research has suggested that inflammatory processes in AD brain are not simply a result of the neuritic plaques, but that they may actually actively participate in the disease pathology (Heneka et al., 2015). This is supported by the finding that many of the novel risk genes for sporadic AD are related to the innate immune system. It has also been speculated that the relationship between Aβ and tau pathologies would not be direct, but rather mediated through pro-inflammatory processes (Hardy et al., 2014).

Neuronal loss and synaptic changes

As the disease progresses, macroscopic structural changes in specific anatomical locations become also apparent in AD brain. The brain atrophy typical for AD is more prominent in areas rich in NFT pathology, i.e. hippocampus (HC) and entorhinal cortex (Karow et al., 2010), and it correlates well with the neuronal loss (Kril et al., 2004), NFT pathology (Whitwell et al., 2008), but not with the Aβ

burden (Josephs et al., 2008). In a neuroimaging study using structural magnetic resonance imaging (MRI), the largest effects were detected in the HC in AD (-20%) and MCI (-11%) in comparison to healthy controls (Karow et al., 2010). In the late AD stages where a severe cognitive decline is already present, atrophy becomes detectable also in frontal cortex (FC), whereas sensory and motor cortices remain unaffected (Thompson et al., 2003).

2.1.2. *Risk and protective factors*

Genetic risk factors

Two distinct forms of AD are recognized based on their genetic etiology and age of onset; the inherited or early-onset (< 65 years) AD (EOAD), and sporadic or late-onset (> 65 years) AD (LOAD). To date, autosomal dominant mutations in three genes coding for amyloid precursor protein (APP), presenilin-1 (PSEN1) or presenilin-2 (PSEN2), have been identified in EOAD (Goate et al., 1991; Levy-Lahad et al., 1995; Sherrington et al., 1995). The mutations in APP are located at, or in close proximity to secretase binding sites or inside the Aβ sequence, favoring APP metabolism via the amyloidogenic pathway (discussed more detailed in chapter 2.2.1) and the production of longer Aβ peptide forms which are more prone to aggregation (Wisniewski et al., 1991). LOAD is the most common form of AD accounting for more than 95% of affected cases. LOAD is suspected to have a multifactorial origin, with a combined genetic and environmental input. Unlike in EOAD, the susceptibility genes associated with LOAD are not causative, but only increase the risk of disease. Until recently, the only identified genetic risk factor for LOAD was the apolipoprotein E (ApoE) ε4 allele. However, recent large genome-wide association studies have identified single nucleotide polymorphisms in over 20 novel loci with significant associations to LOAD (For a review, see e.g. Rosenthal and Kamboh, 2014), leading to identification of three pathways explaining the genetic variability in relation to increased risk for AD: (i) endosomal vesicle recycling, (ii) cholesterol metabolism and (iii) the innate immune system (Hardy et al., 2014).

Non-genetic risk factors and protective factors

The greatest risk factor of LOAD is *age*, as most of the AD patients receive a clinical diagnosis at the age of 65 or older. Even in the absence of the causative EOAD genes, also *family history* of AD has been found to increase an individual's risk (Green et al., 2002). *MCI* has been suggested to be the preceding stage to AD; however, even though MCI increases the risk for AD, all persons with MCI do not convert (Jicha et al., 2006). In addition, *traumatic brain injury* and several *cardiovascular risk factors*, such as infarcts, hypertension, hypercholesterolemia, smoking, diabetes, and obesity in midlife are also viewed as risk factors for AD (Kivipelto et al., 2001; Kivipelto et al., 2006; Reitz and Mayeux, 2014). In population based cohort studies, also *type 2 diabetes* was seen to approximately double the risk of AD (Leibson et al., 1997; Ott et al., 1999).

In a recent analysis of population-based data, a third of AD cases were estimated to be caused by seven potentially modifiable risk-factors: low education, midlife hypertension, midlife obesity, diabetes, physical inactivity, smoking and depression (Norton et al., 2014). On the contrary, factors that benefit the overall health and heart, such as physical activity, healthy diet high in fish, fruits and vegetables and low in red meat, high education and active lifestyle have been postulated to exert a protecting effect on brain health (Reitz and Mayeux, 2014).

2.1.3. *Diagnostic criteria and biomarkers for early detection*

The diagnosis of probable and possible AD relies largely on clinical examination, and the presence of gradually worsening deficits in cognitive functions, however, confirmatory histopathological evidence of AD pathology from autopsy is still needed for verification of the AD diagnosis (McKhann et al., 2011). To date, also a third classification as "probable (or possible) AD dementia with evidence of the AD pathophysiological processes" has been added for research purposes and clinical trials. For this reason, different biomarkers for AD pathophysiology have been included into the diagnostic criteria (McKhann et al., 2011).

Biomarkers that reveal the presence of Aβ or tau pathology in the brain can be referred to as *diagnostic biomarkers*. These markers, such as cerebrospinal fluid (CSF) $A\beta_{42}$, CSF total tau (t-tau) or phosphorylated tau (p-tau), amyloid PET and possibly tau PET in the future, possess the necessary specificity for diagnosing AD at any stage of the disorder, including the early asymptomatic stages. These markers appear abnormal in the earliest phases; however, they might not correlate well with the clinical severity of AD (Dubois et al., 2014; Jack et al., 2013). In biomarker-autopsy correlation studies, a decrease in CSF $A\beta_{42}$ levels and positive amyloid PET scans correlated with Aβ deposition in the brain, whereas an increase in CSF t-tau and p-tau levels was associated with the NFT burden (Ikonomovic et al., 2008; Tapiola et al., 2009).

Pathological biomarkers of AD include the markers reflecting ongoing neuronal damage rather than specific AD pathophysiological processes. These markers include structural brain changes, particularly hippocampal atrophy assessed by MRI, and cortical metabolic alterations evaluated by 2-deoxy-2-[^{18}F]fluoro-D-glucose ([^{18}F]FDG) PET. Similar to brain atrophy discussed before, [^{18}F]FDG hypometabolism is associated with the NFT burden, but not with the Aβ load (Jack et al., 2013). Even though pathological biomarkers can be considered to reflect tau related neurodegeneration, they do not possess the specificity needed for AD diagnosis and they might not be present in the earlier phases of the disease. Nevertheless, they can be used for evaluating the severity and progression of the disease and determination of the various disease stages. The model proposed by Jack and colleagues (Jack et al., 2013; Jack et al., 2010) for dynamic biomarker changes in the course of AD is illustrated in Figure 4.

At present, early diagnosis offers only limited benefits, due to the absence of disease modifying drugs. In addition, individuals with similar biomarker profiles have been found to experience differing clinical outcomes, depending on the underlying risk or protective factors. However, early diagnosis offers possibilities for treatment planning, family support and possibilities for individuals themselves to participate in the decision-making about their own medical care before suffering a drastic decline in their cognitive abilities (Prince et al., 2011). In addition, novel disease modifying drugs are likely to have better effects in the pre-symptomatic phases of AD. The identification of a battery of biomarkers has also importance for the planning and conducting of the secondary preventive clinical trials (Sperling et al., 2011).

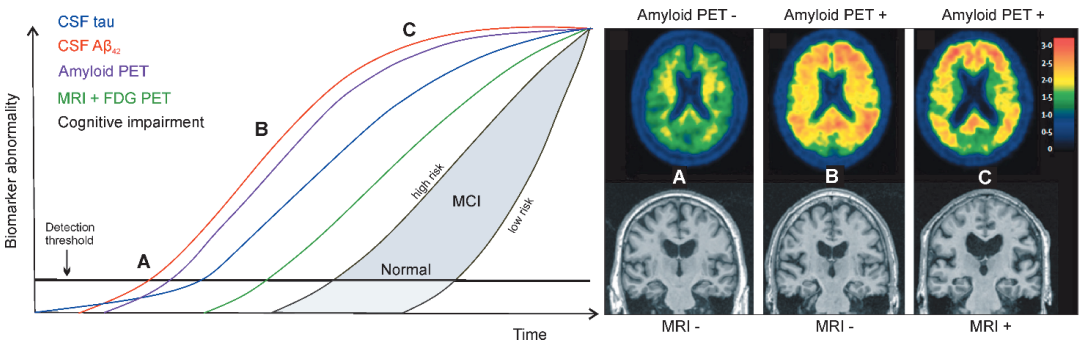

Figure 4. Hypothetical model for dynamic biomarker changes during the progression of Alzheimer's disease. Lowered $A\beta_{42}$ concentrations in the cerebrospinal fluid (CSF) and positive amyloid PET imaging are the first detected abnormalities. Tau pathology is suggested to precede amyloid pathology in the early phases, however, biomarker abnormalities are below threshold levels at this point. In the later stages, brain atrophy detected by magnetic resonance imaging (MRI) and cortical hypometabolism detected with fluorodeoxyglucose (FDG) PET represent ongoing neurodegeneration. Cognitive impairment begins only when all biomarkers already show abnormalities, however, the curve is presented as a zone, where two individuals with similar biomarker profile can have different clinical outcome depending on the underlying risks and protective factors. Modified from Jack et al., 2013 and Jack et al., 2010. Aβ = beta-amyloid; MCI = mild cognitive impairment.

2.2. The role of Aβ in Alzheimer's disease

2.2.1. *Processing of APP to Aβ*

APP, a type I glycosylated transmembrane protein, is the precursor of the Aβ peptide (Kang et al., 1987). It is expressed in all tissues in multiple sub-cellular locations: the Golgi, trans-Golgi network, endosomes and plasma membrane (for a review, see e.g. Claeysen et al., 2012). Its normal physiological function still remains unclear, however, based on its structure, it could serve as a cell-surface receptor (Kang et al., 1987) or a growth factor (Rossjohn et al., 1999), and influence cell proliferation, neurite outgrowth, cell adhesion, synaptogenesis and regulation of neural stem-cell differentiation similar to Notch-protein (Dawkins and Small, 2014). APP can be processed via two alternative pathways: *non-amyloidogenic* and *amyloidogenic* pathways (Fig. 5). Products of APP processing via the non-amyloidogenic pathway are not considered to be pathologic, on the contrary, the amyloidogenic pathway produces Aβ peptides of various lengths, from which $A\beta_{40}$ and $A\beta_{42}$ are most important for AD pathogenesis.

Even though A. Alzheimer characterized the Aβ deposits in AD already in 1907, the Aβ peptide was sequenced only in 1984 from the β-sheeted fibrils found in the brain of both AD patients and individuals with Down's syndrome (Glenner and Wong, 1984a, b). One year later, the same peptide was reported to be the core protein of neuritic plaques in AD (Masters et al., 1985). In addition to its neurotoxic properties, the possible physiological role of Aβ is still not understood in detail, but it is produced also during normal cell metabolism at low concentrations (Haass et al., 1992). Aβ is able to cross BBB; it can be cleared from the brain via low density lipoprotein receptor-related protein 1 (LRP-1) (Shibata et al., 2000) and enter the brain via the receptor for advanced glycation end products (RAGE) (Deane et al., 2003). Various enzymes, i.e. neprilysin, insulin degrading enzyme and endothelin-converting enzyme, are involved in the degradation of Aβ under normal circumstances.

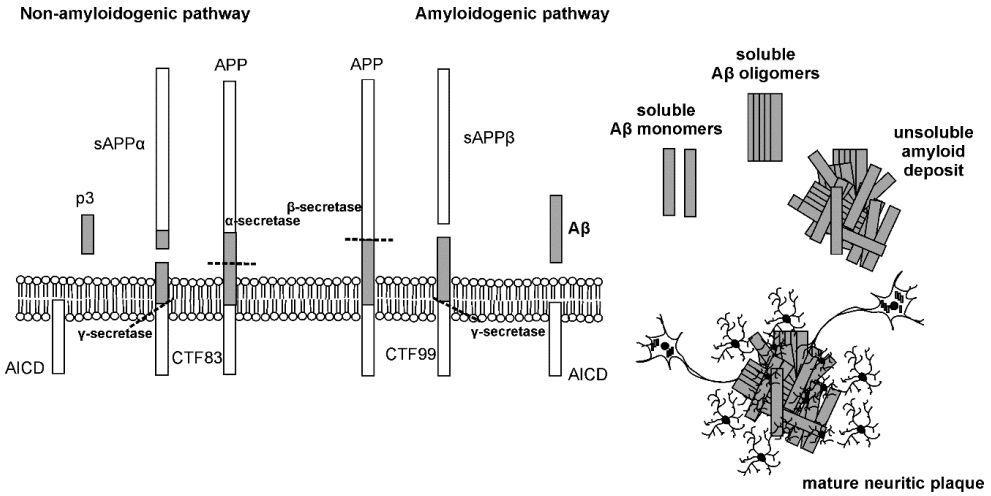

Figure 5. Processing of amyloid precursor protein (APP) via the amyloidogenic and non-amyloidogenic pathway. In the non-amyloidogenic pathway, APP is cleaved within the beta-amyloid (Aβ) sequence by α-secretase and thus Aβ production is halted. In the amyloidogenic pathway, APP is cleaved by β- and γ-secretases to produce Aβ peptides, APP intracellular domain (AICD) and secreted APPβ (sAPPβ). Aβ monomers can further aggregate and form soluble oligomers and subsequently insoluble amyloid deposits. The mature neuritic plaque contains the insoluble amyloid core in addition to reactive microglia, activated astrocytes, and a corona of dystrophic neurites displaying neurofibrillary changes. CTF = carboxyterminal fragment. Modified from Claeysen et al., 2012.

However, when production, clearance and degradation of Aβ are not balanced, Aβ peptides aggregate to form soluble oligomeric structures, insoluble fibrils and eventually plaques (Fig. 5). The molecular structure of $A\beta_{42}$ fibrils, composed of two fibrillary subunits where s-shaped monomers accrue on top of each other, was recently resolved using solid state nuclear magnetic resonance (Colvin et al., 2016; Walti et al., 2016).

2.2.2. *The amyloid cascade hypothesis*

To date, the most widely accepted hypothesis explaining the pathological processes in AD is the amyloid cascade hypothesis, originally presented in 1992 by John Hardy and Gerald Higgins (Hardy and Higgins, 1992). The hypothesis states that an imbalance between clearance and production of Aβ leads to its oligomerization and accumulation in the brain, and is the primary event launching the cascade of AD pathogenesis. With time, the gradual accumulation of Aβ will subsequently trigger other pathological events, such as activation of astrocytes and microglia, altered kinase and phosphatase functions leading to tau aggregation and formation of NFTs, oxidative injury, synaptic deficits, and finally neuronal and synaptic dysfunction, cell loss, and cognitive deficits (Hardy and Higgins, 1992; Selkoe and Hardy, 2016). The hypothesis is supported by the genetic data and discoveries of the EOAD mutations in the APP, PSEN1 and PSEN2 genes, promoting either the overall production of Aβ or aggregation of Aβ, by increasing the $A\beta_{42}/A\beta_{40}$ -ratio. The most convincing discovery supporting the amyloid hypothesis is that mutations in the gene coding for tau protein do not cause the production of Aβ plaques or AD, but rather are associated with frontotemporal dementia with parkinsonism (Poorkaj et al., 1998). In addition, many novel risk genes for LOAD are involved in Aβ clearance and catabolism, and the recently presented genetic data of a

novel protective polymorphism found in the APP gene continue to support the importance of Aβ for the disease process (Hardy and Selkoe, 2002; Jonsson et al., 2012). Recently, Aβ was also seen to induce tau pathology in human neural stem-cells with EOAD mutations in a novel three dimensional (3D) cell culture model (Choi et al., 2014), as well as in a P301L mutant tau transgenic mice (Gotz et al., 2001), further supporting the amyloid cascade hypothesis. In addition, changes in diagnostic biomarkers for Aβ deposition have been seen to precede alterations in other AD-related changes (Selkoe and Hardy 2016).

In addition to supporting data, discrepancies also exist, giving reasons to question the validity of the simplistic version of the amyloid cascade hypothesis. Firstly, the amount of Aβ deposits in the brain has not been seen to be associated with the cognitive deficits (Nelson et al., 2012). In addition, Aβ deposition has been shown to be present also in individuals without any cognitive problems (Jack et al., 2014; Rodrigue et al., 2012). It has also been suggested that it is the soluble oligomeric forms of Aβ, rather than the immunohistochemically defined insoluble plaques, that are responsible for the synaptic dysfunction and neurotoxic effects (Lambert et al., 1998; Walsh et al., 2002). The oligomer-to-plaque ratio has also been seen to separate clinically normal and mildly demented subjects that both had similar Aβ plaque densities, suggesting that aged healthy individuals with abundant deposition could have lower oligomer levels, explaining their failure to suffer a cognitive decline (Esparza et al., 2013). Based on these findings, the updated version of the amyloid hypothesis highlights the contribution of soluble oligomers in the pathological events, either by direct injuring of the synapses and neurites, or by indirect activation of microglia and astrocytes (Hardy and Selkoe, 2002; Selkoe and Hardy, 2016). Neuropathological data revealing neurofibrillary changes in the absence of Aβ deposition even in children and young adults also seems to contradict the original cascade hypothesis (Braak and Braak, 1997; Braak and Del Tredici, 2015), even though high levels of soluble forms of Aβ could be present, and have a role in changing tau metabolism also during these very early phases (Duyckaerts, 2011). Another concern has been raised by the fact that tg mice with EOAD mutations show robust Aβ deposition and various features of AD, but often no neurodegeneration. In tg mice co-expressing human APP and human tau mutations, accelerated tangle formation is present, and even though they do not fully represent the human AD pathology, they do point to a clear link between Aβ and tau pathologies (Lewis et al., 2001). Perhaps the greatest setback for the validity of the amyloid hypothesis has been the disappointing results of all anti-amyloid treatments reaching phase 3 clinical trials (Aisen et al., 2011; Doody et al., 2013; Doody et al., 2014; Salloway et al., 2014).

2.3. Mouse models of Aβ pathology

Animal models of human diseases provide an important tool in the biosciences e.g. for investigating the role of different molecular pathways for specific pathological processes, for target validation in drug development and for evaluating novel therapeutics and PET tracers *in vivo*. Since the introduction of the amyloid cascade hypothesis, there have been many attempts to create animal models that could mirror progressive Aβ pathology and other pathological features of AD. Consequently, multiple models mimicking human neuropathology have been developed since the mid-1990s (for a review, see e.g. Duyckaerts et al., 2008). Mice are most often used as research models as they have a relatively short lifespan and thus good cost-efficiency, they are easy to handle, creating tg mouse models is relatively simple, pathological changes occur in a relatively short time,

and their brain networks and neurobiological processes are comparable to those of humans (Kitazawa et al., 2012). At present, 120 mouse models for AD can be found at the Alzforum Research Model Database (2.1.2017; www.alzforum.org/research-models), however, none of them incorporates all features of the complex AD pathology.

In addition to tg mice, tg rat models expressing pathological features of AD are also available (for a review, see e.g. Do Carmo and Cuello, 2013). The larger body and brain size of rats makes them favorable over mice for many research applications such as repeatable blood sampling and central nervous system (CNS) imaging. In addition, rats are genetically, physiologically and morphologically closer to humans than mice (Kitazawa et al., 2012) and have well characterized and rich behavioral display that makes them suitable for evaluating cognitive alterations related to disease or novel treatment strategies (Do Carmo and Cuello, 2013). Due to space limitations, only mouse models will be discussed in more detail in the following sections.

2.3.1. *APP transgenic models*

Most of the mouse models developed to mimic AD pathology overexpress human APP with associated EOAD mutations. Mice that express only wild type (wt) human APP display only modest neuropathological changes in the absence of Aβ pathology. However, when a transgene of human APP with one or more of the known EOAD mutations is introduced into the mouse genome and over-expressed to non-physiological levels by the use of specific promoters, these mice are capable of capturing multiple aspects of the human disease, such as robust Aβ deposition and plaques, neuroinflammation, tau-alterations, and impairment in learning and memory. Presence of cerebral amyloid angiopathy and synaptic loss or dysfunction have also been reported, however, these are not well established features of the tg mouse models. The temporal course and age of onset of Aβ deposition vary between different tg models and depend on the used EOAD mutations, promoters for transgene expression, as well as on the levels of expressed transgene in the brain (Kitazawa et al., 2012).

To date, the most common EOAD mutations used for generation of tg mice are the Swedish double mutation (APP_{Swe}, K670N/M671L; increases Aβ production), London mutation (APP_{Lon}, V717I; increases $A\beta_{42}$ relative to $A\beta_{40}$), Indiana mutation (APP_{Ind}, V717F; increases $A\beta_{42}$ relative to $A\beta_{40}$), Arctic mutation (APP_{Arc}, E693G; decreases non-amyloidogenic processing of APP and increases aggregation of Aβ) and Dutch mutation (APP_{Dutch}, E693Q; increases production of $A\beta_{40}$ and $A\beta_{40}/A\beta_{42}$ ratio) (Chin, 2011). To accelerate the Aβ pathology further, models expressing a combination of mutations that both increase the general Aβ production (e.g. APP_{swe}) and increase the aggregation properties of Aβ or the proportion of $A\beta_{42}$ over $A\beta_{40}$ (e.g. APP_{Lon} or APP_{Ind}), have also been generated (e.g. TgCRND8 mice). However, the current APP tg models still fail to exhibit NFT formation and robust neuronal loss, suggesting that Aβ deposition alone is not sufficient to drive all the pathological processes in mice (Kitazawa et al., 2012). Genotype and phenotype characteristics of different tg mouse models of AD mentioned later in this chapter are presented in Table 1.

Table 1. Genotype and phenotype characteristics of representative tg mouse models of AD-like pathology. APP = amyloid precursor protein; APP mutations: Swe = Swedish KM670/671NL mutation; Ind = Indiana V717F mutation; Flo = Florida I716Vmutation; Lon = London V717I mutation; EOAD = early onset Alzheimer's disease; hu = human; MAPT= microtubule associated protein tau; mo = month; PSEN = presenilin; w = week. Data collected from Chin, 2011 and from Alzforum web-page (http://www.alzforum.org/research-models).

Name	Transgenes	EOAD mutation	Promoter	Background	Plaques	NFTs	Neuronal loss	Gliosis	Behavioral changes	References
Tg2576	APP	huAPP695$_{Swe}$	Hamster PrP	B6;SJL mixed	11–13 mo	No	No	10–16 mo	< 6 mo, > 12 mo	(Hsiao et al., 1996)
APP23	APP	huAPP751$_{Swe}$	Mouse Thy 1	C57Bl/6N	6 mo	No	Hippocampal	Present	3 mo	(Sturchler-Pierrat et al., 1997)
TgCRND8	APP	huAPP695$_{Swe, Ind}$	Hamster PrP	Hybrid C3H/He-C57BL/6	3 mo	No	Hippocampal	3 mo	3 mo	(Chishti et al., 2001)
APPPS1-21	APP+PSEN1	huAPP$_{Swe}$, PSEN1$_{L116P}$	Mouse Thy 1	C57Bl/6	6 w	No	Unknown	6 w	7–8 mo, 12 mo	(Radde et al., 2006)
APP$_{swe}$-PS1$_{dE9}$	APP+PSEN2	hu/moAPP695$_{Swe}$, PSEN1$_{\Delta E9}$	Mouse prion	(C57BL/6 x C3H)F2	6 mo	No	Hippocampal	3 mo	12 mo	(Huang et al., 2016; Jankowsky et al., 2004; Jankowsky et al., 2001a)
5xFAD	APP+PSEN1	APP695$_{Swe, Flo, Lon}$ PSEN1$_{M146L, L286V}$	Mouse Thy-1	(C57BL/6 x SJL)F1	2 mo	No	Subiculum, layer V	2 mo	4–6 mo	(Oakley et al., 2006)
PS2APP	APP+PSEN2	huAPP$_{Swe}$, PSEN2$_{N141I}$	Thy-1, mouse PrP	C57BL/6	6 mo	No	Unknown	6 mo	8 mo, 12 mo	(Ozmen et al., 2009)
3 x TG	APP+MAPT +PSEN1	APP696$_{Swe}$, MAPT$_{P301L}$ PSEN1$_{M146V}$	Mouse Thy-1.2	129/C57Bl/6	6 mo	12 mo	Unknown	7 mo	4 mo	(Oddo et al., 2003)

Some models express hyperphosphorylated tau in association with neuritic plaques, but paired helical filaments and NFT-like pathology are still absent (Duyckaerts et al., 2008). Introduction of additional mutated forms of the microtubule associated protein tau (MAPT) gene has led to the development of double or triple tg models such as the 3xTg-AD mice expressing the most common tau mutation, P301L, in addition to APP_{swe} and $PSEN1_{M146V}$. For the first time, these mice displayed all of the key pathological lesions present in human AD in a correct temporal and spatial matter: intracellular accumulation of Aβ, followed by its extracellular deposition into plaques and intracellular tau accumulation (Oddo et al., 2003). However, the validity of these double or triple tg animal models in relation to human AD without causative tau mutations should be carefully considered.

The advantages in transgene techniques have allowed also development of multiple tg rat models expressing various characteristic parts of AD pathology (see e.g.Cohen et al., 2013; Echeverria et al., 2004; Folkesson et al., 2007; Leon et al., 2010; Liu et al., 2008). One of the available models is the McGill-R-Thy1-APP rat (Leon et al., 2010). Homozygous McGill-R-Thy1-APP rats display increased intracellular Aβ starting from one week of age and subsequent pre-plaque gliosis, impairments in Morris water maze and finally neuritic plaques at the age of 6−9 months (Hanzel et al., 2014; Leon et al., 2010). Another tg rat model, the TgF344-AD rat, is in turn the first model presenting the full array of AD pathology, including NFT like structures and neuronal loss in relation to Aβ pathology, in the absence of mutated MAPT transgene (Cohen et al., 2013). Consequently, this model could be seen more valid for translational and basic AD research than the triple tg mice with MAPT gene mutations.

2.3.2. *APP and PSEN double transgenic models*

Mutations in the PSEN1 or PSEN2 genes can also cause EOAD; however, when mutated human PSEN1 and PSEN2 were used to create mouse models, they exhibited elevated Aβ levels, but without plaques or other pathological lesions, probably due to the differences in mouse Aβ sequence and its reduced aggregatory properties in comparison to human Aβ (Dyrks et al., 1993). PSEN1 knockout, on the other hand, is lethal at the embryonic stage, but not at the post-natal stage, evidence of an important developmental role of PSEN1 (Duyckaerts et al., 2008). Due to these reasons, PSEN1 and PSEN2 mutations have been mainly used in combination with various APP mutations for the generation of double tg models, such as the APP_{swe}-$PS1_{dE9}$, APPPS1-21 or PS2APP (Jankowsky et al., 2001; Ozmen et al., 2009; Radde et al., 2006). These models generally display robust Aβ pathology and accelerated rates of deposition as the additional PSEN mutation increases the production of the more easily aggregated $Aβ_{42}$ over $Aβ_{40}$. The co-expression also lowers the age of onset for plaque pathology. 5XFAD mice, with 3 different mutations in the APP gene and additional two mutations in PSEN1, represent the earliest onset, with Aβ deposition beginning already at 1.5 months (Oakley et al., 2006).

In addition to the aforementioned tg mice, multiple models expressing LOAD susceptibility genes and a combination of other genes of interest also exist. Due to space limitations, it is impossible to review all models in this thesis, but an exhaustive list of tg models available for AD research can be found in the Alzforum web-page (www.alzforum.org/research-models).

2.3.3. New generation of knock-in mouse models

In addition to the expected and desired increase in Aβ production in the tg models, elevated APP expression to non-physiological levels with artificial promoters leads also to increased activity of the other APP fragments, expression of APP in cell types that normally do not express APP, alterations in endogenous gene expression and interferences within the cellular transport machinery (Nilsson et al., 2014). Due to the multiple and partly unknown physiological roles of APP, it has been speculated that many of the phenotypic characteristics of tg AD mice could actually be artefacts from overproduction of other APP fragments, such as the sAPP, AICD, CTF83 and CTF99 (Nilsson et al., 2014; Saito et al., 2014). These unwanted effects are avoided by using infusion models, i.e. direct intracerebral administration of Aβ peptides into the brain. However, methodological differences hamper the use of these models, and results have been highly varying between laboratories depending on the injection site, duration of infusion and used Aβ peptide (Van Dam and De Deyn, 2011).

Recently, a new generation mouse model, presenting $A\beta_{42}$ overproduction without overexpression of the precursor APP gene, has been developed by adding a humanized Aβ sequence with EOAD mutations to the endogenous mouse APP gene using a knock-in technique (Saito et al., 2014). These animals displayed a progressive increase in $A\beta_{42}$ levels, Aβ deposition, neuroinflammation, synaptic alterations and memory impairment, but similar levels of APP and AICD than wt control mice. However, these mice also failed to produce tau pathology (Saito et al., 2014).

2.4. PET imaging of Aβ in Alzheimer's disease

Recent developments in molecular imaging techniques have allowed researchers and clinicians to visualize and quantify molecules and cellular processes of interest *in vivo* in living subjects, in contrast to traditional *ex vivo* techniques, where only tissue samples could be examined. Molecular imaging methods that allow longitudinal studies of the biological processes of interest are beneficial for many reasons e.g. for temporal characterization of disease processes, improving diagnostics and treatment planning, for target validation and for testing novel interventions in drug development. In the following chapters, the principle of PET, available PET tracers for amyloid imaging, and the role of amyloid PET imaging in both preclinical research and in clinical applications will be discussed.

2.4.1. *The PET principle*

PET is a nuclear imaging method that enables quantitative measurements of biological functions in a living subject. It is based on PET tracers labelled with short-lived positron emitting radionuclides, and PET cameras that can detect the high energy photons emitted during the decay of the radionuclides. The two PET radionuclides that have had most impact on medical imaging are carbon-11 (^{11}C, $t_{1/2}$ = 20.4 min, E = 0.96 MeV) and fluorine-18 (^{18}F, $t_{1/2}$ = 109.8 min, E = 0.63 MeV). These PET radionuclides are produced by irradiation of stable atoms with high energy charged particles produced by a cyclotron. ^{11}C is a radioactive isotope of carbon, and since carbon is naturally present in most biologically active compounds, and it could, in theory, replace its stable isotope in a molecule without affecting its bioactivity (Ferrieri, 2003). In addition, ^{18}F is often used to replace hydroxyl groups in biological compounds, as there are no positron emitting isotopes for hydrogen (Phelps, 2000). Positron emitting radionuclides have an excess of protons (p) and they can decay either through positron emission (β^+ decay) or electron capture. In β^+ decay, the excess proton in the

nucleus is converted into a neutron (n) and a positron (e^+), which are emitted from the nucleus simultaneously with a neutrino (ν) that is not detected.

$$\mathbf{p \rightarrow n + e^+ + \nu}$$

Positrons are antiparticles to electrons (e^-); these particles have an equal mass but opposite electrical charge (Cherry and Dahlblom, 2004). Positrons are emitted with a range of energy, depending on the radionuclide, but they are short-lived, and rapidly lose their energy when traveling in the surrounding electron rich matter. When most of its kinetic energy is lost, a positron is able to collide with its antiparticle, and trigger a process called *annihilation*. In an annihilation, the masses of e^+ and e^- are converted into electromagnetic energy that is released in the form of two high energy (511 keV) annihilation photons travelling in opposite directions (Cherry and Dahlblom, 2004). This process forms the base of PET imaging (Fig. 6): These co-incidence photons have high energy (gamma ray region of the electromagnetic spectrum), they are likely to escape the body and can be detected by the detector ring of a PET camera surrounding the imaging object. Based on the two simultaneous events detected on opposite sides of the detector ring, the spatial location of the annihilation can be located. In a typical PET scan, 10^8–10^{10} such events are registered and corrected for multiple factors, e.g. attenuation, scatter and random coincidences. Finally, the data is reconstructed into a 3D tomographic images, where the signal intensity in each 3D voxel is proportional to the amount of the radionuclide in that voxel (Cherry and Dahlblom, 2004).

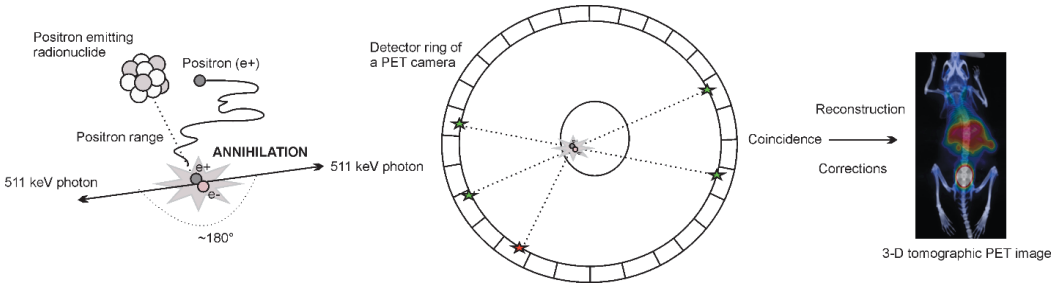

Figure 6. Annihilation and the principles of PET imaging. Positron emitting radionuclides, such as carbon-11, emit a positron (e^+) as they decay. The emitted positron travels a few millimeters in surrounding matter losing most of its kinetic energy before colliding with its antiparticle (e^-). This process, called annihilation, produces two 511 keV photons which move in nearly opposite directions. These annihilation photons can subsequently be detected with detectors in a PET camera and, based on the co-incidence of the registered events, a line of response can be defined. After multiple corrections and applying the appropriate reconstruction algorithm, a 3D tomographic image representing the radioactivity distribution is obtained.

PET is a very sensitive tracer technique, typical PET tracer tissue concentrations are pico- or femtomoles per gram. This high sensitivity not only results in improved image quality, but also the possibility to perform shorter scans, with improved temporal resolution by enabling shorter time frames with statistically relevant data (Rahmim and Zaidi, 2008). The spatial resolution is 4−6 mm for a typical clinical PET scanner, ~2.5 mm for dedicated human brain scanner (HRRT) and ~1.5 mm for µPET devices designed for small animal imaging. Spatial resolution of PET is clearly dependent on detector-related effects, but in addition, it is limited by two physical issues: the positron range and photon non-collinearity. These are the errors introduced by the different location of the decay of the radionuclide and the origin of the annihilation photons, and by the small deviation from the theoretical 180º angle between the two annihilation photons, respectively (Cherry and Dahlblom, 2004).

Single photon emission computed tomography (SPECT) is another nuclear imaging technique widely used for medical applications. SPECT radionuclides are heavy isotopes of non-natural elements, such as technetium-99m (^{99m}Tc, $t_{1/2}$ = 6.01 h, E = 140.5 keV), that decay through single photon emission and emit lower energy photons than the annihilation photons. The production of physiologically relevant tracers becomes more challenging with SPECT than with PET radionuclides, however, the longer half-life of SPECT radionuclides is beneficial for investigating slower biological processes or biological molecules with more delayed distribution and clearance, such as antibodies. The longer half-life of SPECT radionuclides makes SPECT tracers also more readily available. In addition, the labelling chemistry of SPECT tracers is usually less complicated and less expensive than that of PET tracers (Ziegler, 2011), making the method less expensive than PET imaging. In comparison to PET, SPECT has lower sensitivity. The detection of a single emitted photon does not contain any information about the origin of the event without physical collimators that absorb all photons that are not incident on the detector from one particular direction, which again reduces the detected events by 1−2 orders of magnitude in comparison to positron emitters (Cherry and Dahlblom, 2004). The typical spatial resolution for a clinical SPECT scan is similar to PET, however, even submillimeter resolution has been obtained with μSPECT systems designed for small animal imaging (Beekman et al., 2005; van der Have et al., 2009).

2.4.2. *PET tracers for Aβ imaging*

PET tracers are biologically active molecules that bind to specific targets of interest, and are labelled with some of the above-mentioned PET radionuclides. They are referred to as “tracers” as they are injected into living subjects in non-pharmacological (trace) doses, that lead to less than 10% target occupancy which nonetheless can be measured in a living subject without affecting the targets function (Gambhir, 2004). These molecules can be designed to measure and quantify either physiological processes, such as glucose metabolism, different receptor systems or pathophysiological changes occurring in diseased states. For example, in subjects with AD, PET tracers are used to recognize increases in pathologically relevant molecules, such as the Aβ deposits and tau protein, created during the disease process.

To be clinically useful, a novel PET tracer must have certain beneficial characteristics: firstly, the addition of a suitable radionuclide to the molecule needs to be possible, and the resulting tracer has to be synthesized with sufficient yield, specific activity (SA), radiochemical and chemical purity to allow its injection into a living subject *in vivo*. SA is one of the most important properties for a tracer. It describes the isotopic purity of the tracer as an amount of radioactivity in a mass unit (Bq/mol); in other words the number of molecules radiolabeled with the positron-emitter and capable of producing a radioactive signal at a certain time, in relation to the total number of molecules (Gambhir, 2004). A high SA is needed especially in CNS imaging, as very low injected mass amounts of molecules binding to CNS targets are required so that they will not interfere with the system of interest in living human subjects. Secondly, a PET tracer has to be able to reach its target tissue, which in the case of CNS targets means passing through the BBB. Small and lipophilic molecules tend to cross the BBB easier; however, the tracer can still be actively pumped out of the brain by efflux pumps, such as the P-glycoprotein, located in the endothelial cell membrane. Thirdly, the tracer needs to bind to its target molecule with sufficient affinity. The affinity between a certain ligand and its target protein is described by the equilibrium dissociation constant (K_d), describing in molar units the concentration of the ligand that results in half the binding sites to be occupied (i.e. 50% occupancy). Traditional

idea has been, that for successful radiotracers, the K_d-value should be ≤ 1 nM (Mathis et al., 2003). However, the required affinity is related to the total concentration of the target protein, which in the case of Aβ in AD brain is considered to be high (1−10 μM) compared to values of 1−200 nM for most neuroreceptors (Furumoto et al., 2007; Mathis et al., 2003). In addition, the non-specific binding of the ligand to molecules other than its target protein should be low, so that sufficient target-to-background signal and sensitivity can be reached. Brain uptake and non-specific binding profile are related to the lipophilicity of the tracer; moderate lipophilicity often leads to highest brain uptake, whereas highly lipophilic compounds undergo higher non-specific binding to brain tissue, plasma proteins, and metabolic enzymes. Too low lipophilicity might in turn hinder passage through the BBB (Waterhouse, 2003).

Multiple molecules from different molecular classes have been developed for Aβ imaging during the past years. Many of the developed molecules are derivatives of the common histological dyes used for amyloid staining, such as **Congo red** and **Thioflavine T**. These fluorescent dyes bind to the β-sheeted amyloid structures and are used for staining amyloid in histological sections. However, they are not useful *in vivo*, due to their positive charge, hydrophilicity and thus limited passage through the BBB. Due to space limitations, only the small fraction of developed Aβ targeting PET tracers which have reached clinical evaluation will be further described in the following chapters and presented in Table 2.

^{11}C-labeled PET tracers for Aβ imaging

Thioflavine T has been extensively used as a pharmacophore for developing uncharged derivatives suitable for PET tracers. In the University of Pittsburgh, many of these kinds of molecules, referred to as 2-arylbenzothiazoles (**BTAs**), have been synthesized and evaluated in the laboratories of William Klunk and Chester Mathis (Klunk et al., 2001; Mathis et al., 2002; Mathis et al., 2003). Finally, 6-OH-BTA-1 (Pittsburgh compound B, **[^{11}C]PIB**), was selected for further development due to its relatively low non-specific binding and fast clearance from mouse and baboon brain (Mathis et al., 2003). *In vitro* binding of [^{3}H]PIB to AD brain homogenates demonstrated that the compound possessed low nanomolar binding affinity (Klunk et al., 2005), and later both high and low affinity binding sites have been detected in human AD brain (Ni et al., 2013). In addition, the high affinity PIB binding site has recently been proposed to contain not only insoluble Aβ, but also lipid and protein components, e.g. ApoE and tau, that are required for binding (Matveev et al., 2014).

Using four-dimensional multiphoton microscopy, PIB was seen to enter the brain of living mice rapidly, label Aβ deposits within minutes and the non-specific binding was cleared quickly (Bacskai et al., 2003). The first clinical study using [^{11}C]PIB was published in 2004 and it demonstrated increased retention of [^{11}C]PIB in AD patients in comparison to healthy controls, especially in the cortical brain areas known to contain Aβ deposits (Klunk et al., 2004). Subsequently, binding of [^{11}C]PIB to Aβ aggregates has been validated by comparing imaging results to

Table 2. Summary of Aβ targeting PET tracers that have entered clinical evaluations. *Brain uptake was measured in wild type mouse brain. AD = Alzheimer's disease; N/A= not available; K_d = dissociation constant; K_i = inhibitory constant; LogP = partition coefficient; LogD = distribution coefficient.

Radiotracer	Uptake ratio*		K_d	K_i	Competitor	LogP	Log D	References
	2:30 min	2:60 min						
[^{11}C]PIB	9[2]	11.7[1]	4.7 nM ($A\beta_{40}$ fibrils)[1], 1.4 nM (AD brain homogenate)[1]	2.8 nM ($A\beta_{40}$ fibrils)[3]	[^{125}I]IMPY[3]	1.2[1]	2.5[2]	[1]Mathis et al., 2003; [2]Johnson et al., 2009; [3]Zhang et al., 2005
[^{11}C]AZD2184	17	N/A	8.4 nM ($A\beta_{40}$ fibrils)	24.6 nM (AD brain sections)	PIB	N/A	1.8	Johnson et al., 2009
[^{11}C]SB13	N/A	5[1]	2.4 nM (AD brain homogenate)[2]	6.0 nM ($A\beta_{40}$ fibrils)[1]	[^{125}I]TZDM	2.4[1]	N/A	[1]Ono et al., 2003; [2]Kung et al., 2004
[^{18}]FDDNP	N/A	N/A	0.12 nM and 1.86 nM ($A\beta_{40}$ fibrils)[1]	293 nM (AD brain homogenate)[2]	[^{3}H]SB13	3.9[1]	N/A	[1]Agdeppa et al., 2001; [2]Kung et al., 2003
[^{18}F]flutemetamol	3.6[1]	N/A	1.6 nM ($A\beta_{40}$ fibrils)[1]	1.9 nM (AD brain homogenates)[3]	[^{3}H]PIB	1.7[2]	3.2[1]	[1]Júreus et al., 2010; [2]Mathis et al., 2007; [3]Mathis et al., 2008
[^{18}F]florbetaben	N/A	3.1	N/A	6.7 nM (AD brain homogenate)	[^{125}I]IMPY	2.4	N/A	Zhang et al., 2005
[^{18}F]florbetapir	N/A	3.4	3.7 nM (AD brain homogenate)	2.9 nM (AD brain homogenate)	AV-45	N/A	N/A	Choi et al., 2009
[^{18}F]NAV4684	10	N/A	2.3 nM ($A\beta_{40}$ fibrils)	23.1 nM (AD brain sections)	[^{3}H]AZD2184	N/A	2.8	Júreus et al., 2010

immunohistochemical staining of Aβ neuropathology in brain biopsy specimens (Leinonen et al., 2008; Leinonen et al., 2013). To date, [^{11}C]PIB PET has been widely used for clinical research purposes in numerous research centers around the world and it is considered as the gold standard of amyloid PET imaging. However, its short half-life hampers its usability in clinical practice.

Attempts to develop a PET tracer with higher sensitivity resulted in another Thioflavine T derivative and PIB analogue **[^{11}C]AZD2184** (Johnson et al., 2009). An initial *in vitro* evaluation of [^{3}H]AZD2184 revealed its high affinity to Aβ fibrils and lower non-specific background binding on cortical brain sections in comparison to [^{3}H]PIB (Johnson et al., 2009). In AD patients, uptake of [^{11}C]AZD2184 was substantially higher in brain areas expected to contain Aβ deposits, in comparison with control subjects. In addition, ^{11}C-radioactivity was low in the cerebellum (CB) and homogeneous in young control subjects, verifying the preclinical finding of low background signal (Nyberg et al., 2009).

Stilbene is a simple molecule that has been used as a pharmacophore in the development of molecules binding to Aβ by Kung and co-workers (Ono et al., 2003). From the stilbene derivatives that were synthesized, **[^{11}C]SB13** was reported to have beneficial properties such as moderate lipophilicity similar to [^{11}C]PIB, good entry and clearance from rat brain, and distinctive binding to Aβ deposits in tg mouse brain sections *in vitro* (Ono et al., 2003). In humans, [^{11}C]SB-13 was seen to possess similar binding properties as [^{11}C]PIB, (Verhoeff et al., 2004), however, due to the practical difficulties with the ^{11}C-labelled agent, no further clinical studies were performed, and the development of second generation of ^{18}F-labelled stilbene derivatives was initiated.

^{18}F-labeled PET tracers for Aβ imaging

Multiple ^{18}F-labelled Aβ tracers have been developed to overcome the practical limitations of [^{11}C]PIB. The longer half-life of ^{18}F enables more flexible commercial production and wider use also in imaging centers without an on-site cyclotron and radiochemistry department. To date, three ^{18}F-labeled tracers, [^{18}F]flutemetamol, [^{18}F]florbetaben and [^{18}F]florbetapir have been approved by the Food and Drug Administration (FDA) and European Medicines Agency (EMA) for clinical use. However, they all have higher non-specific binding to cerebral white matter than [^{11}C]PIB, thus tracers with lower non-specific background binding and higher sensitivity are still being developed.

The first ^{18}F-labeled ligand that reached clinical evaluation in AD patients was an aminonaphthalene derivative, referred to as [^{18}F]FDDNP. In contrast to [^{11}C]PIB, [^{18}F]FDDNP binds also to diffuse Aβ deposits and NFTs in AD brain, and has two kinetically distinguishable binding sites on Aβ aggregates to which it binds with nanomolar affinity (Agdeppa et al., 2001). [^{18}F]FDDNP was shown to cross the BBB and label Aβ aggregates in the brain of both AD patients and a triple tg rat model (Shoghi-Jadid et al., 2002; Teng et al., 2011). In humans, [^{18}F]FDDNP exhibited higher uptake in the brain of AD subjects than healthy controls, and was able to differentiate AD from MCI and subjects without cognitive deficits. However, its sensitivity was relatively low, resulting in only small differences between groups (Shoghi-Jadid et al., 2002; Small et al., 2006). Interestingly, binding of [^{18}F]FDDNP to Aβ_{40} fibrils and AD brain sections can be inhibited by the commonly used non-steroidal anti-inflammatory drugs, such as naproxen and ibuprofen (Agdeppa et al., 2003).

[^{18}F]flutemetamol (previously also referred to as 3´-F-6-OH-BTA1, 3´-[^{18}F]PIB, [^{18}F]GE-067) is a ^{18}F-labelled structural PIB analogue where ^{18}F-fluorine is attached to the 3´position. *In vitro* evaluation of [^{3}H]flutemetamol detected a low nanomolar binding affinity to Aβ fibrils and specific

binding similar to [^{3}H]PIB to Aβ deposits in brain sections of subjects with AD. However, due to the higher non-specific binding to subcortical white matter, its sensitivity was lower than [^{3}H]PIB (Juréus et al., 2010). [^{18}F]flutemetamol has a biodistribution similar to [^{11}C]PIB, a mean effective dose comparable to other ^{18}F-labelled tracers, and differences in its uptake pattern can discriminate AD patients from healthy controls (Nelissen et al., 2009). [^{18}F]flutemetamol binding in AD brain is similar to [^{11}C]PIB, however, it has higher binding to cerebellar white matter (Vandenberghe et al., 2010). The specificity of [^{18}F]flutemetamol for Aβ imaging has been supported by multiple studies depicting a strong correlation between *in vivo* [^{18}F]flutemetamol binding ratios and immunohistochemically verified Aβ deposition in cortical biopsies (Leinonen et al., 2013; Rinne et al., 2013; Wolk et al., 2011; Wong et al., 2013). Pooled analysis of the results reported an overall sensitivity of 93% and specificity of 100% by majority read (Rinne et al., 2012). [^{18}F]flutemetamol was developed and manufactured by GE Healthcare, and has been approved by the FDA and EMA for clinical amyloid PET imaging of subjects with cognitive impairment; its trade name is Vizamyl™.

[^{18}F]Florbetaben (previously also referred to as [^{18}F]AV-1 and [^{18}F]BAY94-9172) is an ^{18}F-labelled SB-13 derivative where ^{18}F is linked to stilbene via a polyethylglycol chain (Zhang et al., 2005). [^{18}F]Florbetaben shares structural similarities with [^{11}C]PIB, and they bind competitively to the same binding site in Aβ fibrils with similar affinities (Rowe et al., 2008; Zhang et al., 2005). In AD brain homogenates, [^{18}F]florbetaben exhibited high affinity for Aβ, and labeled Aβ plaques in the brain sections of both AD patients and Tg2576 tg mice (Zhang et al., 2005). In clinical studies, [^{18}F]florbetaben binding was seen to correlate with post-mortem neuropathological findings in AD patients, and it displayed 100% sensitivity and 90% specificity for AD by visual interpretation (Rowe et al., 2008). To date, [^{18}F]florbetaben is manufactured by Piramal Pharma Inc. under the trade name Neuraseq™, and is approved by the FDA and EMA for clinical amyloid PET.

[^{18}F]Florbetapir (previously also referred to as ^{18}F-AV-45) is another fluoropegylated stilbene derivative that has been under commercial development. It binds to a single binding site with a low nanomolar binding affinity, and was shown to label Aβ aggregates in brain sections of AD patients and in tg APPswe-PSEN1 mouse brain sections (Choi et al., 2009). *In vivo*, [^{18}F]florbetapir was seen to accumulate in cortical regions of AD patients, whereas binding in healthy controls was minimal (Wong et al., 2010). In addition, cortical retention ratios of [^{18}F]florbetapir and [^{11}C]PIB were highly associated when assessed in the same individuals (Landau et al., 2013). [^{18}F]florbetapir is manufactured by Eli Lily under the trade name Amyvid™, and it was approved by FDA in 2012 and by the EMA in 2013 for clinical amyloid PET in subjects with cognitive impairment.

[^{18}F]NAV4694 (previously also referred to as [^{18}F]AZD4694) was developed to overcome the practical inconveniences of the [^{11}C]AZD2184. [^{18}F]NAV4694 binds to Aβ fibrils with high affinity *in vitro*. It showed a good kinetic profile as a PET tracer in rats, and was seen to bind selectively to Aβ deposits in the cortical grey matter in brain sections from human AD subjects and Tg2576 tg mice. (Juréus et al., 2010). It was able to make a clear separation of AD patients and healthy controls (Cselényi et al., 2012), and display a cortical distribution that was nearly identical to [^{11}C]PIB when evaluated in the same subjects (Rowe et al., 2013). In comparison to other second generation ^{18}F-labelled amyloid PET tracers, [^{18}F]NAV4694 shows a lower level of non-specific binding in white matter, and thus improved sensitivity. [^{18}F]NAV4694 is being further developed by Navidea Biopharmaceuticals, and it is currently in a phase 3 validation trial (ClinicalTrials.gov identifier: NCT01886820).

2.4.3. *Clinical PET imaging of Aβ*

The above-mentioned amyloid tracers have been highly beneficial for research purposes; however, their clinical usability is still limited. To date, the main clinical advantage of amyloid PET is to improve the diagnosis in unclear cases. Wider use for other purposes, such as for diagnostic use in pre-symptomatic phases, is still limited due to cost, lack of disease-modifying treatments and additional ethical and practical issues: Even though negative amyloid PET scan diminishes the likelihood of AD, other dementias cannot be excluded. In addition, even if a positive PET scan is a fairly well validated biomarker for ongoing β-amyloidosis in the brain, the results have to be interpreted in the clinical context. Due to these issues, consensus guidelines for health care practitioners have been published to assist in the appropriate use of amyloid PET in clinical practice (Johnson et al., 2013; Minoshima et al., 2016). In these reports, amyloid imaging was stated to be appropriate for subjects who have objectively confirmed cognitive impairment or a possible AD diagnosis that remains uncertain after a full clinical evaluation by a dementia expert. In addition, knowledge about the presence or absence of Aβ deposition in the brain would need to affect the certainty of diagnosis, and the management of the patient. Appropriate or inappropriate uses of clinical amyloid PET for persons fulfilling these criteria are listed in Table 3.

Table 3. Guidelines for appropriate and inappropriate use of clinical amyloid PET by the Amyloid Imaging Taskforce in 2013. Modified from Johnson et al., 2013 and Minoshima et al., 2016.

Clinical amyloid PET
Appropriate
i) For patients with persistent or progressive unexplained MCI
ii) For patients who meet the core clinical criteria of possible AD, but present atypical clinical course or mixed presentation
iii) For patients with a progressing type of dementia and early age of onset (< 65 years).
Inappropriate
i) For patients meeting core clinical criteria of possible AD with typical age of onset
ii) For evaluation of the severity of dementia
iii) Evaluation of an asymptomatic patient based on family history of AD or ApoE4-genotype
iv) Instead of genotyping for suspected carriers of autosomal dominant mutations
v) For asymptomatic individuals
vi) For any other than medical purposes (e.g. legal, insurance etc.)

In clinical drug trials, PET imaging and Aβ targeting PET tracers can be used in various ways: Firstly, many of the anti-amyloid trials in mild-to-moderate AD subjects have included screening for amyloid biomarkers, such as positive [^{11}C]PIB or [^{18}F]flutemetamol PET to ensure that the trial participants do have Aβ (i.e. the drug target) present in the brain. Secondly, as the consensus has shifted towards prevention and it is believed that early initiation for anti-amyloid therapies will be more effective, amyloid PET provides one way to include only higher risk subjects, such as clinically normal older individuals with positive amyloid PET finding, to the clinical trials (Sperling et al., 2014). In addition, repeated amyloid PET imaging has been widely used in drug trials as a secondary outcome measure, providing information on the temporal course of amyloid deposition at the time of the intervention (Ostrowitzki et al., 2012; Rinne et al., 2010; Sevigny et al., 2016). Amyloid PET imaging is being incorporated into the study design in most of the ongoing clinical trials; however, a similar design

has rarely been exploited in the preclinical phase of the drug discovery process while testing the compounds in tg animal models.

2.4.4. *Preclinical PET imaging of Aβ*

The usability of Aβ targeting PET tracers for *in vivo* imaging of tg mice has been debated during the last years. Similar to clinical drug trials, repeated imaging of tg mice with tracers such as [^{11}C]PIB or [^{18}F]flutemetamol would add translational value for preclinical studies evaluating the therapeutic effect of disease modifying drugs in animal models of AD. However, even though [^{11}C]PIB has shown clear specific binding to Aβ aggregates in tg mouse brain *in vitro*, *in vivo* imaging studies with tg mice have provided more controversial results. Initial *in vivo* imaging studies using [^{11}C]PIB in tg mouse models were disappointing: in PS1/APP mice, there was no significant increase in the whole brain [^{11}C]PIB uptake in comparison to control mice, even though robust Aβ deposition has been claimed to begin at 3 months in this model (Klunk et al., 2005). Similar results were independently obtained using the Tg2576 mouse model: only small differences in cortical uptake ratios were seen in elderly tg and wt mice, leading to the authors concluding that [^{11}C]PIB demonstrated minimal specific binding to Aβ in this model (Toyama et al., 2005). *In vitro* experiments revealed differences in the numbers of high affinity binding sites in tg PS1/APP and AD brain tissue, and in addition to lower affinity of [^{11}C]PIB to Aβ in mouse brain, this was suggested to explain the observed differences in *in vivo* imaging results between mice and men (Klunk et al., 2005; Toyama et al., 2005). Later, Maeda and co-workers successfully demonstrated increased [^{11}C]PIB retention relative to aging in the tg APP23 mouse brain. In this experiment, [^{11}C]PIB had been synthesized with high SA (290 GBq/μmol, end of synthesis), and it was postulated that high SA tracers would be needed for successful *in vivo* imaging of cerebral amyloidosis in tg mice (Maeda et al., 2007). In addition, [^{11}C]PIB binding was seen to associate closely with N-terminally truncated forms of Aβ, suggesting that also differences in the distinctive Aβ subtypes between species might result in differing binding characteristics (Maeda et al., 2007). Due to these controversies, to date, μPET studies have been most commonly used for the development and evaluation of novel PET tracers, or monitoring pathological changes in different tg models and only a few preclinical anti-amyloid intervention studies exploiting the methodology have been published (Balducci et al., 2014; Brendel et al., 2015c). In addition to PET, also other molecular *in vivo* imaging methods, e.g. preclinical MRI (Maier et al., 2015), μSPECT (Chen et al., 2015) and multiphoton microscopy (Hefendehl et al., 2011), are available for studying Aβ deposition in tg mouse models. All of these methods have their advantages and disadvantages, including differences in sensitivity, temporal and spatial resolution, and due to these reasons, different molecular imaging methods can also be combined to supplement each other.

2.5. Aβ centric drug discovery

Multiple therapeutic strategies and targets have been investigated for AD as a result of the complex and multifactorial pathophysiology of the disease (Anand et al., 2014). Examples of these strategies are presented in Figure 7. It is impossible to review this active field in detail within this thesis, thus in the following chapters, only current drugs and Aβ-based strategies that have reached clinical phases are briefly presented. At present, 389 open interventional studies can be found from clinicaltrials.gov website using the search for Alzheimer's disease (2.1.2017), including nine open Aβ-related studies that are in phase 3 (http://www.alzforum.org/therapeutics/search, 2.1.2017).

Aβ	**Tau**	**Others**
Aβ immunotherapy	Tau immunotherapy	Caspase inhibitors
Secretase enzyme modulation	Tau phosphorylation inhibition	Nitric oxide synthase modulation
Affecting Aβ transport	Microtubule stabilization	Nucleic acid drugs
Decreasing Aβ aggregation	Blocking tau oligomerization	Multi-target directed ligands
Increasing Aβ clearance	Enhancing tau degradation	Gonadotropin supplementation
		Lipid modifiers - statins
Neurotransmission	**Intracellular signaling cascades**	Growth factor supplementation
Cholinesterase inhibitors		Metal chelation
NMDA receptor antagonism	**Cellular Ca^{2+} homeostasis**	Epigenetic modifiers
GABAergic modulation		
Serotonin receptor modulation	**Mitochondria**	**Oxidative stress**
Histaminergic modulation		Exogenous antioxidants
Adenosine receptor modulation	**Anti-inflammatory therapy**	Augmenting endogenous defense

Figure 7. Therapeutic targets and strategies for disease modifying drugs in Alzheimer's disease. Aβ based strategies that are presented more in detail in this thesis are highlighted. Modified from Anand et al., 2014.

2.5.1. *Current treatment strategies*

To date, two classes of drugs have been licensed by the FDA and EMA for the treatment of AD; the acetylcholinesterase inhibitors (AChEI) for mild to moderate AD, and the N-methyl-D-aspartate (NMDA) receptor antagonist, memantine, for moderate to severe AD. The AChEI treatment of AD is based on the cholinergic hypothesis, which proposed that disruption in the central cholinergic neurotransmission is an important contributing effect in AD (Bartus et al., 1982). Glutamate, in turn, is the major excitatory neurotransmitter in the brain, and in AD, increased glutaminergic activity can lead to neurotoxicity. To date, three different AChEIs, donepezil, rivastigmine and galantamine are available for the treatment of mild to moderate AD by inhibiting the ACh degrading enzyme, and thus increasing cholinergic neurotransmission. The efficacy of AChEIs has been studied in multiple randomized double-blinded clinical trials, which have shown a mild positive effect on cognitive, functional and behavioral symptoms (Birks, 2006). Memantine, on the contrary is a non-competitive NMDA-receptor antagonist that has been shown to exert a positive effect on cognitive and behavioral symptoms in the moderate to severe phase of AD (Wilcock, 2003). All the aforementioned drugs are well tolerated, but their efficacy varies between individuals and is only temporary and symptomatic in character.

2.5.2. *Disease modifying treatment strategies targeting Aβ*

During the last 25 years, the amyloid cascade hypothesis has exerted a huge influence on guiding AD drug development towards compounds that could either prevent Aβ deposition in the brain, or remove already existing Aβ. Several anti-amyloid strategies have involved: i) increasing the clearance of Aβ by active or passive immunization, ii) decreasing Aβ production via the different secretases iii) affecting Aβ transport, or iv) preventing aggregation or oligomerization of Aβ monomers. In practice, the validation of Aβ as a drug target has proved difficult. Each different Aβ species (monomers, oligomers, protofibrils and mature plaques) has its own distinctive properties, and probably also varying degrees and mechanisms of toxicity, and thus they actually form a group of various targets (Schneider et al., 2014). Different anti-amyloid strategies and examples of compounds in clinical development are presented in Table 4.

Initial studies aiming to enhance Aβ clearance by **immunotherapy** were performed using an active vaccine *AN1792* with full length $A\beta_{42}$. However, the clinical phase 2 trial was terminated due to meningoencephalitis appearing in a subset of patients (Orgogozo et al., 2003). Subsequently, most research has been concentrated around passive immunization, where monoclonal antibodies targeted against different forms of Aβ are directly administered to patients. Many such antibodies have been developed, binding to either soluble monomeric (e.g. *Solanezumab*), fibrillar and oligomeric (e.g. *Gantenerumab, Aducanumab, BAN2401*) or all forms of Aβ (e.g. *Bapinezumab*, *Crenezumab*), and promoting its/their clearance either by binding monomeric forms, or activating microglia mediated clearance mechanisms. As the recent phase 3 immunization trials with Solanezumab and Babinezumab failed to meet the set primary endpoints in improving cognitive functions (Doody et al., 2014; Eli Lilly and Company, 2016; Salloway et al., 2014), it has become clear that promising preclinical data are not easily reproducible in the clinical setting. To date, phase 3 trials with Crenezumab in patients with MCI and prodromal AD (NCT02670083) and Gantenerumab in mild AD (NCT02051608) are still ongoing. In addition, promising interim results have been published from a phase 1b study assessing Aducanumab, where a dose-dependent slowing of clinical decline and reductions in predefined regional [^{18}F]florbetapir uptake were detected at one year (Sevigny et al., 2016). Two phase 3 trials have been initiated with Aducanumab in patients with MCI or mild AD in 2015, but the results are not to be expected before 2022 (NCT02477800, NCT02484547).

Another approach for decreasing Aβ levels in the brain has been to alter Aβ production by **modulating the activity of the secretase enzymes** responsible for APP cleavage. Different compounds have been developed for inhibition of both γ-secretase (e.g. *Semagacestat***)** and β-secretase (e.g. *Verubecestat*), or activation of the non-amyloidogenic α-secretase (e.g. *Epigallocatechin-gallate*). However, modulation of secretase function has proven to be problematic, as both β- and γ-secretases have multiple physiological functions, and also other substrates in addition to APP, such as the Notch receptor for γ-secretase. To overcome this limitation, also γ-secretase modulators, with a Notch sparing function have been developed (e.g. *EVP-0962*). To date, three β-secretase inhibitors, *Verubecestat* (NCT01953601), *E2609* (NCT02956486) and *AZD3293* (NCT02783573), are currently recruiting or undergoing phase 3 trials.

The **transport of Aβ** via the BBB is regulated by the apolipoproteins in a receptor mediated manner, utilizing the low-density lipoprotein receptor related protein (LRP). In addition, RAGE binds to Aβ in the blood with high affinity, and transports it to the brain. One strategy of decreasing brain Aβ has been to increase its transport from brain to periphery, or inhibit the RAGE mediated influx to the brain. *Azeliragon* (known previously as TTP488**)** is a small molecule RAGE-inhibitor, designed to suppress Aβ transport to the brain. The compound entered phase 3 trials with mild probable AD patients in 2015 (NCT02080364).

Recent research has suggested that the aggregation to Aβ monomers into more toxic oligomers would be the cause of neuronal and synaptic failure, and this reasoning has led to the development of molecules that bind to the monomeric peptide and **suppress its aggregation** into more toxic forms. From this category of drugs, *ALZT-OP1* represents a combination therapy with two drugs already approved by the FDA: an asthma medication Cromolyn, shown to inhibit Aβ aggregation *in vitro* and decrease soluble Aβ levels *in vivo* (Hori et al., 2015), and an anti-inflammatory drug, ibuprofen. Phase 3 trials with this combination were initiated in 2015 (NCT02547818).

Table 4. Aβ-based strategies in Alzheimer's disease drug development. *Status is obtained from https://clinicaltrials.gov (21.10.2016).

Anti-Aβ strategy	Compound class	Example drugs in clinical development	Sponsor	Mechanism of action	Status*
Aβ production ↓	α-secretase activator	Epigallocatechin-gallate	Charite University, Berlin, Germany	Enhancement of non-amyloidogenic APP metabolism (among others)	Phase 2/3 completed (NCT00951834), Outcome not published
Aβ production ↓	γ-secretase inhibitor	Semagacestat	Eli Lilly	Inhibition of amyloidogenic APP metabolism	Phase 3 terminated (NCT01035138), No effect on disease progression
Aβ production ↓	γ-secretase modulator	EVP-0962	FORUM Pharmaceuticals/Parexel	Inhibition of amyloidogenic APP metabolism, Notch sparing effect	Phase 2 completed (NCT01661673), Outcome not published
Aβ production ↓	β-secretase inhibitor	Verubecestat	Merck Sharp & Dohme	Inhibition of amyloidogenic APP metabolism	Phase 3 ongoing (NCT01953601), Estimated completion 2021
Modulation of Aβ transport	Small molecule RAGE inhibitor	Azeliragon	vTv Therapeutics, Pfizer, TransTech Pharma Inc.	Blockage of Aβ transport to the brain	Phase 3 ongoing (NCT02080364), Estimated completion 2019
Aβ aggregation↓	Combination therapy, anti-inflammatory compounds	ALZT-OP1 (Cromolyn+Ibuprofen)	Bellus Health Inc.	Prevention of oligomerization and aggregation of monomeric Aβ	Phase 3 ongoing (NCT02547818), Estimated completion 2018
Aβ degradation ↑	Protease (e.g. plasmin, neprilysin) activators	NA	NA	Activation of the proteases responsible for degradation of Aβ	NA
Aβ clearance ↑	Active immunotherapy (vaccination)	AN1792	Janssen Alzheimer immunotherapy	First active vaccine using a full length aggregated $A\beta_{42}$	Phase 2 terminated (NCT00021723), Meningoencephalitis
Aβ clearance ↑	Passive immunotherapy (monoclonal antibodies)	Bapineuzumab	Pfizer/Janssen Alzheimer immunotherapy	Microglia mediated clearance of Aβ	Phase 3 completed and terminated, (NCT00575055, NCT00676143), No clinical benefit
Aβ clearance ↑		Solanezumab	Eli Lilly	Sequestration of soluble monomeric Aβ	Phase 3 terminated (NCT01900665), No clinical benefit; ongoing (NCT02008357), Estimated completion 2020
Aβ clearance ↑		Gantenerumab	Hoffman-La Roche/Genentech	Microglia mediated clearance of Aβ	Phase 3 ongoing (NCT02051608), Estimated completion 2019
Aβ clearance ↑		Crenezumab	Hoffman-La Roche/Genentech	Microglia mediated clearance of Aβ	Phase 2/3 ongoing (NCT02670083), Estimated completion 2021
Aβ clearance ↑		Aducanumab	Biogen/Neurimmune	Microglia mediated clearance of Aβ	Phase 3 ongoing (NCT02477800, NCT02484547), Estimated completion 2022
Aβ clearance ↑		BAN2401	Eisai/Biogen	Microglia mediated clearance of Aβ	Phase 2 ongoing, NCT01767311, Estimated completion 2018

In theory, reductions in brain Aβ levels could also be achieved by **activating the proteases that bind and degrade Aβ**, such as plasmin, neprilysin, insulin degrading enzyme or metalloproteinase 9. This approach is however not specific to Aβ or AD, and even though protease inhibitors are already widely available, the therapeutic effects of protease activators still need further investigation (Anand et al., 2014). To date, no such activators have reached clinical evaluations.

After the disappointing results from the recent phase 3 clinical trials using anti-amyloid strategies, **secondary preventive trials** have recently been initiated. These trials aim to test the effect of anti-amyloid compounds in a more relevant population of older individuals but without clinical symptoms, only an increased risk defined either by positive Aβ biomarkers or the presence of EOAD genes (Mills et al., 2013; Reiman et al., 2011; Sperling et al., 2014). In addition to using anti-amyloid pharmaceuticals, another group of ongoing preventive trials are targeting the known lifestyle related risk factors of AD in multi-domain intervention trials (Ngandu et al., 2015; Vellas et al., 2014). The FINGER study has already reported a significant intervention effect in cognitive function after the initial 2-year intervention and an additional 5 years' follow-up has already been launched (Ngandu et al., 2015; Sindi et al., 2015).

2.5.3. *Functionalized nanoparticles as anti-amyloid drugs*

Multiple nanoparticles (NPs) with differing composition, size and shape, including (but not limited to) LIPs, polymeric nanoparticles, carbon nanotubes, micelles and gold nanoparticles, have been used for CNS drug development, mainly to increase the delivery of drugs to the brain (Vieira and Gamarra, 2016). The traditional way of exploiting nanotechnologies in treatment strategies has been to use them as "Trojan horses" i.e. nanocarriers that can bind active molecules, transport them across the BBB and thus increase their efficacy and/or reduce their unwanted effects. Various bioactive molecules with potential for AD treatment, such as the AChEI rivastigmine, and a metal chelating compound, MAEHP, have been incorporated to different nanocarriers to increase their efficacy and BBB penetration or reduce toxicity, respectively (Liu et al., 2009; Wilson et al., 2008).

The advances in nanotechnologies have meant that different nanomaterials now can be considered as a potential tool also for early diagnosis and treatment of AD. In addition to embedding active drug molecules within NPs, another approach is to design functionalized NPs that would have high affinity to selected therapeutic targets (e.g. Aβ) and thus therapeutic (and/or diagnostic) efficacy. For example, novel nanodevices with attached high affinity ligands for diagnostic biomarkers could be helpful in detecting soluble Aβ species or tau *in vitro* from blood or CSF samples, where concentrations are usually below the detection level of traditional analytical methods (Re et al., 2012). Nanoparticles could also be incorporated with contrast agents or radionuclides for *in vivo* MRI or PET/SPECT imaging purposes, respectively. Different features affecting the properties of NPs and examples of attached ligands for achieving different functionalities are presented in Figure 8.

LIPs are some of the most extensively investigated NP types for CNS applications. These particles are composed of bi-layers of naturally occurring lipids that surround an additional aqueous compartment, enabling the entrapment of both lipophilic and hydrophilic drugs into the particle. LIPs have favorable physicochemical properties and characteristics for use in human disease; they are biocompatible and physically stable, have low toxicity and good stealth characteristics, and can easily be further functionalized with peptides or lipids of interest (Gobbi et al., 2010; Re et al., 2011).

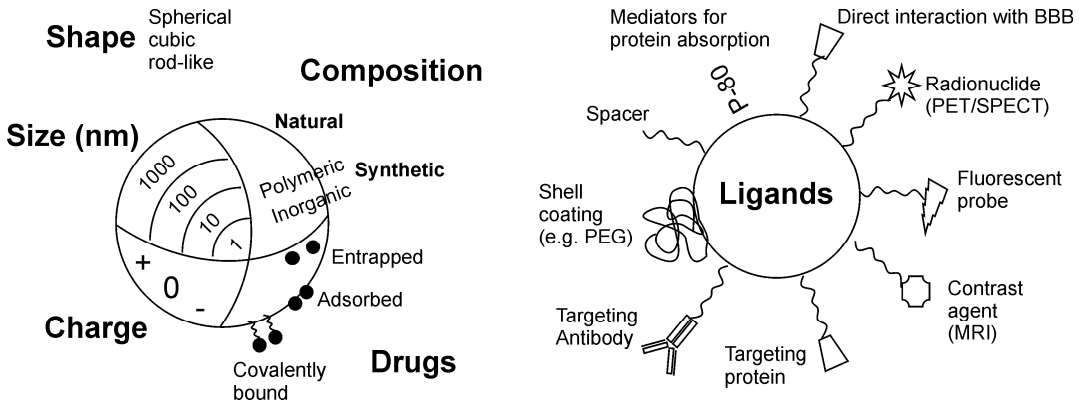

Figure 8. Main features that affect the properties of nanoparticles (NPs). Figure modified from Re et al., 2012 and Saraiva et al., 2016.

Bi-functionalized LIPs targeting Aβ, called *mApoE-PA-LIPs*, have recently been developed as a disease modifying treatment of AD (Balducci et al., 2014; Bana et al., 2014). The Aβ binding ligand in these LIPs is PA; it was initially recognized to bind $A\beta_{42}$ *in vitro*, and its subsequent attachment to LIPs was seen to lead to specific binding of these PA-LIPs to $A\beta_{42}$ fibrils and oligomers (Gobbi et al., 2010). Further studies investigating ways to increase the PA-LIP interaction with brain endothelial cells and ultimately to their crossing of the BBB, led to further functionalization of PA-LIPs with 141-150 amino acid fragment (mApoE) derived from receptor binding domain of human ApoE (Re et al., 2010; Re et al., 2011). *In vitro* studies conducted by Re and colleagues showed that mApoE functionalization increased the cellular uptake of PA-LIPs by caveolae-mediated mechanisms in comparison to LIPs without surface ApoE peptides (Re et al., 2011). In addition, further functionalization with mApoE was not seen to affect the Aβ binding when compared to PA-LIPs.

In the subsequent studies undertaken by Bana and colleagues, bi-functionalized mApoE-PA-LIPs were shown to cross human brain endothelial cell monolayers in an *in vitro* BBB model. As uptake into the cells was decreased when free mApoE was added, the authors suggested that a saturable internalization system, such as the low density lipoprotein receptor mediated pathway, was involved. In addition, radiolabelled mApoE-PA-LIPs were able to enter mouse brain, evidence of an ability to cross the BBB *in vivo.* mApoE-PA-LIPs were also seen to bind to $A\beta_{42}$ (K_d = 0.6 μM), and inhibit peptide aggregation and disaggregate already formed $A\beta_{42}$ aggregates (Bana et al., 2014). In addition, peripheral mApoE-PA-LIPs circulating in the blood have been suggested to clear oligomeric forms of Aβ from the brain by a sink effect (Mancini et al., 2016). Further *in vivo* studies using APP/PS1 tg mouse model of AD and dually fluorescently labelled LIPs confirmed that mApoE-PA-LIPs could cross the BBB in an intact form *in vivo* (Balducci et al., 2014). Remarkably, administration of mApoE-PA-LIPs also decreased soluble and insoluble $A\beta_{40}$ and $A\beta_{42}$ levels, the total amount of histologically confirmed Aβ deposits, and Aβ oligomers in the brain in comparison to the control group. In addition, the mApoE-PA-LIP treated mice performed better in novel object recognition, evidence of improved memory functions (Balducci et al., 2014). These observations further suggested that the mApoE-PA-LIPs could represent a novel and valuable disease modifying therapy for AD.

3. AIMS OF THE STUDY

The aim of this thesis was to evaluate the suitability of Aβ targeting PET tracers, [^{11}C]PIB and [^{18}F]flutemetamol, for longitudinal *in vivo* imaging of Aβ deposition in tg mouse models of AD. Another aim was to monitor the effects of a novel mApoE-PA-LIP intervention in a tg mouse model of Aβ deposition *in vivo*, and to validate the use of serial μPET amyloid imaging for future anti-amyloid evaluations.

The following specific objectives were set for the studies included in the thesis:

1. To perform a preliminary evaluation of the pharmacokinetic properties of a novel Aβ targeting PET tracer [^{18}F]flutemetamol in wt rats and mice, and its binding to Aβ in tg mouse brain *ex vivo* and *in vitro.* The results were further compared to [^{11}C]PIB, the present gold standard of Aβ PET imaging. According to the working hypothesis, [^{18}F]flutemetamol would demonstrate suitable properties for further animal imaging studies.
2. To investigate longitudinal temporal changes in Aβ deposition in the brain of APP23, Tg2576 and APP_{swe}-$PS1_{dE9}$ tg mouse models of AD using repeated *in vivo* PET imaging and [^{11}C]PIB produced with moderate SA. As previous imaging results using [^{11}C]PIB and these models had been confounding, the aim was to produce comparable imaging data using these three commonly used models. The working hypothesis was that [^{11}C]PIB with only moderate SA would not possess sufficient sensitivity to detect changes in Aβ deposition *in vivo*.
3. To investigate the effect of high SA for PET imaging of temporal changes in Aβ deposition in the brain of APP23, Tg2576 and APP_{swe}-$PS1_{dE9}$ tg mouse models of AD using [^{18}F]flutemetamol. Based on previous findings, the working hypothesis was that [^{18}F]flutemetamol produced with very high SA would have higher sensitivity, and thus it could be exploited in the longitudinal follow-up of Aβ deposition in tg mouse models.
4. To evaluate the therapeutic effect of novel functionalized mApoE-PA-LIPs for reducing/halting Aβ deposition in APP23 mouse model of AD, and the capability to detect the changes in Aβ load with longitudinal follow-up of individual mice using [^{11}C]PIB μPET imaging. According to working hypothesis, mApoE-PA-LIP treatment would halt Aβ deposition in the brain of treated tg mice, and this effect could be monitored *in vivo* using repeated [^{11}C]PIB μPET imaging.

4. MATERIALS AND METHODS

4.1. General experimental design

The pharmacokinetic profile of [^{18}F]flutemetamol and [^{11}C]PIB was evaluated in equivalent groups of weight matched experimental animals (**I**). The radiation dose estimates for human organs of interest were performed based on the *ex vivo* rat biodistribution data.

Studies **II** and **III** were longitudinal imaging studies with a repeated measurements design, where tg and wt animals were imaged with [^{11}C]PIB (**II**) or [^{18}F]flutemetamol (**III**) at multiple time-points. The experimental units were both individual animals that were imaged more than once, and the groups of animals imaged at various ages. The primary outcome was the temporal change in the [^{11}C]PIB and [^{18}F]flutemetamol binding ratios in brain areas affected by the Aβ pathology. Both studies were proof-of-principle studies aiming to examine the suitability of the clinically used PET tracers for preclinical experiments.

Study **IV** was a longitudinal follow-up study with one experimental and one control group. The experimental group received the investigated anti-amyloid intervention (mApoE-PA-LIPs) and the control group received vehicle only (physiological saline). Animals were allocated to groups based on their age by a person not involved in the study design and analysis. Each animal served as an experimental unit, and the primary outcome was the difference in the change in [^{11}C]PIB binding ratios between baseline and follow-up scans in a comparison between experimental and control groups. An additional follow-up three months after the treatment was added as previous studies had suggested a possible long-term effect of mApoE-PA-LIPs that could be investigated with use of the non-invasive PET method in the same individual mice. Analyses of the PET data were performed without the knowledge of the treatment status of the mice. A detailed study design for **IV** is presented in Figure 9.

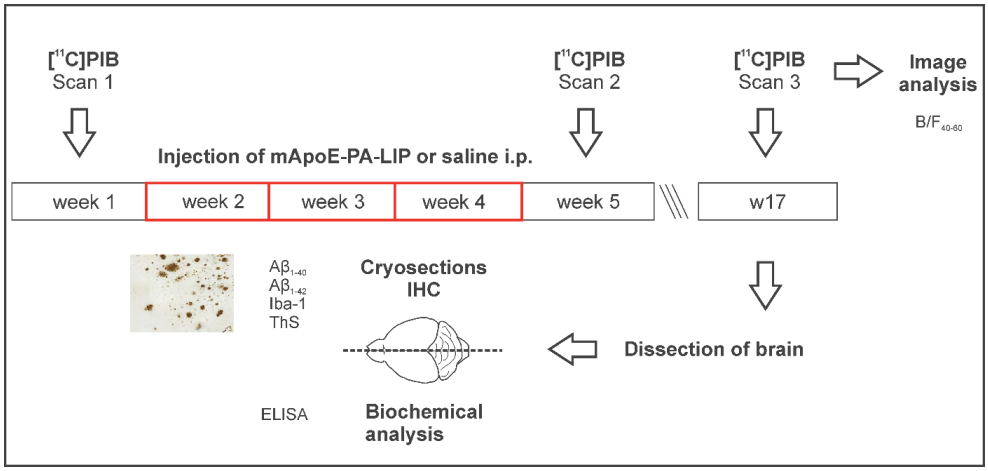

Figure 9. Experimental design for **IV**. $B/F_{40\text{-}60}$ = binding ratios for 40−60 min post injection; ELISA= enzyme linked immunosorbent assay; Iba-1 = Ionized calcium binding adaptor molecule 1; IHC = immunohistochemistry; PIB = Pittsburgh Compound B; ThS = Thioflavine S.

4.2. Experimental animals

All animal experiments were approved by the Animal Experiment Board of Finland (permissions ESAVI-2010-04454/Ym-23 and ESAVI/3899/04.10.07/2013) and conducted following the ethical guidelines provided by the International Council of Laboratory Animal Science (ICLAS).

Animals were group-housed (females) or individually housed (males) in the animal facility of the University of Turku where the temperature (21 ± 3 ºC), humidity (55 ± 15 %) and light-dark cycle (light period from 6 am to 6 pm) were controlled. Wt animals in **I** had free access to RM1 (E) chow (801002; Special Diets Service, Witham, UK) and tap water. Tg mice and their strain and age matched controls in **II−IV** were fed with a soy-free diet (RM3 (E) soya, 801710, Special Diets Service, Essex, UK) aiming to prevent excess weight gain of the aged animals. The numbers and details of animals used in studies **I−IV** are presented in Table 5.

Table 5. Animals used in **I−IV**. M = male; F = female; FMM =flutemetamol; mo = months. *n* = number of animals.

Study	Strain	Species	Genotype	*n*	Gender	Age (mo)	PET tracer	Intervention
I	C57Bl/6N	Mouse	wt	2	M	2	[^{11}C]PIB	-
				2	M	2	[^{18}F]FMM	-
	Sprague Dawley	Rat	wt	19	M	2	[^{11}C]PIB	-
				22	M	2	[^{18}F]FMM	-
	Tg2576	Mouse	tg	2	F	16; 22	[^{18}F]FMM	-
II	APP23	Mouse	tg	5	F, M	7–21	[^{11}C]PIB	-
		Mouse	wt	3	F	27	[^{11}C]PIB	-
	Tg2576	Mouse	tg	4	F	9–22	[^{11}C]PIB	-
		Mouse	wt	3	F	12–22	[^{11}C]PIB	-
	APP_{swe}-$PS1_{dE9}$	Mouse	tg	5	F	9–19	[^{11}C]PIB	-
		Mouse	wt	3	F	12–19	[^{11}C]PIB	-
III	APP23	Mouse	tg	6	F, M	9–21	[^{18}F]FMM	-
		Mouse	wt	4	F	27	[^{18}F]FMM	-
	Tg2576	Mouse	tg	4	F	9-22	[^{18}F]FMM	-
		Mouse	wt	3	F	12–22	[^{18}F]FMM	-
	APP_{swe}-$PS1_{dE9}$	Mouse	tg	7	F, M	9-19	[^{18}F]FMM	-
		Mouse	wt	3	F	12–19	[^{18}F]FMM	-
IV	APP23	Mouse	tg	5	M	16–21	[^{11}C]PIB	mApoE-PA-LIP
	APP23	Mouse	tg	7	F, M	16–21	[^{11}C]PIB	Saline

4.2.1. *Wild type animals*

Male Sprague Dawley rats were bred in the animal facility of the University of Turku and weighed 250−300 g at the time of experiments. Male C57Bl/6N mice were bred in the animal facility of the University of Turku and weighed 25−31 g at the time of experiments.

4.2.2. *Transgenic animal models*

APP23 mice

APP23 tg mice (APP23, Novartis Pharma Inc., Basel, Swizerland) and aged wt control mice were obtained from Mario Negri Institute for Pharmacological Research, Milan, Italy (**II−IV)**, and directly from Novartis Pharma Inc. (**IV)**. APP23 mice overexpress the human 751-isoform of APP_{swe} mutation driven by the neuron specific murine Thy-1 promoter (Sturchler-Pierrat et al., 1997). Plaque deposition starts at approximately 6 months from the FC and subiculum, progressing later to whole NC and HC. At the time when plaques are histologically detected, there is more $A\beta_{40}$ in comparison with $A\beta_{42}$ present in the brain, similar to the situation observed in humans (Sturchler-Pierrat and Staufenbiel, 2000). Most amyloid plaques are compact and congophilic, associated with inflammatory components and hyperphosphorylated tau in the surrounding neurites (Sturchler-Pierrat et al., 1997). Vascular amyloid and microhemorrhages can be found in APP23 mice older than one year (Winkler et al., 2001). Significant neuronal loss from 14% to 25% has also been reported in the CA1-region of the HC in 14−18 month old mice in comparison to wt control mice (Calhoun et al., 1998). A cognitive decline has been shown to precede Aβ deposition, as progressive deficits were seen in the Morris water maze starting at 3 months (Van Dam et al., 2003).

Tg2576 mice

Tg2576 mice (B6;SJL-Tg(APPSWE)2476Kha; Taconic Inc., stock nr. 001349-T) and their wt littermates were obtained from Taconic Farms Inc. for **I−III**. Tg2576 is one of the most widely used commercially available tg models carrying the most abundant 695-isoform of the APP_{swe} (Hsiao et al., 1996). In this model, 5-fold and 14-fold increases in $A\beta_{40}$ and $A\beta_{42}$ have been reported between young (2−8 months) and older (11−13 months) mice, and both senile plaques and diffuse deposits become apparent by 11−13 months with further elevated Aβ levels (Hsiao et al., 1996). Plaques are associated with reactive astrocytes and microglia and dystrophic neurites are surrounding the dense cores. From 9 months onwards, tg animals also show deficits in learning and memory associated to elevated Aβ deposition (Hsiao et al., 1996).

APP_{swe}-$PS1_{dE9}$ mice

APP_{swe}-$PS1_{dE9}$ mice (B6.Cg-Tg(APPswe,PSEN1dE9)85Dbo/Mmjax; The Jackson Lab,. JAX MMRRC stock 034832-JAX) and wt littermates were obtained from Jackson Laboratories Inc., MMRRC for **II−III**. In **III**, additional tg mice were received for *ex vivo* studies as a kind gift from Professor Heikki Tanila. APP_{swe}-$PS1_{dE9}$ model is an early-onset double tg model of β-amyloidosis expressing both chimeric human/mouse APP_{swe} and human PSEN1 with deletion of exon 9 (dE9). The expression of the transgenes is directed to CNS neurons by using independent mouse prion protein promoters. These mice express elevated levels of Aβ peptides, favoring $A\beta_{42}$ by specifically increasing its levels (Borchelt et al., 1996; Jankowsky et al., 2004). Aβ deposits appear in the brain at 6 months, and the plaque number increases greatly to 12 months (Garcia-Alloza et al., 2006; Jankowsky et al., 2004). Plaques have been reported to exist mainly in cortical and hippocampal regions up to 12 months, and to spread to other brain regions as the animal ages (Garcia-Alloza et al., 2006; Savonenko et al., 2005). Aβ deposition is also present in the CB in older aged mice (Brendel et al., 2015a; Sérrière et al., 2015) Astrocytosis, gliosis and changes in synaptic plasticity are present in the brain, whereas NFTs are absent. Young tg mice have a high probability for suffering epileptic seizures, and this accounts for the sudden deaths of some young tg mice (Minkeviciene et al., 2009).

Impaired spatial learning evaluated with the Morris water maze has been reported at 12 months (Lalonde et al., 2005). No neuronal or synaptic loss has been reported in this model.

4.3. Interventions (IV)

In **IV**, the animals received i.p. injections of either the mApoE-PA-LIPs (n = 5) or saline (n = 7) three times per week (Monday, Wednesday and Friday) for a period of three weeks. All animals were injected in the morning between 9 and 11 by the same individual, not responsible for study design or analysis of the results. mApoE-PA-LIPs were prepared as previously described (Balducci et al., 2014). A fresh mApoE-PA-LIP solution was prepared weekly and stored at + 8ºC prior to use. The total lipid concentration of mApoE-PA-LIPs was 15.6 ± 0.5 mM (n = 3) based on sphingomyelin content. The size of the LIPs before the mApoE functionalization was 190 ± 18 nm (n = 3) with a polydispersity index < 0.35. The final functionalization of the LIPs with mApoE peptide residue was performed as previously described (Re et al., 2010).

4.4. Production of PET radionuclides and tracers (I−IV)

The radionuclides being used, ^{11}C and ^{18}F were produced in the Accelerator Laboratory of Turku PET Centre using their CC-18/9 cyclotron (Efremov Scientific Institute of Electrophysical Apparatus, St. Petersburg, Russia, **III−IV**) and the particle accelerator MGC-20 (Efremov Scientific Institute of Electrophysical Apparatus, **I−II**), in the following nuclear reactions:

$$^{14}\text{N (p, α) } ^{11}\text{C} \qquad\qquad ^{18}\text{O (p, n) } ^{18}\text{F}$$

[^{11}C]PIB and [^{18}F]flutemetamol were synthetized at the Radiopharmaceutical Chemistry Laboratory of Turku PET Centre as described in **I−IV**. The batches used for **I−IV** are presented in Table 6.

Table 6. Produced PET tracers for **I−IV**. SA = specific activity; EOS = end of synthesis; Inj = at the time of injection; RCP = radiochemical purity; n = number of produced batches.

Study	Radiotracer	n	SA_{EOS} (GBq/µmol)	SA_{Inj} (GBq/µmol)	RCP (%)
I	[^{11}C]PIB	13	50 ± 11	17 ± 5	> 95
	[^{18}F]flutemetamol	8	1460 ± 1160	980 ± 480	> 98
II	[^{11}C]PIB	45	100 ± 27	50 ± 15	> 95
III	[^{18}F]flutemetamol	34	> 1000	> 342	> 92
IV	[^{11}C]PIB	13	1200 ± 215	640 ± 120	> 99

4.5. *In vivo* PET imaging (I−IV)

In **I−IV**, *in vivo* dynamic PET/computed tomography (CT) scans were performed with the Inveon Multimodality PET/CT device (Siemens Medical Solutions, Knoxville, TN, USA). The scanner offers a 10 cm transaxial and 12.7 cm axial field-of-view (FOV) with a spatial resolution of approximately 1.5 mm and 10% sensitivity in the center of the FOV, according to the manufacturer. Transmission scans using the CT modality were first performed for anatomical reference purposes and for attenuation correction of the PET data. Dynamic PET recordings in 3D list mode were initiated at the time of radiotracer injection and collected for 60 min in all studies. PET data were recorded as 3D sinograms with 350−650 keV energy window, dynamic data were divided into 51

time frames and reconstructed using specific reconstruction protocols chosen for each study. The used PET work flow is visualized in Figure 10, and the imaging protocols are presented in Table 7.

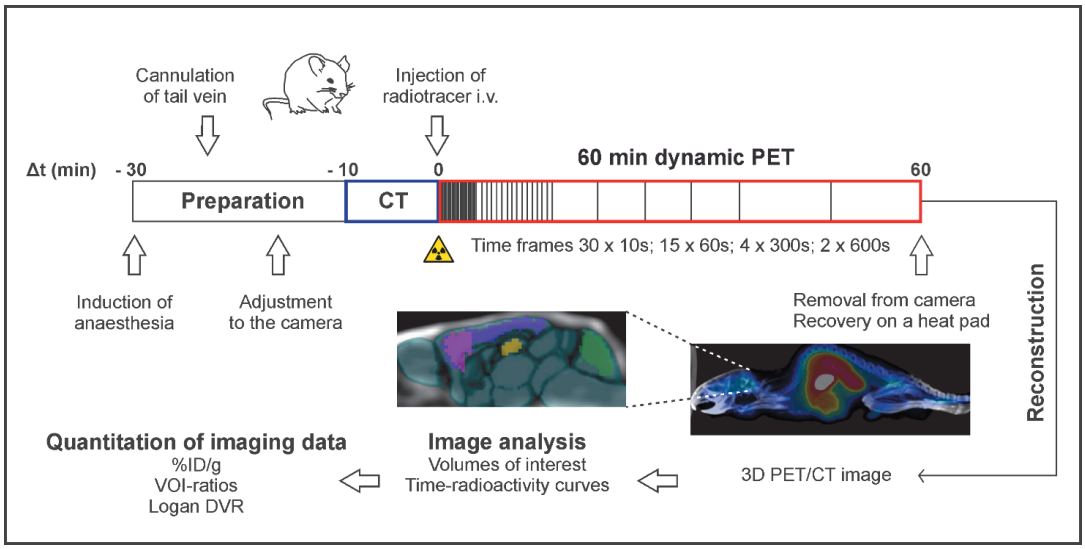

Figure 10. Workflow for the *in vivo* PET experiments in **I–IV**. VOI = volume of interest; DVR = distribution volume ratio; % ID/g = percentage of injected dose per gram of tissue.

Analysis of the data was volumes of interest (VOI) based and performed with the Inveon research Workplace –software (Siemens Medical Solutions); in **I**, VOIs were manually drawn around the left ventricle of the heart to estimate the radioactivity present in blood, liver, intestine, kidneys and whole brain to obtain time-radioactivity curves (TACs) for each VOI. In **II–IV**, VOIs were manually drawn for whole brain, frontal cortex (FC), neocortex (NC), cerebellum (CB), and pons (PO), as illustrated in Figure 11. Drawing of VOIs was guided by either the accumulated radioactivity to the organ of interest (**I**), the anatomy based on the CT image and the stereotactic mouse brain atlas (Franklin and Paxinos, 2008) (**I–III**), or an external MRI template of a mouse brain (**IV**).

Table 7. Details from the dynamic PET studies performed in **I–IV.** 2D-FBP = two-dimensional filtered back-projection; B/F = bound-to-free –ratio; CB = cerebellum; DVR = distribution volume ratio; FC = frontal cortex; IA = injected activity; NA = not available; OP-OSEM = ordinary Poisson ordered-subset expectation maximization; PO = pons; tg = transgenic; wt = wild type.

Study	PET tracer	*n*	Species	Strain	IA (MBq)	Reconstruction	Quantification	Ref. region
I	[^{11}C]PIB	2	mouse	C57Bl/6N	8.0; 9.0	Fourier rebinning, 2D-FBP	%ID/g	NA
	[^{18}F]flutemetamol	4	rat	Sprague-Dawley	34 ± 2	Fourier rebinning, 2D-FBP	%ID/g	NA
		2	mouse	C57Bl/6N	2.5; 3.5	Fourier rebinning, 2D-FBP	%ID/g	NA
II	[^{11}C]PIB	9	mouse	APP23 tg	8.5 ± 2.1	Fourier rebinning, 2D-FBP	FC/CB; B/F$_{40\text{-}60;}$ DVR	CB, PO
		2	mouse	APP23 wt	8.7; 8.6	Fourier rebinning, 2D-FBP	FC/CB; B/F$_{40\text{-}60;}$ DVR	CB, PO
		12	mouse	Tg2576 tg	8.3 ± 1.0	Fourier rebinning, 2D-FBP	FC/CB; B/F$_{40\text{-}60;}$ DVR	CB, PO
		5	mouse	Tg2576 wt	8.6 ± 0.6	Fourier rebinning, 2D-FBP	FC/CB; B/F$_{40\text{-}60;}$ DVR	CB, PO
		8	mouse	APP$_{swe}$-PS1$_{dE9}$ tg	9.0 ± 0.7	Fourier rebinning, 2D-FBP	FC/CB; B/F$_{40\text{-}60;}$ DVR	CB, PO
		7	mouse	APP$_{swe}$-PS1$_{dE9}$ wt	9.3 ± 1.3	Fourier rebinning, 2D-FBP	FC/CB; B/F$_{40\text{-}60;}$ DVR	CB, PO
III	[^{18}F]flutemetamol	7	mouse	APP23 tg	3.6 ± 0.8	Fourier rebinning, 2D-FBP	FC/CB, DVR	CB
		2	mouse	APP23 wt	6.0; 5.4	Fourier rebinning, 2D-FBP	FC/CB, DVR	CB
		14	mouse	Tg2576 tg	4.4 ± 0.8	Fourier rebinning, 2D-FBP	FC/CB, DVR	CB
		8	mouse	Tg2576 wt	4.3 ± 1.0	Fourier rebinning, 2D-FBP	FC/CB, DVR	CB
		9	mouse	APP$_{swe}$-PS1$_{dE9}$ tg	3.9 ± 0.6	Fourier rebinning, 2D-FBP	FC/CB, DVR	CB
		8	mouse	APP$_{swe}$-PS1$_{dE9}$ wt	4.3 ± 1.0	Fourier rebinning, 2D-FBP	FC/CB, DVR	CB
IV	[^{11}C]PIB	21	mouse	APP23 tg	10.3 ± 0.5	OP-OSEM-3D	B/F$_{40\text{-}60}$	CB

	Anatomic Ref.	FC (mm^3)	NC (mm^3)	CB (mm^3)	HC (mm^3)	PO (mm^3)
II	CT, brain atlas	46 ± 16	131 ± 20	12 ± 4	NA	8 ± 3
III	CT, brain atlas	46 ± 13	130 ± 19	10 ± 5	NA	9 ± 4
IV	CT, MRI template	15	64	21	12	NA

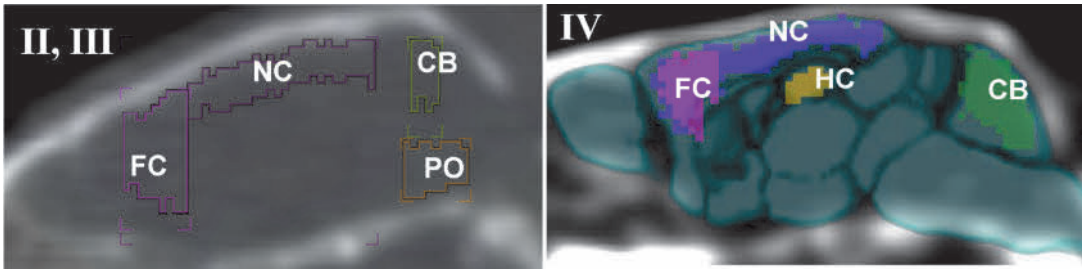

Figure 11. Volumes of interest drawn to different mouse brain regions in **II–IV.** CB = cerebellum; CT = computed tomography; FC = frontal cortex; HC = hippocampus; MRI = magnetic resonance imaging; NC = neocortex; PO = pons.

4.6. *Ex vivo* methods

4.6.1. *Biodistribution studies (I, III)*

Results from dynamic *in vivo* studies were verified with *ex vivo* tissue counting measurements from organs of interest at specific time points. In **I**, Sprague Dawley rats were briefly anesthetized with CO_2/O_2 (50/50 vol %), the investigated PET tracers were injected into the tail vein, and allowed to distribute for 5, 15, 30, 60 or 120 min. Subsequently, the animals were sacrificed with CO_2 inhalation and tissues of interest were collected, weighed and measured for their radioactivity using NaI(TI) well counter (3 x 3-inch; Bicron, Newbury, OH). In **III**, C57Bl/6N mice were anesthetized with 2.5% isoflurane/air mixture, [^{18}F]flutemetamol was injected i.v. and allowed to distribute for 60 min. Mice were sacrificed by cardiac puncture while under deep isoflurane anesthesia, brains were removed, and brain areas of interest were dissected. Samples were weighed and radioactivity measured using a gamma counter (2480 Wizard^2, Perkin Elmer, Turku, Finland). Measurements were corrected for the weight of the organ, decay and background activity, and finally expressed as a percentage of the injected dose per gram of tissue (% ID/g).

4.6.2. *Binding to tissue sections (I–III)*

In **I**, tracer binding was also evaluated from rat brain cryosections, to investigate the non-specific binding of the tracers in various brain areas. In **I–III**, similar experiments were performed with tg mice to validate the specific binding of the tracer to Aβ deposits in the brain. Investigated time points were 10 and 30 min for tg mice after [^{11}C]PIB (**I–II**) or [^{18}F]flutemetamol (**I, III**) injections, respectively, and 5, 15, 30 and 60 min for wt rats (**I**). Brains were rapidly removed and freshly frozen by immersion in isopentane chilled on dry ice. Subsequently 20 µm coronal sections were cut with cryomicrotome from various brain areas of interest. Sections were collected to microscope slides, dried, exposed to imaging plates (Fuji imaging plate BAS-TR2025; Fuji Photo Film Co., Tokyo, Japan) and scanned with Fuji Analyzer BAS-5000 (Fuji Photo Film Co., Tokyo, Japan) resulting in 25 µm image resolution. Digital images of the radioactivity distribution in the sections were analyzed by comparing count densities as photostimulated luminescence intensity per square millimeter

(PSL/mm^2) between areas of interest (**I**), or by calculating regions of interest (ROI) –ratios (**I−III**) after subtracting background activity from each ROI. In the ratios, CB was used as a reference area. In **I**, ROIs were drawn to striatum, corpus callosum, parietal cortex, cerebellar grey matter, cerebellar white matter and immunohistochemically verified Aβ deposits. In **II−III**, ROIs were drawn to FC and CB, at approximately 2 mm and -7 mm from Bregma, respectively. All images were analyzed using Aida Image analyzer v.4.19 (Raytest, Isotopenmessgeräte, Staubenhardt, Germany).

4.6.3. *Radiometabolite analysis (I)*

Radioactive metabolites of [^{11}C]PIB and [^{18}F]flutemetamol were analyzed from plasma and brain homogenates of Sprague Dawley rats and C57Bl/6N mice by thin layer chromatography (TLC) and digital autoradiography. Digital images of plates were analyzed with Aida Image analyzer v.4.19 for proportions of parent tracer, its radioactive metabolites and their R_f values.

4.6.4. *Binding to plasma proteins (I)*

An ultrafiltration method was used to study the proportions of tracers and their radioactive metabolites bound to proteins in plasma. Plasma samples were added to Filtron Microsep 30K ultrafiltration tubes (Filtron Technology Corporation, Northborough, MA) and centrifuged 2 × 15 min (3030 g) to separate free tracers from the protein bound fraction remaining on the filter.

4.7. *In vitro* methods

4.7.1. *Binding to tissue sections (I, III)*

In **I** and **III**, [^{11}C]PIB and [^{18}F]flutemetamol binding to tg mouse brain sections was evaluated using *in vitro* binding experiments and digital autoradiography. 20 µm mouse brain sections were pre-incubated in 2% human serum albumin in phosphate buffer (pH 7.4) prior to 30 min incubation in 0.5 MBq/ml [^{11}C]PIB (**I**) or [^{18}F]flutemetamol (**I, III**) solution. The specificity of tracer binding to Aβ in the brain sections was evaluated by adding 10 µM non-radioactive PIB to the incubation solution. After incubation, sections were washed, dried and the binding of ^{11}C- and ^{18}F-radioactivity was measured using digital autoradiography as previously described for *ex vivo* studies.

4.7.2. *Immunofluorescence and immunohistochemistry (I−IV)*

Immunofluorescence (IF) and immunohistochemical (IHC) stainings were performed for mouse brain cryosections in all studies. In **I−III,** 20 µm coronal cryosections were prepared as described before. The sections were first used for *ex vivo* or *in vitro* digital autoradiography and then stored at -20ºC for subsequent staining. In **IV**, 14 µm serial sagittal cryosections were cut from frozen left hemispheres, and stored at -20 ºC before staining.

Fresh frozen sections were first post-fixed in 4% paraformaldehyde for 30 min. ThS staining was carried out as described in **I**. For anti-Aβ staining, epitope retrieval with 88−100% formic acid for 10 min was performed before incubation in a blocking solution (2% BSA, 2% NGS, 0.3% Triton X-100 in PBS, pH 7.4) for 30 min. In the ionized calcium binding adaptor molecule 1 (Iba-1) staining, endogenous peroxidase was additionally blocked with 0.3% hydrogen peroxidase in methanol prior to blocking. The used primary antibodies and dyes are listed in Table 8.

Table 8. Primary antibodies and dyes used in **I–IV**. Mc = monoclonal antibody; Pc = polyclonal antibody, RT = room temperature, O/N = overnight

Study	Name	Type	Reactivity to	Dilution	Incubation	Origin and Cat.
I–IV	Thioflavine S	Dye	Fibrillar amyloid	0.015 %	10 min, RT	Sigma-Aldrich; T1892
II–IV	Anti-$A\beta_{40}$	Pc	$A\beta_{40}$	1:400, 1:300	48h, +8ºC	Millipore; AB5074P
IV	Anti-$A\beta_{42}$	Pc	$A\beta_{42}$	1:400	48h, +8ºC	Millipore; AB5078P
II	Anti-$A\beta_{N3(pE)}$	Mc	$A\beta_{N3(pE)}$	1:400	48h, +8ºC	Antibodies-online GmbH; ABIN459385
I, II	6E10	Mc	$A\beta_{16}$	1:400	48h, +8ºC	Covance Inc.; SIG-39320
IV	Anti-Iba1	Pc	Ionized calcium binding adapter molecule 1	1:1000	O/N, +8ºC	Wako Pure Chemical Industries, Ltd; 019-19741

For IF, washed sections were incubated 60 min RT with goat anti-mouse IgG fluorescent secondary antibody (Alexa Fluor® 568, 1:500, Invitrogen) and 4´-6-diamidino-2-phenylindole as the nuclear counterstain. Immunoreactivity was assessed using a DMR microscope (Leica, Heerbrugg, Germany) with fluorescent filters.

For IHC, washed sections were incubated for 60 min RT with biotin-conjugated goat anti-rabbit secondary antibodies (Jackson Immuno Research Laboratories, Inc. (**II, III**); Invitrogen, Camarillo; CA, USA (**IV**)) and avidin-peroxidase conjugate (Vestastain ABC kit, Vector laboratories, Burlingame, CA, USA).

4.7.3. *Biochemical analysis of Aβ (IV)*

The $A\beta_{40}$ and $A\beta_{42}$ concentrations in tg APP23 brain tissue homogenates were quantified with use of solid phase sandwich enzyme-linked immunosorbent assays (ELISA). Right brain hemisphere was dissected into CB and forebrain, weighed, snap frozen in liquid nitrogen and stored at -70 ºC. Subsequently, the samples were homogenized in PBS (pH 7.4) containing protease inhibitor cocktail (cOmplete™, Roche, Mannheim, Germany) and ultra-centrifuged for 3 h (100 000 g) to separate the PBS-soluble fraction of Aβ from the PBS-insoluble fraction. The insoluble fraction was further homogenized in 5 M guanidine HCl/50 mM Tris-HCl (pH 8.0) solution including a protease inhibitor cocktail, agitated for 3 h and stored at -70 ºC before use. The amount of $A\beta_{40}$ and $A\beta_{42}$ from the samples was quantified according to the protocol of the used ELISA assay kits (Human $A\beta_{40}$ ELISA (Cat: KHB348) and Human $A\beta_{42}$ ELISA (Cat. KHB344), Thermo Fisher Scientific, Waltham, MA, USA).

4.8. Radiation dose estimations (I)

Radiation dose estimates and effective doses for an adult male (73 kg) were calculated for [^{11}C]PIB and [^{18}F]flutemetamol from rat *ex vivo* biodistribution data using Olinda/Exm 1.0 software (Radar, USA) as reported in **I**.

4.9. Statistical analysis

Results are presented as means ± standard deviation (SD). In all studies, statistical analyses were performed with GraphPad Prism program v 5.01 (GraphPad software, Inc., La Jolla, CA, USA), except in **IV**, where differences in binding ratios over time between mApoE-PA-LIP and saline groups and within groups were tested with the hierarchical linear mixed models, and SAS® System, v 9.4 for Windows (SAS Institute Inc., Cary, NC, USA). Differences between ages, injected doses, injected mass, SA, baseline binding ratios and VOI volumes between tg and wt mice or mApoE and saline groups were evaluated using unpaired t-tests (**II−IV)**. [^{11}C]PIB and [^{18}F]flutemetamol binding ratios from the same individual mice were compared using paired t-test (unpublished data). A linear regression analysis was performed to evaluate the correlation of the different quantification methods (**III**). The correlation between PET tracer retention and quantitated Aβ plaque load was tested with Pearson's correlation coefficient (**IV**). *P*-values less than 0.05 (two-tailed) were considered statistically significant.

5. RESULTS

5.1. Characterization of the AD mouse models

APP23 mice showed a relatively slow rate of Aβ pathology, and were seen to first acquire sparse immunodetectable Aβ and Thioflavine S (ThS) positive fibrillar deposits in the cortical areas at 12 months and the deposition heavily increased with age. At 20−27 months, large fibrillar deposits were seen abundantly around NC, HC and thalamus, whereas deposits were absent in the striatum and CB (**II**−**IV**). In the cortical areas, deposits were large, dense-cored and ThS positive and activated microglia surrounded the deposits at 20 months (unpublished results). APP23 mice also showed immunodetectable N-terminally truncated pyroglutamated forms of Aβ in the NC at 18 months (**II**).

Tg2576 mice showed the slowest Aβ deposition rate, initially sparse small fibrillar deposits were observed only at 15 months, and even at 22 months the plaque load in the FC was modest (**I**−**III**). At 22 months, deposits were seen in NC, HC and thalamus, whereas striatum and CB were preserved. In Tg2576 brain, 6E10 staining dominated over ThS positive fibrillar Aβ (**II**, Fig. 7). At 6 months, no signs of neuroinflammation were present, but at 17 months, activated microglia were detected around the cortex in close proximity to the Aβ deposits (unpublished results). No N-terminally truncated pyroglutamated forms of Aβ were detected (**II**).

APP_{swe}-$PS1_{dE9}$ mice presented the quickest onset and fastest progression of Aβ pathology: 6E10 positive Aβ deposits were observed at 6 months in the cortex and HC, and the amount of plaques markedly increased to the last evaluated time point at 19 months (**II**−**III**). The deposits were abundant but small, focal and less intensively stained with ThS. Activated microglia was present around Aβ deposits already at 6 months, increasing in number with the severity of plaque pathology (unpublished results). No N-terminally truncated pyroglutamated forms of Aβ were detected (**II**).

Representative cortical images of the AD-like changes in the brain of aged tg APP23, Tg2576, and APP_{swe}-$PS1_{dE9}$ mice are summarized in Figure 12.

5.2. Pharmacokinetics of [^{11}C]PIB and [^{18}F]flutemetamol

5.2.1. *Biodistribution*

TACs for various organs of interests showed similar distribution of [^{11}C]PIB and [^{18}F]flutemetamol in Sprague Dawley rats *in vivo* (**I**): Both tracers were rapidly removed from blood, and uptake in the brain was fast as ^{11}C- and ^{18}F-radioactivity peaked at 2 min post-injection (p.i.). In the absence of Aβ deposits, both tracers were rapidly removed from the brain, however, clearance of [^{18}F]flutemetamol was slower than with [^{11}C]PIB (**I**, Fig. 2). Subsequently, both tracers were taken up into the liver and kidneys, and excreted mainly via the hepatobiliary pathway. *In vivo* distribution of both [^{11}C]PIB and [^{18}F]flutemetamol was similar in mice than in rats, and no clear difference in tracer uptake in the peripheral tissues was seen between old tg and old wt mice (unpublished data). Figure 13 presents the distribution of [^{11}C]PIB and [^{18}F]flutemetamol in Sprague Dawley rats, old wt C57Bl/6N mice, and old tg APP23 mice.

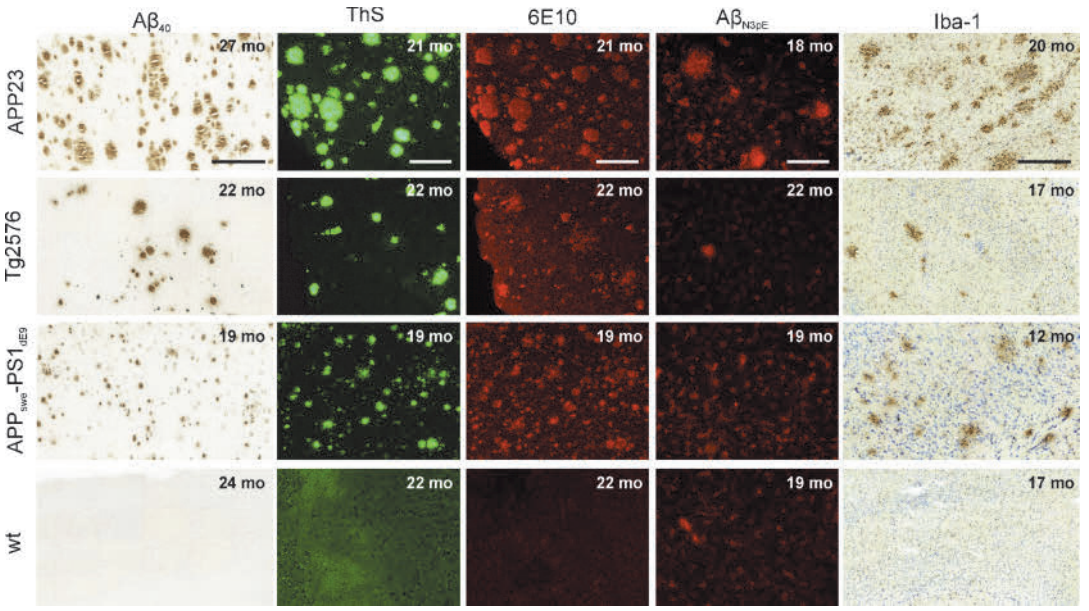

Figure 12. AD-like pathology in the brain of APP23, Tg2576 and APP_{swe}-$PS1_{dE9}$ mice. Representative 10 x microscope captions of the ongoing cortical Aβ pathology and microgliosis evaluated by various specific antibodies and Thioflavine S (ThS) dye in transgenic and wild type (wt) mice. Scale bars 200 µm. Aβ = beta-amyloid; mo = months; 6E10 = monoclonal anti-$Aβ_{1-16}$ antibody; Iba-1 = ionized calcium binding adapter molecule 1.

Ex vivo measurements verified the high initial uptake and fast clearance from the brain: Brain-to-blood ratios were 4.8 and 12.2 at 5 min, and 1.1 and 1.0 at 60 min for [^{11}C]PIB and [^{18}F]flutemetamol, respectively. At later time points, ^{11}C-and ^{18}F-radioactivity accumulated in the liver and intestine (**I**, Table 1). In Sprague Dawley rats, the measured ^{18}F-radioactivity in cranial bone was low (0.04 ± 0.01 % ID/g, n = 3 at 60 min p.i.) and temporally stable (**I**). However, in mice, ^{18}F-radioactivity in the cranial bone at 60 min was 0.83 ± 0.13 %ID/g (n = 4), and significantly higher than in rats ($p < 0.001$, unpaired t-test, unpublished results). This difference was not detectable *in vivo*.

Effective dose estimates for adult human 73-kg male subject extrapolated from the rat *ex vivo* biodistribution data were 2.28 µSv/MBq and 6.65 µSv/MBq for [^{11}C]PIB and [^{18}F]flutemetamol, respectively. The highest received doses were detected in small intestine (11.30 and 58.70 µSv/MBq), followed by liver (7.95 and 13.70 µSv/MBq) and kidneys (5.49 and 12.10 µSv/MBq) for both [^{11}C]PIB and [^{18}F]flutemetamol.

5.2.2. *Metabolism and binding to plasma proteins*

[^{11}C]PIB and [^{18}F]flutemetamol were both rapidly metabolized into multiple more polar radioactive metabolites, and the metabolized fraction in rat plasma increased with time (**I**, Fig. 6). At 60 min, unchanged [^{11}C]PIB and [^{18}F]flutemetamol comprised only 9% and 3% of the total radioactivity in plasma, respectively. In Sprague Dawley rats, radioactive metabolites of [^{11}C]PIB and [^{18}F]flutemetamol were detected also in brain homogenates. In C57Bl/6N mice, only unchanged [^{11}C]PIB and [^{18}F]flutemetamol were present in the brain. Both unchanged parent compounds and

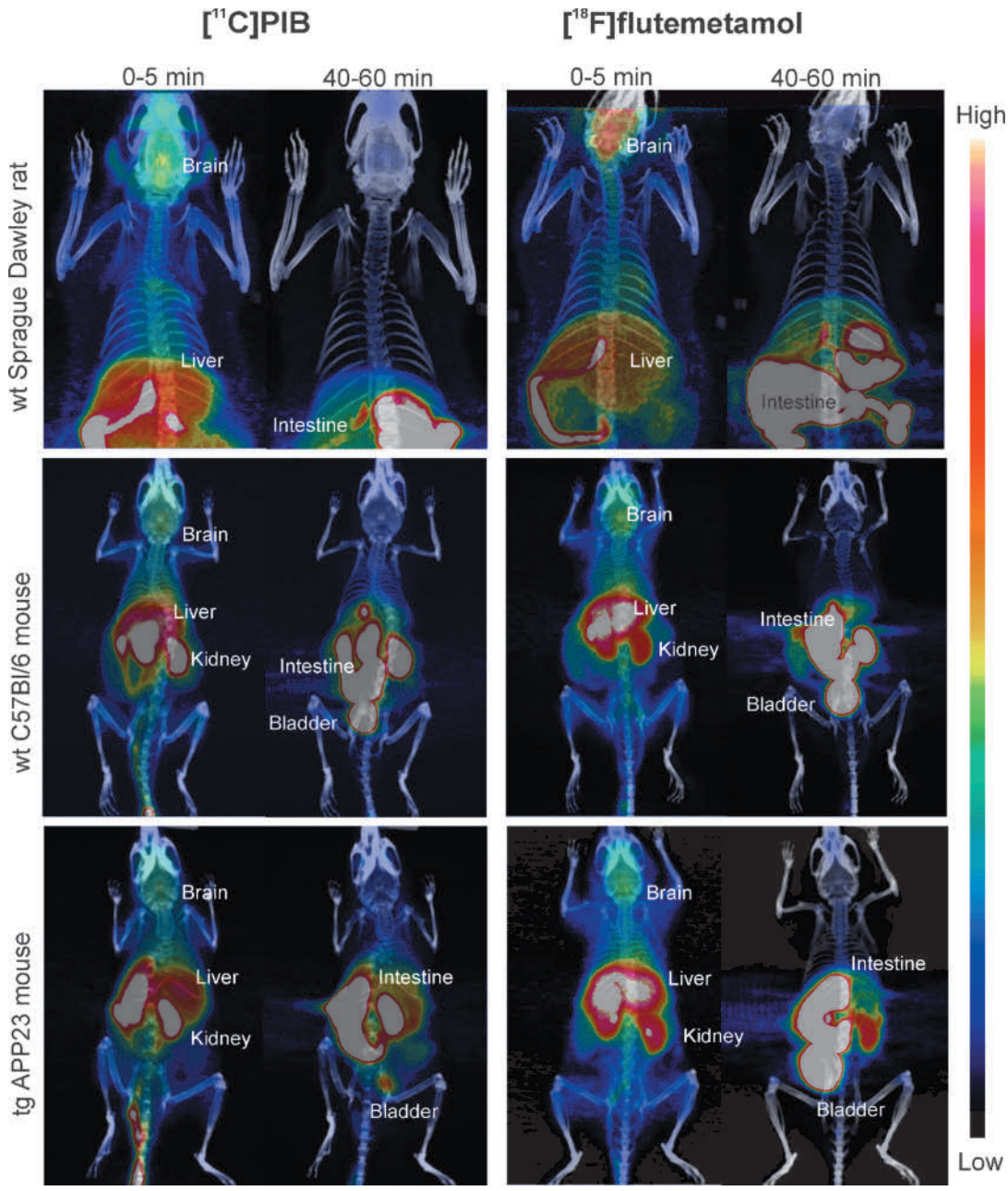

Figure 13. Whole body *in vivo* biodistribution of [^{11}C]PIB and [^{18}F]flutemetamol in Sprague Dawley rat, old wild type (wt) mouse, and old transgenic (tg) APP23 mouse. Images are summed during the early (0−5 min post injection) and late phase (40−60 min post injection) of the dynamic PET scan. Both tracers showed rapid entrance to brain and uptake into liver and kidneys. In the later phase, ^{11}C- and ^{18}F-radioactivity was mainly accumulated in the intestine and urine.

their radioactive metabolites were largely bound to plasma proteins: Free fraction of ^{11}C-radioactivity at 5 min p.i. was only 7% and free ^{18}F-radioactivity comprised only approximately 1% of the total ^{18}F-radioactivity at every investigated time point.

5.3. Binding of [^{11}C]PIB and [^{18}F]flutemetamol to Aβ in AD mouse models

5.3.1. *In vivo follow-up of Aβ deposition*

In **II**, cortical increases in [^{11}C]PIB retention were observed in aged tg APP23 mice (15−21 months) compared to young APP23 mice (7−12 months) and wt mice. At 12 months, [^{11}C]PIB retention in the area of interest (FC) was equivalent to the reference area lacking Aβ deposition (CB). The FC/CB ratio was first seen to rise at 15 months, and it further increased at 18 months (**II**, Fig. 1). No such increase was seen in the brain of aged Tg2576 or APP$_{swe}$-PS1$_{dE9}$ mice.

In **III**, increased [^{18}F]flutemetamol binding was only visible in the brain of aged APP23 mice (**III**, Fig. 1). However, FC/CB ratios were lower than those calculated for [^{11}C]PIB, due to higher non-specific binding to white matter in the reference region (**III**, Fig. 3). In Tg2576 and APP$_{swe}$-PS1$_{dE9}$ models, no equally clear changes in brain [^{18}F]flutemetamol retention were observed between young and old tg mice.

For easier comparison of the results emerging from **II** and **III**, similarly quantified cortical [^{11}C]PIB and [^{18}F]flutemetamol binding at 12 and 18−22 months is presented in Table 9. Figure 14 presents the cortical retention of [^{11}C]PIB and [^{18}F]flutemetamol in representative aged APP23, Tg2576 and APP$_{swe}$-PS1$_{dE9}$ mice.

Table 9. Quantified [^{11}C]PIB and [^{18}F]flutemetamol binding ratios for frontal cortex (FC) in APP23, Tg2576 and APP$_{swe}$-PS1$_{dE9}$ mouse models of AD. For $n \geq 3$, mean ± SD is presented. For $n \leq 2$, individual values are presented separated by a semi-column. * FC/CB is calculated from the last imaging frame, i.e. 50−60 min after tracer injection. B/F = bound-to-free; CB = cerebellum; DVR = distribution volume ratio; mo = months.

		[^{11}C]PIB (II)			[^{18}F]flutemetamol (III)		
	Age (mo)	**FC/CB ***	**Logan DVR**	**B/F$_{40-60}$**	**FC/CB***	**Logan DVR**	**B/F$_{40-60}$**
APP23	12	1.1; 1.3	1.1; 0.9	0.1; 0.1	0.9	1.0	-0.05
	18	1.8 ± 0.4	1.4 ± 0.03	0.8 ± 0.2	1.4; 1.2	1.4; 1.1	0.4; 0.1
Tg2576	12	1.2; 1.1	1.0; 0.9	0.03; 0.1	0.8 ± 0.1	0.9 ± 0.2	-0.2 ± 0.1
	22	0.9; 1.2	1.1; 0.9	0.1; -0.1	1.0; 0.9	1.2; 1.1	-0.01; -0.1
APP$_{swe}$-PS1$_{dE9}$	12	1.0; 1.4	1.0; 1.1	0.1; 0.2	0.9 ± 0.1	0.9 ± 0.02	-0.1 ± 0.1
	19	1.0; 1.0	1.0; 1.0	-0.1; -0.04	1.0; 0.9	0.8; 0.9	-0.1; -0.1

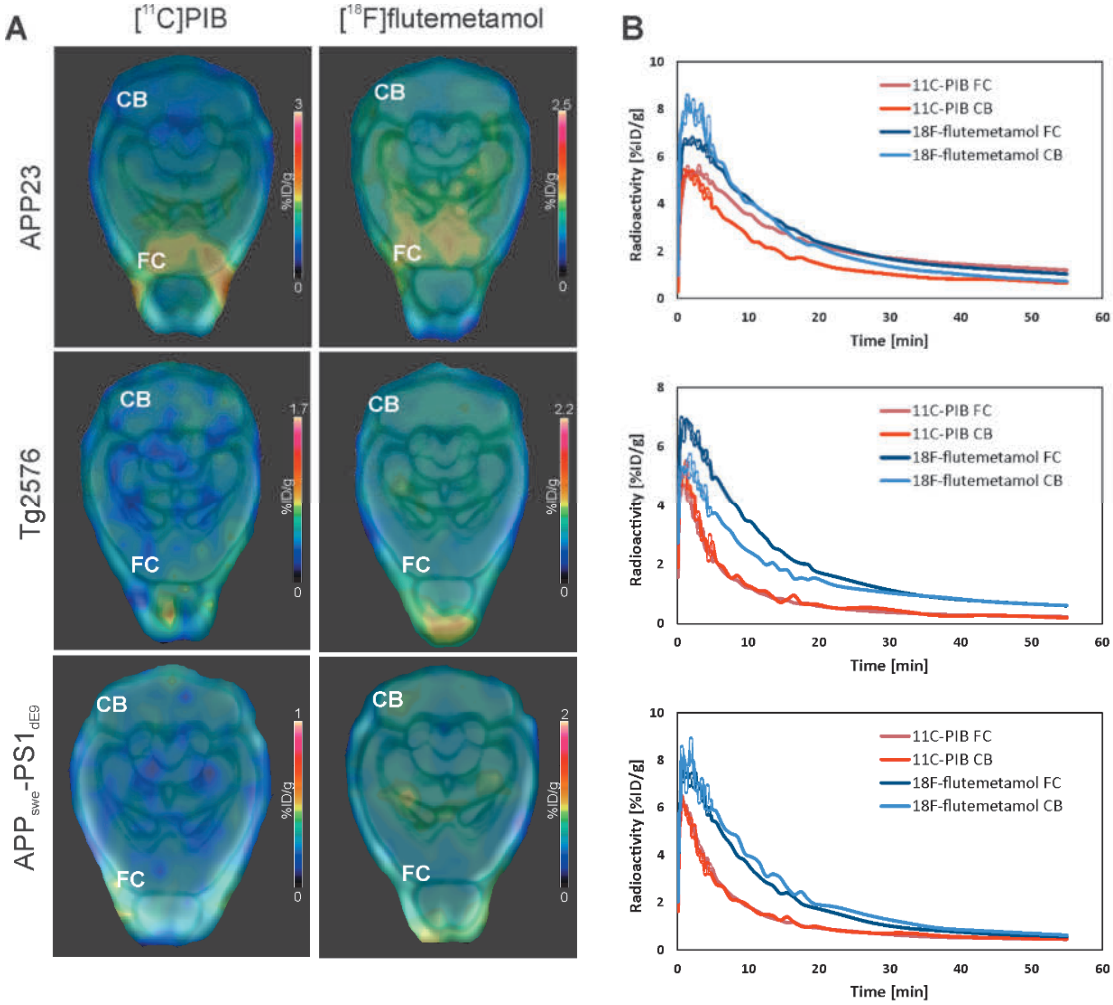

Figure 14. [^{11}C]PIB and [^{18}F]flutemetamol retention in the brain of old APP23 (18−21 months), Tg2576 (22 months) and APP$_{swe}$-PS1$_{dE9}$ mice (19 months). **A.** All PET images are summed images of 40−60 min after tracer injection, co-registered to a CT-image of the same mouse, and a general mouse brain MRI template. Despite ongoing β-amyloidosis in the brain occurring in all three models, increased retention of tracers was seen only in transgenic APP23 mice. **B.** Time radioactivity curves obtained from the PET images reveal the uptake and clearance of the tracers from frontal cortex (FC) and cerebellum (CB).

In study **II**, quantified [^{11}C]PIB binding in the FC was seen to correlate with the temporal increase in ThS or anti-Aβ$_{40}$ immunoreactive Aβ deposition only in APP23 mice (**II**, Fig. 5 and 6). In study **IV**, [^{11}C]PIB binding ratios in FC, NC and HC also showed positive correlation with ThS, anti-Aβ$_{40}$ and anti-Aβ$_{42}$ immunoreactive Aβ load in APP23 mice at 21 months (Pearson's r = 0.71, p = 0.001 (ThS); Pearson's r = 0.88, $p < 0.001$ (Aβ$_{40}$); Pearson's r = 0.59, p = 0.001 (Aβ$_{42}$) (**IV**, Fig. 6). In Tg2576 and APP$_{swe}$-PS1$_{dE9}$ mice, no increase in [^{11}C]PIB binding was detected at older ages when Aβ load in the brain was seen to increase.

[^{11}C]PIB and [^{18}F]flutemetamol FC/CB$_{50\text{-}60}$ –ratios obtained from individual tg mice at the same age are presented in Figure 15 (unpublished data). In general, binding ratios were higher with [^{11}C]PIB than with [^{18}F]flutemetamol.

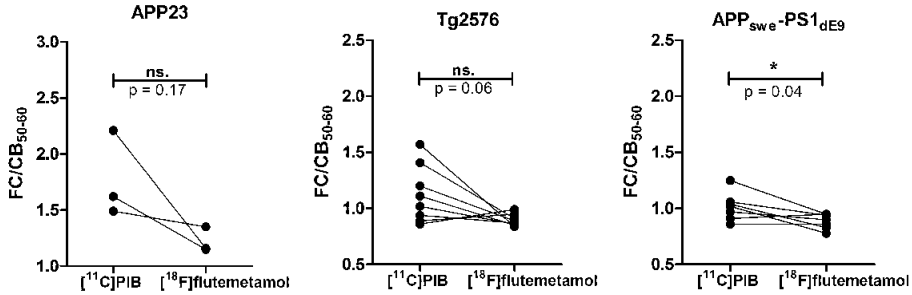

Figure 15. Comparison of [^{11}C]PIB and [^{18}F]flutemetamol binding in individual transgenic APP23, Tg2576 and APP$_{swe}$-PS1$_{dE9}$ mice. FC/CB- ratio was calculated from the last imaging frame (50−60 min post injection). In general, the ratios were higher with [^{11}C]PIB. The differences were evaluated with paired t-test and considered significant if $p < 0.05$.

5.3.2. *Ex vivo binding to Aβ*

In **I**, *ex vivo* autoradiographs from Sprague Dawley rat brain revealed slower clearance of [^{18}F]flutemetamol from all brain regions, especially from white matter structures in comparison to [^{11}C]PIB. The white matter-to-cortex ratio increased from 1.1 (5 min) to 3.7 (30 min) for [^{11}C]PIB and from 0.6 (5 min), to 1.6 (30 min) and further to 11.6 (60 min) for [^{18}F]flutemetamol. At 60 min, ^{11}C-radioactivity in the brain was too low for quantification (**I**, Fig. 1).

In study **II**, [^{11}C]PIB *ex vivo* autoradiographs showed clear tracer binding to Aβ deposits only in cortical sections of APP23 mice. In Tg2576 and APP$_{swe}$-PS1$_{dE9}$ mice, Aβ plaque identification was not possible, and the radioactivity in the reference tissue (CB) exceeded the radioactivity in the FC. High ^{11}C-radioactivity was seen to co-localize with ThS stained fibrillary Aβ deposits in APP23 mice, but less clearly in Tg2576 and APP$_{swe}$-PS1$_{dE9}$ mice (**II**, Fig. 4).

Ex vivo binding of [^{18}F]flutemetamol to Aβ was seen in the brain sections from 27 months old APP23 mice (**III**), and 16 and 22 months old Tg2576 mice (**I**, **III**) using digital autoradiography. In APP$_{swe}$-PS1$_{dE9}$ mice, Aβ deposition was present and visualized with IHC and ThS at 19 months, but *ex vivo* autoradiographs showed less clear binding of [^{18}F]flutemetamol than in the brain of the two other models (**III**, Fig. 5 and Fig. 6). Only APP23 mice were clearly distinguished from wt mice based on FC/CB –ratios calculated from the *ex vivo* autoradiographs (**III**, Fig. 5).

5.3.3. *In vitro binding to Aβ*

In vitro autoradiographs visualized specific [^{18}F]flutemetamol binding to Aβ deposits in the FC of Tg2576 mouse at 16 months (**I**, Fig. 4), and in the cortex of all of the investigated mouse models at 19−22 months (**III**, Fig. 4). High [^{18}F]flutemetamol binding was co-localized with Aβ deposits stained in the same or adjacent cortical brain sections (**III**, Fig. 4).

[^{18}F]flutemetamol binding was completely blocked with co-incubation with 10μM non-radioactive PIB in Tg2576 and APPswe-PS1$_{dE9}$ mice (**I**, **III**), and partially blocked in APP23 mice, presumably due to the much larger amount and higher affinity for the plaques expressed by APP23 mice in comparison to other evaluated models (**III**). Similar displaceable *in vitro* [^{11}C]PIB binding to cortical Aβ deposits was seen in Tg2576 brain in **I**.

5.4. mApoE-PA-LIP treatment

5.4.1. *In vivo follow-up of Aß deposition*

Elevated [^{11}C]PIB binding ratios ($B/F_{40\text{-}60} > 0$) were detected at baseline in most tg APP23 mice, however, large variation among the age-matched APP23 mice was also observed. Mean binding ratios at baseline were higher in mApoE-PA-LIP group in all analyzed regions, reaching statistical significance in the HC (p = 0.02, unpaired t-test). At follow-up 1 after the treatment period, no increase in [^{11}C]PIB binding was seen in the FC of mApoE-PA-LIP group (n = 5), whereas binding increased in the saline group (n = 5) (**IV**, Fig. 2). However, due to the high variation within the groups, this trend was not statistically significant between baseline and follow-up 1 in any of the analyzed brain regions. At follow-up 2, [^{11}C]PIB binding increased significantly from baseline in both mApoE-PA-LIP (n = 4, $p < 0.01$ for all brain regions, hierarchical linear mixed models) and saline groups (n = 5, $p < 0.001$ for all brain regions, hierarchical linear mixed models). [^{11}C]PIB binding ratios for each mApoE-PA-LIP and saline treated mouse during the longitudinal experiment are presented in Figure 16.

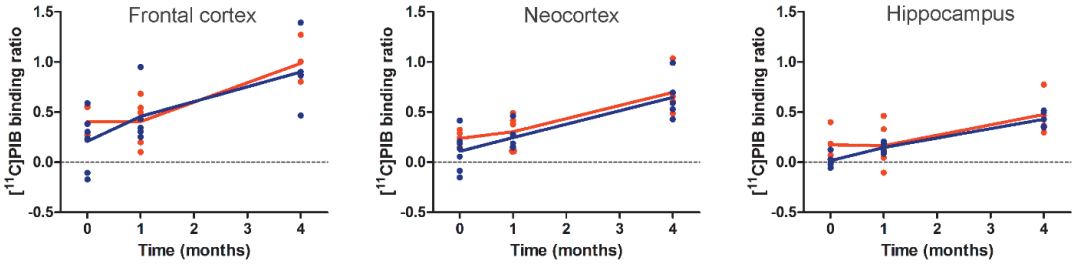

Figure 16. Follow-up of [^{11}C]PIB binding in mApoE-PA-LIP (red) and saline (blue) injected APP23 tg mice. APP23 tg mice were imaged repeatedly at baseline (0 months), after a 3 week treatment period (1 months), and after additional follow-up period (4 months). mApoE-PA-LIP injected mice showed a trend of slower temporal increase in [^{11}C]PIB retention in comparison to saline group, but the difference did not reach statistical significance. The figure is modified from Fig. 2 in **IV**.

5.4.2. *Immunohistochemical and biochemical evaluation of Aß*

mApoE-PA-LIP treated tg APP23 mice did not show any reduction in Aβ deposition or Iba-1 positive activated microglia evaluated with IHC at follow-up 2, when compared to the saline group. The quantified percentages of ThS (**IV**, Fig. 3), anti-$A\beta_{1\text{-}40}$ (**IV**, Fig. 4) and anti-$A\beta_{1\text{-}42}$ (**IV**, Fig. 5) positive amyloid deposits in the FC, NC and HC were equivalent in both groups.

$A\beta_{1\text{-}40}$ or $A\beta_{1\text{-}42}$ concentrations evaluated by ELISA were similar in the forebrain of mApoE-PA-LIP and saline injected mice at follow-up 2. Total insoluble $A\beta_{1\text{-}40}$ and $A\beta_{1\text{-}42}$ concentrations were 27.6 ± 6.0 and 5.6 ± 0.4 nmol/g in the mApoE-PA-LIP group (n = 4) and 26.4/23.5 and 4.8/5.4 nmol/g in saline-treated mice (n = 2). The amount of soluble $A\beta_{1\text{-}40}$ and $A\beta_{1\text{-}42}$ was 2.3 ± 1.0 and 0.4 ± 0.3 pmol/g in the mApoE-PA-LIP group and 2.4/2.0 and 0.2/0.3 pmol/g in the saline group.

6. DISCUSSION

6.1. Used AD mouse models

At the time this work was initiated, *in vivo* PET imaging of Aβ had been performed only in APP23 (Maeda et al., 2007), Tg2576 (Toyama et al., 2005) and PS1/APP mice (Klunk et al., 2005). The results from these studies were conflicting and difficult to compare due to several methodological issues, thus it was deemed reasonable to investigate both [^{11}C]PIB and the novel tracer [^{18}F]flutemetamol using more than one mouse model. All of the chosen mouse models, i.e. APP23, Tg2576 and APP$_{swe}$-PS1$_{dE9}$, have been well characterized and widely used already prior to this project and as expected, a clear difference in the structure, quantity and temporal appearance of Aβ deposits was detected between these models also in this thesis work.

In APP23, the onset of deposition was slow, but abundant large and compact deposits with clear binding of ThS, [^{11}C]PIB and [^{18}F]flutemetamol, were present throughout the brain in old animals, in line with other reports (Maeda et al., 2007; Maier et al., 2014; Sturchler-Pierrat and Staufenbiel, 2000). In the Tg2576 model, we observed very late onset and a slow progression of Aβ deposition. The Tg2576 model was previously reported to show evidence of Aβ deposition in the brain at 9−12 months (Hsiao et al., 1996; Kawarabayashi et al., 2001), whereas in **I−III**, the first sparse deposits were seen only at 15 months, and the plaque load was modest even at 22 mo. Although the observed slow Aβ deposition is temporally closer to human AD, the Tg2576 model seems less attractive for longitudinal imaging studies, as in our experience, follow-up and repeated anesthesia for animals older than 22 months is already challenging. In addition, also cerebellar deposition has been reported for this strain (Hsiao et al., 1996), further complicating the choice of reference region, even though it was not detected in **I−III**. In APP$_{swe}$-PS1$_{dE9}$ mice, abundant deposition was visible already at 9 months and the plaque load in FC was extensive in old mice. In addition, due to favored production of Aβ$_{42}$ over Aβ$_{40}$ and the less congophilic nature of the deposits in this model, the quantification conducted in **II−III** using anti-Aβ$_{40}$ antibody and ThS is likely to be an underestimate. In contrast to earlier reports (Garcia-Alloza et al., 2006; Jankowsky et al., 2004), we observed abundant deposition also in CB at 19 mo. Similar findings have been subsequently reported by Brendel and colleagues (Brendel et al., 2015a), leading to the conclusion that this model is not preferred for quantitative *in vivo* PET imaging when a cerebellar reference is used.

When relevance to human AD is considered, all of the existing tg models fail to exhibit all of the characteristics of human AD, e.g. robust NFT formation and neuronal loss. Nonetheless, the current models represent a valuable research tool for studying APP metabolism and Aβ deposition *in vivo.* However, development of translationally more relevant models, that would present progressive and temporally parallel neuropathological features of human AD, impairment in learning and memory, in addition to CSF biomarkers and neuroimaging data which would correlate with human AD, has still been emphasized (Keene et al., 2016). For the mApoE-PA-LIP treatment study presented in this thesis, we chose the APP23 model, because **I, II** and several other reports (Maeda et al., 2007; Maier et al., 2015; Maier et al., 2014) supported its use over other models in small animal [^{11}C]PIB PET imaging studies. Even though NFT are not present in this model, its suitability for anti-amyloid intervention studies is further supported by its progressive Aβ pathology and the presence of

hyperphosphorylated tau, progressive impairment in spatial memory (Van Dam et al., 2003), and changes in CSF-Aβ and CSF-tau, mimicking the changes seen in AD patients (Maia et al., 2013).

6.2. Methodological considerations

μPET imaging systems available to date have a spatial resolution of approximately ~1.5 mm whereas ~2.5 mm is typical for dedicated human brain scanner. The recent combined preclinical PET/MRI equipment with digital detector technology has reached a spatial resolution of 0.7 mm (Weissler et al., 2015), however, physical properties of PET radionuclides, i.e. the positron range and photon non-collinearity, limit further improvements in resolution. Imaging targets approaching the spatial resolution of the scanner, such as different mouse brain regions, result inevitably in a partial volume effect (PVE) that leads to underestimation of quantified values and a decrease in sensitivity. Consequently, lower binding ratios from *in vivo* data in comparison to subsequent *ex vivo* autoradiographs were seen for [^{18}F]flutemetamol in **III**, similar to the situation with [^{18}F]florbetaben (Rominger et al., 2013) and [^{18}F]florbetapir (Poisnel et al., 2012). The effect of applied PVE correction (PVEC) has recently been investigated also for mouse amyloid imaging: For [^{18}F]florbetaben, a clear effect was observed: In APPswe mice at 20 months, standardized uptake value ratio (SUVr) increased 36.4% from baseline with PVEC, in comparison to 15.5% without PVEC (Brendel et al., 2014). In addition, PVEC was seen to steepen the estimated slope for temporal Aβ deposition, and thus increase the difference in [^{18}F]florbetaben binding between young and old animals (Brendel et al., 2015a). In **II**−**IV**, PVEC would have presumably increased the sensitivity of the tracers to detect Aβ deposition at earlier ages, and for revealing mApoE-PA-LIP treatment effects. The application of PVEC in all future small animal brain imaging studies is thus highly recommended.

Another source of error for small animal imaging data is the spillover from adjacent structures with high radioactivity uptake, i.e. the skull or white matter for [^{18}F]flutemetamol, potentially leading to an overestimation of the signal in cerebral VOIs. In this thesis, spillover from the skull was expected to be similar in all cortical and cerebellar VOIs, thus it is likely to be negated in the calculated ratios. In addition, possible spillover to frontal VOIs from adjacent high uptake in the nasal cavity can be anticipated to cause a similar error in both tg and wt mice, thus leading to an equivalent overestimation in both groups. In an attempt to avoid this problem, in all analyses, the drawing of cerebral VOIs was guided by the CT/MRI template rather than the radioactivity. These issues, however, are important in small animal imaging with small analyzed VOIs, and they should be carefully considered while planning the quantification of the PET data.

The Multimodal Inveon PET/CT scanner was used in **I**−**IV**, where the CT scan provides anatomical information and enables attenuation correction for the PET data. However, the CT contrast is not sufficient for soft tissue separation, hence the drawing of cerebral VOIs was guided either by the skull and additional brain atlas (**I**−**III**), or by an additional MRI template superimposed onto the PET data (**IV**). With PET/MRI imaging systems, MR images from each individual mice would allow for more accurate analysis, and in addition, simultaneous assessment of other physiological features, e.g. alterations in regional cerebral blood flow (Maier et al., 2015), using the MR entity. Due to the previously discussed issues concerning spatial resolution and PVE, it is also noteworthy that it is impossible to follow the dynamics or morphology of individual plaques with μPET. For these purposes, real-time multiphoton microscopy or high field microscopic MRI could be exploited

(Hefendehl et al., 2011; Maier et al., 2015). However, due to the invasive nature of the installation of a cranial window and the limited imaging depth (< 1mm), multiphoton microscopy is not suitable for quantifying Aβ levels in whole brain. On the contrary, high resolution MRI enables full 3D volume quantification of individual plaques with significantly reduced work load compared to histological evaluation, and could potentially be used also *in vivo,* however, its sole usage for amyloid imaging is limited by its low specificity to Aβ (Maier et al., 2015).

In addition to μPET, also a μSPECT system could be used for Aβ imaging in tg AD models. While current multi-pinhole μSPECT systems offer better spatial resolution in comparison to μPET, and also increased sensitivity in comparison to clinical SPECT systems, their usage for amyloid imaging has been hampered by the poor availability of high quality SPECT tracers for Aβ, as well as quantification issues related to the decay properties of SPECT radioisotopes. Recently, a novel SPECT tracer for Aβ imaging was shown to detect Aβ deposition in old Tg2576 mice in a quantitative manner (Chen et al., 2015). However, in the longitudinal follow-up studies, quantification issues and the ten times higher injected activities combined with the longer half-life of ^{125}I still lessen its potential.

Various quantification methods for PET data have been used in different small animal amyloid imaging studies, e.g. SUVr or VOI ratios for static time frames, Logan DVRs or BP_{ND}s for dynamic data or direct comparison of %ID/g values. Ratios calculated for certain static time frame have been seen to correlate well with DVRs, thus justifying also shorter static scans and simple reference region ratio quantification (Brendel et al., 2015a; Rominger et al., 2013). In most of the studies, a reference region approach is employed, with the cerebellar reference being most often used. This approach is widely used also in clinical studies; however, as discussed before, its use is not optimal in mice, especially with tracers with elevated white matter binding characteristics as it is not possible to define VOIs only to cerebellar grey matter. In study **III**, the uptake was higher in the CB reference VOI than in cortical VOIs, resulting in binding ratios below unity in wt and young tg mice. Similar results have been reported for [^{18}F]florbetaben (Brendel et al., 2015a; Rominger et al., 2013). In addition, many of the used AD models e.g. APP_{swe}-$PS1_{dE9}$, APPPS1-21, Tg2576 and BRI1-42 express Aβ deposits also in the CB. In APPPS1-21 mice, significantly higher binding to CB was seen in tg vs wt mice using [^{11}C]PIB (Waldron et al., 2015). Both the possible specific binding to cerebellar Aβ, and non-specific binding to cerebellar white matter reduce the sensitivity of tracers, especially for the initial early phases when there is much less apparent cortical Aβ pathology. Utilizing animal models not expressing any cerebellar Aβ, tracers with low white matter binding, and PVEC would be required for optimal sensitivity in small animal imaging studies.

6.3. Utility of [^{11}C]PIB and [^{18}F]flutemetamol for μPET imaging

For practical work, [^{18}F]flutemetamol offers many benefits over [^{11}C]PIB also in preclinical imaging: The longer half-life of ^{18}F in comparison to ^{11}C allows for more efficient use of the tracer batches, and gives more time for the practical laboratory work. In addition, in general, its high SA is beneficial for CNS imaging. However, a comparison of the tracers revealed also less desirable characteristics of [^{18}F]flutemetamol for small animal imaging.

Pharmacokinetic properties

Both [^{11}C]PIB and [^{18}F]flutemetamol displayed suitable pharmacokinetic properties for preclinical imaging; both entered the brain rapidly, however, clearance of [^{18}F]flutemetamol from the brain was slower. Similar slower washout from the brain has also been reported in clinical studies, where [^{18}F]flutemetamol binding ratios in the brain were maximal only at 80 min after injection (Nelissen et al., 2009). The peripheral distribution of [^{11}C]PIB and [^{18}F]flutemetamol in rats and mice was comparable with both tracers being excreted via the hepatobiliary route, similarly to the situation in humans (Koole et al., 2009; Scheinin et al., 2007). The subtle differences in the distribution of the tracers are presumably caused by the higher lipophilicity of [^{18}F]flutemetamol ($LogP_{C18}$ = 1.7) over [^{11}C]PIB ($LogP_{C18}$ = 1.2) (Mathis et al., 2007).

^{18}F-radioactivity measured from cranial bone in rats was stable over time and low at 60 min p.i., leading to the conclusion that [^{18}F]flutemetamol is not de-fluorinated *in vivo*. However, subsequent *ex vivo* experiments revealed a different de-fluorination pattern in mice: ^{18}F-radioactivity in the skull was significantly higher in mice than in rats at 60 min p.i., exceeding the radioactivity measured from the neighboring brain tissue. Higher uptake was not visually detected *in vivo,* but it might have resulted in an overestimation of the binding ratios from the cortical VOIs in all of the studied mice. A similar high uptake in the skull has been observed in mice also with [^{18}F]florbetaben (Waldron et al., 2015).

Both tracers were also rapidly metabolized into several more polar radioactive metabolites which could be detected in rat plasma; an equivalent high metabolism rate has been reported for both tracers in humans (Heurling et al., 2016; Klunk et al., 2004), and for [^{11}C]PIB in mice (Mathis et al., 2003) and baboons (Parsey et al., 2005). Rapid peripheral metabolism has been characterized also for [^{18}F]FDDNP, [^{18}F]florbetapir and [^{18}F]florbetaben (Choi et al., 2009; Luurtsema et al., 2008). One ([^{11}C]PIB) and two ([^{18}F]flutemetamol) radioactive metabolites were also detected from rat brain homogenates in **I**. The metabolites were not further characterized, but one was assumed to be 6-sulphato-PIB produced by estrogen sulfotransferase present in rat brain (Cole et al., 2010; Mathis et al., 2004). Since [^{18}F]flutemetamol is a structural analogue of PIB, equivalent sulfation of by the same enzyme could be expected. In addition, in agreement with the previous data (Mathis et al., 2004), no radioactive metabolites were detected in mouse brain in **I.** The reported metabolic differences between species need to be considered when performing imaging experiments with different tg AD rat models. The presence of radioactive metabolites in the brain would decrease the sensitivity of the tracer and further complicate the data quantification.

The obtained effective dose estimates for [^{11}C]PIB and [^{18}F]flutemetamol extrapolated from rat *ex vivo* data were 2.28 and 6.65 µSv/MBq, respectively. Higher estimates have been previously published for both [^{11}C]PIB (6.50 µSv/MBq (Parsey et al., 2005); 4.74 or 5.29 µSv/MBq (O'Keefe et al., 2009; Scheinin et al., 2007)) and for [^{18}F]flutemetamol (33.8 µSv/MBq (Koole et al., 2009)). As the previous estimates were obtained from baboon and human data without extrapolation, differences with the values obtained in **I** are not surprising.

Specific activity

The importance of high SA for amyloid imaging in tg models was originally proposed by Maeda and co-workers after the first successful amyloid PET study in mice was done using high SA [^{11}C]PIB (290 GBq/µmol, end of synthesis) (Maeda et al., 2007). Due to this finding, [^{18}F]flutemetamol

produced with very high SA (>1 TBq/µmol, end of synthesis) was predicted to show improved sensitivity in **III** for *in vivo* imaging of Aβ in "low target" models, i.e. Tg2576 and APP_{swe}-$PS1_{dE9}$, where deposition could not be followed in **II** with [^{11}C]PIB with a lower SA. On the contrary, despite its very high SA, [^{18}F]flutemetamol did not show superior sensitivity for detecting changes in Aβ deposition over [^{11}C]PIB. In addition, in other studies with [^{18}F[florbetaben and [^{18}F]florbetapir, successful longitudinal imaging results were obtained with a SA of 80 GBq/µmol (Rominger et al., 2013), 150 GBq/µmol (Poisnel et al., 2012) and 35 GBq/µmol (Sérrière et al., 2015), all of which are much lower than the value of the [^{18}F]flutemetamol in study **III**. Together these findings suggest that even though a high SA value in general is a desired feature in CNS imaging, it is not the key factor when performing PET studies with tg models.

White matter binding

High binding to cerebral white matter is a common feature for Aβ targeting PET tracers, and it is generally more prominent with ^{18}F-labelled tracers. Higher white matter binding of [^{18}F]flutemetamol over [^{11}C]PIB has been reported in clinical studies (Landau et al., 2013; Vandenberghe et al., 2010), and a similar difference was clearly visible in rats (**I**) and mice (**II−III**). This binding is often stated to be unspecific; however, the mechanism of white matter binding has not been investigated in detail. In addition to the expected non-specific binding due to the tracer's higher lipophilicity, it might include also specific components, such as specific binding to myelin (Stankoff et al., 2011).

The CB contains large amounts of white matter that cannot be separated from the grey matter areas in small animal PET/CT. Consequently, even though clear specific binding of [^{18}F]flutemetamol to cortical Aβ deposits was present in mouse brain sections in **I** and **III**, higher white matter binding inevitably lowered the sensitivity of the tracer in comparison to [^{11}C]PIB when the cerebellar reference region was used. An equivalent decrease in the signal-to-background ratio in comparison to [^{3}H]PIB and [^{3}H]AZD4694 has been previously reported for [^{3}H]flutemetamol (Juréus et al., 2010). In clinical studies, a late scanning window (e.g. 85−110 min after injection) has been used to ensure more efficient washout of non-specific binding of the ^{18}F-tracers from the brain (Vandenberghe et al., 2010; Villemagne et al., 2012). Accordingly, the last imaging frame representing the late washout phase at 50−60 min was used for quantitation of [^{18}F]flutemetamol data in study **III**. An even later time frame could further increase the binding ratios, however, as **III** was the first *in vivo* imaging study using [^{18}F]flutemetamol in mice, dynamic scans were preferred over static scans for quantification purposes. In addition, dynamic scans longer than 60 minutes were not considered appropriate because these experiments involved aged and fragile tg animals. In future studies, static scans starting only at 90 min p.i. could be performed, however, as discussed before, de-fluorination of [^{18}F]flutemetamol in mice and the resulting increase in the accumulation of ^{18}F-fluorine in the skull, could complicate the *in vivo* analysis at later time points.

6.4. µPET imaging of Aβ deposition in AD mouse models

Recently, an increasing number of µPET imaging studies have been completed using different Aβ targeting PET tracers and transgenic animal models (Table 10). PIB, florbetapir and florbetaben have previously been shown to have multiple binding sites in human AD brain and bind mainly to a shared high affinity binding site (Ni et al., 2013), hence their binding characteristics can be assumed to be similar also in tg mouse models. However, it is impossible to directly compare the obtained results from these studies due to differences in instrumentation, quantification methods, animal models and

evaluated time-points. In general, all of these *in vivo* studies support the findings of this thesis, i.e. the importance of the used animal model, and the quantity and quality of its Aβ deposits for successful follow-up by μPET.

[^{11}C]PIB has already been exploited in multiple imaging studies with various mouse models. A gradual increase in [^{11}C]PIB binding was seen in aging APP23 but not in Tg2576 or APP$_{swe}$-PS1$_{dE9}$ mice in **II**. These results are in line with earlier studies where Toyama and co-workers showed only mildly increased binding ratios in Tg2576 in comparison to wt mice, and Klunk and co-workers failed to detect any significant increase in [^{11}C]PIB binding even in old PS1/APP mice (Klunk et al., 2005; Toyama et al., 2005). At that time, the authors concluded that the low number of high-affinity PIB binding sites or lower affinity hampered the usability of this method in mice. In a subsequent study, increased [^{11}C]PIB binding was successfully detected in aged APP23 mice, and recently also in very old (28 months) Tg2576 mice, when tracers were produced with higher SA (Chen et al., 2015; Maeda et al., 2007). However, increased [^{11}C]PIB binding was replicated with lower SA in APP23 mice (**II**), whereas in Tg2576 mice, specific binding was not detected even with [^{18}F]flutemetamol (**III**), that was produced with more than three times higher SA than that reported for [^{11}C]PIB (Chen et al., 2015). Together, these studies suggest that the controversies are due to differences in study design rather than SA.

In addition to the aforementioned studies, successful longitudinal *in vivo* [^{11}C]PIB imaging of Aβ has been reported for APP23 (Maier et al., 2015; Maier et al., 2014), APPPS1-21 (Maier et al., 2014), and ARTE10 models (Manook et al., 2012). In addition, cross-sectional evaluations with clear differentiation of wt and tg mice have been conducted with the use of 5XFAD (Rojas et al., 2013), APPPS1-21 (Waldron et al., 2015), and ARTE10 mice (von Reutern et al., 2013). In these models, the specificity of [^{11}C]PIB binding has been verified with Aβ immunohistology, and an increase in Aβ deposition was shown to correlate with the temporal increase in [^{11}C]PIB binding (Maier et al., 2014; Manook et al., 2012; von Reutern et al., 2013). In addition, negative [^{11}C]PIB binding was recently reported in the BRI1-42 model (Waldron et al., 2015).

As far as we are aware, **I** and **III** remain the only studies where [^{18}F]flutemetamol has been evaluated in tg mouse models of AD. Similar to [^{11}C]PIB, a temporal increase in [^{18}F]flutemetamol retention was detected only in aging APP23 mice, and the expected increase in sensitivity due to the very high SA of [^{18}F]flutemetamol was not observed. To date, increasing numbers of preclinical studies have been published with other ^{18}F-tracers: With [^{18}F]florbetaben, cerebral Aβ deposition has been longitudinally followed in APPswe (Brendel et al., 2015a; Rominger et al., 2013), and subsequently in a cross-sectional comparison using also PS2APP and G384A mice (Brendel et al., 2015a). Similar to [^{18}F]flutemetamol in **III**, no evidence of increased binding was detected in aging APP$_{swe}$-PS1$_{dE9}$; instead SUVr decreased with time, possibly due to the Aβ deposition observed also in the CB reference region (Brendel et al., 2015a). When [^{18}F]florbetaben was directly compared with [^{11}C]PIB, it seemed to exhibit a lower discriminating power for tg and wt mice, the differences between groups were approximately half of those achieved with [^{11}C]PIB (Waldron et al., 2015). In this thesis, similar differences were observed between [^{18}F]flutemetamol and [^{11}C]PIB, presumably reflecting the effect of the higher non-specific binding of ^{18}F-labeled tracers in the reference region used, lowering the sensitivity as discussed before. To gain optimal quantification using these tracers, modelling the data through an image derived input function could be one alternative. Alternatively, another reference

Table 10. Summary of the μPET imaging studies performed to date with use of different transgenic mouse models and Aβ targeting PET tracers. **X** = Aβ deposition has been observed with use of μPET imaging; **O** = Increased Aβ deposition was not observed with the use of μPET imaging. The age of the animals when increases in tracer binding were first detected or could not be detected are presented in parenthesis after the symbols.

	[^{11}C]PIB	[^{18}F]florbetaben	[^{18}F]florbetapir	[^{18}F]flutemetamol	[^{18}F]FDDNP	References
APP23	**X** (15−17 mo)[1,2,3,4]	-	-	**X** (15 mo)[5]	-	[1]Maeda et al., 2007; [2]**II**; [3]Maier et al., 2014; [4]**IV**; [5]**III**
Tg2576	**X** (28 mo)[4], **O** (22mo)[1,2]	-	-	**O** (22 mo)[3]	**O** (13−15 mo)[5]	[1]Toyama et al., 2005; [2]**II**; [3]**III**; [4]Chen et al., 2016; [5]Kuntner et al., 2009
APP$_{swe}$-PS1$_{dE9}$	**O** (19 mo)[2]	**O** (24 mo)[4]	**X** (9 mo)[1]	**O** (19 mo)[3]	-	[1]Serriere et al., 2012; [2]**II**; [3]**III**; [4]Brendel et al 2015,
PS1/APP (Tg2576xM146L PS1)	**O** (12 mo)	-	-	-	-	Klunk et al., 2005
APPswe	-	**X** (20 mo)[1,2]	-	-	-	[1]Rominger et al., 2012; [2]Brendel et al., 2015
PS2APP	-	**X** (8−10 mo)[1,2]	-	-	-	[1]Brendel et al., 2015; [2]Brendel et al., 2017
G384A (APP23xPS45)	-	**X** (16 mo)	-	-	-	Brendel et al., 2015
BRI1-42	**O** (22−25 mo)	**O** (22−25 mo)	-	-	-	Waldron et al., 2015
APPPS1-21	**X** (8 mo[2], 22−25 mo[1])	-	**X** (5 mo)[3]	-	-	[1]Poisnel et al., 2012; [2]Maier et al., 2014; [3]Waldron et al., 2015
Arte-10	**X** (9 mo, tg-tg[1]; 23−25 mo, tg[1,2])	-	-	-	-	[1]Manook et al., 2012; [2]von Reutern et al., 2013
5xFAD	**X** (10 mo)	-	**X** (11 mo)	-	-	Rojas et al., 2013

region without Aβ deposition and with constant activity could be used. Different reference regions and methods for intensity scaling for [^{18}F]florbetaben small animal amyloid imaging studies were investigated in a recent study by Overhoff and colleagues (Overhoff et al., 2016). In that study, a white matter reference region was found to be slightly superior to a CB reference, and due to this finding, the normalization in a subsequent [^{18}F]florbetaben study was performed using the white matter reference (Brendel et al., 2016b). Similar approach could be applied also for [^{18}F]flutemetamol studies.

In addition to [^{18}F]flutemetamol and [^{18}F]florbetaben, also [^{18}F]florbetapir has been successfully used to image Aβ in mouse brain (Poisnel et al., 2012; Sérrière et al., 2015). Interestingly, contradictory results to those obtained with [^{18}F]flutemetamol (**III**) and [^{18}F]florbetaben (Brendel et al., 2015a) were reported using the APP_{swe}-$PS1_{dE9}$ model (Sérrière et al., 2015): A significant difference in cortical SUVr was seen between APP_{swe}-$PS1_{dE9}$ and wt mice at 19 months, even though the CB reference was used, and Aβ deposition in the reference region was reported similar to **III**. This finding suggests that [^{18}F]florbetapir may possess superior sensitivity over [^{18}F]florbetaben and [^{18}F]flutemetamol in APP_{swe}-$PS1_{dE9}$ model, however, the differences with wt mice were relatively small even at 19 months of age when abundant deposition is already present in the brain. In addition, PVEC was used for the PET data, which could explain higher sensitivity in comparison to [^{18}F]flutemetamol in **III**.

Selection of suitable AD mouse model

The characteristics of the various transgenic mouse models used in amyloid μPET imaging experiments to date are summarized in Table 11. Together these data shows that although there is no unambiguous way of predicting whether or not a mouse model will be suitable for amyloid μPET imaging, a few characteristics seem to be important for *in vivo* detection of β-amyloidosis in mice.

The level of $Aβ_{40}$ in relation to $Aβ_{42}$ does not seem to unequivocally explain the differences in tracer binding between models: In models that have revealed the highest binding ratios and differences to wt animals, i.e. APP23, ARTE10 and PS2APP mice, $Aβ_{40}$ dominates in the first two, whereas in ARTE10 mice, $Aβ_{42}$ predominates by 1.5 fold (Richards et al., 2003; Sturchler-Pierrat et al., 1997; Willuweit et al., 2009). In addition, increased [^{11}C]PIB binding has also been detected in 5xFAD mice that express $Aβ_{42}$ almost exclusively (Rojas et al., 2013), whereas no specific [^{11}C]PIB binding was detected in PS1/APP mice with a $Aβ_{40}$ dominance (Takeuchi et al., 2000). [^{11}C]PIB binding to synthetic $Aβ_{40}$ and $Aβ_{42}$ has also been reported to be similar, further supporting the matter (Klunk et al., 2005). In addition, in human AD, [^{11}C]PIB is seen to bind both $Aβ_{40}$ and $Aβ_{42}$ immunoreactive plaques, with most robust labeling in compact deposits (Ikonomovic et al., 2008).

In this thesis, binding of [^{11}C]PIB and [^{18}F]flutemetamol to Aβ deposits in APP23 model was clearly superior to the other two investigated models, and consequently the APP23 model was selected for the subsequent intervention study. The superiority of the APP23 mouse model for [^{11}C]PIB binding has also been shown in comparison to the APPPS1-21 model (Maier et al., 2014), where the maximum BP_{nd} was more than five times higher with APP23 with a comparable range of histological Aβ deposition between models. The authors stated that the distinguishing feature between the models was the *plaque size;* this differed by a factor of approximately eight (5−25 μm in APPPS1-21 vs. 25−200 μm in APP23). In addition, the deposits in APP23 brain were more often seen as plaque clusters in contrast to the more homogeneously distributed deposits in APPPS1-21 brain (Maier et al., 2014). In addition, Manook and co-workers detected a more intense [^{11}C]PIB signal in thalamus

in comparison to cortical areas of ARTE10 mice, where thalamic plaques had previously been shown to be larger (Willuweit et al., 2009). As shown in Figure 12, a similar relationship between [^{11}C]PIB and [^{18}F]flutemetamol binding, Aβ plaque size and distribution was observed in this thesis; maximum size of plaques visualized by anti-Aβ$_{40}$ staining was approximately 250 µm in APP23, 120 µm in Tg2576 and 50 µm in APP$_{swe}$-PS1$_{dE9}$, and more clusters were visible in the APP23 brain. As suggested by Maier and co-workers, the clustering of large deposits in APP23 could lead to an increased amount of high affinity binding sites and signal for an equivalent plaque load, whereas smaller and evenly distributed deposits in APPPS1-21, Tg2576 and APP$_{swe}$-PS1$_{dE9}$ models present less binding sites and are more affected by PVE.

N-terminal modifications of Aβ are typical in human AD (Kawarabayashi et al., 2001) and these N-terminally truncated forms of Aβ have been suggested to be critical also for [^{11}C]PIB binding in mice (Maeda et al., 2007). However, a relatively high Aβ load is still needed for *in vivo* detection of the deposition in mouse models that express these kinds of N-terminal modifications, e.g. in APP23 mice, increased tracer binding was detected only at 15−17 months (Maeda et al., 2007; Maier et al., 2014). In addition, Tg2576 and BRI-1-42 models, which also express N-terminal truncated forms of Aβ, have not been found suitable for amyloid imaging µPET experiments, or at least only when the animals reach a very old age.

Considering the major differences between the quality and quantity of Aβ deposits in different tg AD models, it is not surprising that there are differences in amyloid µPET experiments between different animal models of AD. Based on this thesis as well as the aforementioned imaging studies, it is possible to conclude that generally a *high plaque load*, as well as *large plaque size* and *compact morphology* seem to be the key factors for detecting mouse Aβ using PET imaging. Accordingly, a high cortical amyloid load (> 4%) detected by ThS or other dyes that label dense core amyloid deposits, and a large size of the deposits seem to have the highest predictive value. On the other hand, the SA of the used PET tracer seems to be less important than previously claimed.

Limitations of the method

In all of the aforementioned studies where Aβ deposition was successfully measured or followed in tg mouse models, increased tracer binding has been detected only in older tg mice, regardless of the age of onset for Aβ deposition (Table 11). These limitations in sensitivity inevitably narrow the usability of the µPET method for therapeutic study design, where an anti-amyloid treatment is expected to halt or reverse already existing amyloid deposition in the brain. As such, the method seems to be inappropriate for detecting early changes in Aβ deposition and anti-amyloid effects in prevention studies that could be more clinically valid considering the mechanism of action of many anti-amyloid compounds. In addition, in some models, the differences between old tg mice and wt or younger tg animals were still quite small, leading to rather low margins for detection of possible treatment effects.

.

Table 11. Characteristics of the different transgenic mouse models used for amyloid μPET imaging. $A\beta_{N3pE}$ = N-terminally truncated and pyroglutamated form of Aβ; APP = amyloid precursor protein; CAA = cerebral amyloid angiopathy; CB = cerebellum; Flo = Florida mutation; hu = human; Lon = London mutation; Swe = Swedish mutation.

Mouse model	Included mutations	$A\beta_{42}/A\beta_{40}$ levels	Aβ deposition	Plaque morphology	Approximate plaque size	CAA	CB deposits	$A\beta_{N3pE}$	References
APP23	$huAPP751_{Swe}$	$A\beta_{40}$ dominates[1]	6 mo[1]	Dense cored, diffuse deposition appear later[1]	< 200 μm²	X	O	X	[1]Sturchler-Pierrat et al., 1997; [2]Maier et al., 2014
Tg2576	$huAPP695_{Swe}$	$A\beta_{40}$ dominates[1,2]	11−13 mo[1]	Dense cored and diffuse[1]	< 120 μm³	X	X	X	[1]Hsiao et al., 1996; [2]Kawarabayashi et al., 2001; [3]**II**
APPswe-PS1dE9	$hu/moAPP_{Swe}$, $PSEN1_{\Delta E9}$	$A\beta_{42}$ dominates[1,2]	4 mo	Dense cored and diffuse[1,2]	< 50 μm³	X	X	o	[1]Jankowsky et al., 2004; [2]Garcia-alloza et al., 2006; [3]**II**
PS1/APP	$huAPP695_{Swe}$, $PSEN1_{M146L}$	$A\beta_{40}$ dominates	3 mo	Compact and diffuse	< 70 μm	?	O	?	Takeuchi et al., 2000
APPswe	$huAPP751_{Swe}$	$A\beta_{40}$ dominates 5−10 fold[1]	12 mo	Dense cored and congophilic	< 245 μm²	O	O	O	[1]Richards et al., 2003; [2]Brendel et al., 2015
PS2APP	$huAPP751_{Swe}$, $huPSEN2_{N141I}$	$A\beta_{40}$ dominates 3−4 fold[1]	6 mo	Mainly compact[2], but also diffuse[1]	< 100 μm²	O	O	?	[1]Richards et al., 2003; [2]Brendel et al., 2015
G384A	$huAPP751_{Swe}$, $PSEN1_{G384A}$	$A\beta_{40}$ dominates slightly (less than in APP23)[1]	2 mo	Dense cored and congophilic[1]	< 100 μm²	?	X	?	[1]Busche et al., 2008; [2]Brendel et al., 2015
BRI1-42	BRI-$A\beta_{42}$ fusion	Exclusive $A\beta_{42}$[1]	3 mo (CB), 6 mo[1]	Dense cored and diffuse[1], predominantly diffuse in forebrain[2]	< 55 μm[1]	X	X	X	[1]McGowan et al., 2005; [2]Waldron et al., 2015
APPPS1-21	$huAPP_{Swe}$, $PSEN1_{L116P}$	$A\beta_{42}$ dominates 5-fold[1]	6−8 wk	Dense cored and congophilic, halo of diffuse amyloid appears later[1]	< 25 μm[4]	X	O	?	[1]Radde et al., 2006; [2]Maier et al., 2014
Arte-10	$huAPP_{Swe}$, $PSEN1_{M146V}$	$A\beta_{42}$ dominates 1.5-fold[1]	3 mo (tg-tg) 5mo (tg)	Dense cored congophilic, diffuse deposits later	< 100 μm, most < 40 μm²	X	O	?	[1]Willuweit et al., 2009; [2]Manook et al., 2012
5xFAD	$APP695_{Swe, Flo, Lon}$, $PSEN1_{M146L, L286V}$	Almost exclusively $A\beta_{42}$	2 mo	Both mature and diffuse	~20 μm	?	O	?	Oakley et al., 2006

6.5. Evaluation of anti-amyloid drugs with μPET imaging

Functionalized mApoE-PA-LIPs have recently been investigated as a novel therapeutic approach for targeting Aβ in AD (Balducci et al., 2014; Mancini et al., 2016), and longitudinal [^{11}C]PIB PET was used in **IV** for following the therapeutic effects of mApoE-PA-LIPs in APP23 mice. Even though several studies have reported the possibility to monitor the increasing Aβ load in tg models, very few *in vivo* evaluations of anti-amyloid compounds have actually been published. In an early study, where intra-hippocampal injections of anti-Aβ antibody 6E10 were given to APP23 mice, reduced [^{11}C]PIB binding potential and a histologically-confirmed Aβ load were detected (Maeda et al., 2007). Similar results were subsequently obtained using [^{18}F]FDDNP and intra-cerebral injection of 6E10 in triple-tg AD rats (Teng et al., 2011). These studies supported the use of a longitudinal PET imaging method for evaluating anti-amyloid interventions, however novel drug candidates were not investigated. As far as is known, with the exception of mApoE-PA-LIPs reported in this thesis, the only longitudinal anti-amyloid treatment follow-up using μPET has been published by Brendel and colleagues, who observed inhibition of Aβ plaque formation in APPswe mice during treatment with a novel gamma-secretase inhibitor RO5506284, and detected the effect using longitudinal *in vivo* [^{18}F]florbetaben PET imaging (Brendel et al., 2015b). In that study, high [^{18}F]florbetaben binding at baseline was also seen to correlate with further increases in binding ratios despite the anti-amyloid treatment, further emphasizing the effect of individual variations in the baseline on the outcomes. Similar high variation at baseline was present also in APP23 mice at 16−17 months in **IV**. Both these studies clearly highlight the clear advantages of non-invasive longitudinal follow-up with PET in treatment monitoring: As temporal differences can be evaluated in individual mice, the error resulting from inter-individual variation at baseline can be avoided, leading to increased sensitivity to the treatment response and a reduction in the animal numbers needed for meaningful results. In addition, baseline data could be exploited for stratification of the animals to intervention and control groups based on their estimated levels of Aβ pathology.

Previously, a reduction of approximately 34% in total insoluble Aβ was detected after mApoE-PA-LIP treatment in APP_{swe}-$PS1_{dE9}$ mice (Balducci et al., 2014), however, such decrease was not observed in the mApoE-PA-LIP group at follow-up 2 in **IV**. This discrepancy can be attributed to the clear differences in the study design between these two studies; in **IV**, an additional follow up of three months was added to the study protocol, as μPET enables monitoring of possible long term effects in the same individual mice. Thus, the histological plaque load was not quantified directly after the treatment, as was done in the study by Balducci and colleagues. In addition, conflicting results are not surprising due to the previously discussed differences in Aβ load and type between these two tg models. As none of the existing tg models fully mirror human AD, it is beneficial to test novel interventions in multiple preclinical models; if clinical success is to be expected, the intervention should be able show effects also in mouse models with different temporal courses and types of Aβ deposits.

Interestingly, these two studies had different outcomes also in the [^{11}C]PIB PET experiments: In the study conducted by Balducci and colleagues, [^{11}C]PIB binding in mApoE-PA-LIP treated APP23 brain was low at baseline, after the treatment, and remained equivalent to those of wt mice also at follow-up 2. On the contrary, higher baseline [^{11}C]PIB binding and a clear increase from follow-up 1 to follow-up 2 was detected in **IV**. However, IHC verified the PET findings in both studies, showing

that the low [^{11}C]PIB binding was associated with a low plaque load (Balducci et al., 2014), and higher binding with higher Aβ load at follow-up 2 (**IV**). Younger age (15 months) and lower baseline binding indicates that the initial plaque load was lower in APP23 mice in the previously published study, whereas a more abundant baseline deposition was already present in APP23 mice at 16−17 months in **IV**. Both [^{11}C]PIB binding ratios and Aβ deposition in APP23 mice have been shown to increase with a steep slope between 15 and 20 months (Maier et al., 2014). Together, this data suggests that mApoE-PA-LIPs could be more efficient in inhibiting aggregation and the formation of plaques in APP23 mice, presumably by binding the existing soluble forms of Aβ, rather than clearing already existing large and dense cored deposits. This theory is supported by Mancini and colleagues, who postulated that considering the low levels of the particles reaching the brain, the *in vivo* efficacy of mApoE-PA-LIPs could be due to the ability of circulating mApoE-PA-LIPs to remove oligomeric Aβ from the brain via a "sink effect" (Mancini et al., 2016). However, due to the small animal number and the lack of a proper control group in the study of Balducci and colleagues, these differences should be interpreted with caution.

Recommendations for future studies

To increase the translation of encouraging preclinical anti-amyloid results to the clinical setting, better preclinical study design, including standardized methods similar to those applied in clinical studies, i.e. power analysis, randomization, and reporting also negative studies, has recently been highlighted (Selkoe and Hardy, 2016). For **IV** and other studies in this thesis, the main limiting factor in the study design was the poor availability of the AD mice, impacting on the possibility for conducting proper power calculations and using larger group sizes. However, **II** and **III** were proof of principal studies, and thus it was considered more informative to follow several mouse models with small group numbers, than to monitor a larger group of animals from only one model, whereas in study **IV**, the individual follow-up made it possible to use repeated measures analyses that is much more powerful than one time-point approach. However, the animal number in **IV** was still relatively low, and could be the reason for the difficulties in detecting significant treatment effects between the groups. To avoid this, sample size calculations should be performed also for preclinical studies to increase their translational value.

Animals of mixed gender were included in **IV**, and both females were allocated to the saline group to balance the mean age of the two groups. It would always be optimal to include only male or females in a study, especially as gender differences in the rate of Aβ pathology have previously been reported for APP23 mice (Sturchler-Pierrat and Staufenbiel, 2000). However, as the animals were longitudinally followed, and the baseline values obtained from these individual female mice fit inside the range of the male mice, we decided to include the animals to increase the relatively small sample size.

As an increase in cognition is the primary outcome in clinical studies, it would be beneficial for translational preclinical studies to also include behavioral endpoints in addition to histological evaluation of the reduced plaque load. mApoE-PA-LIP treatment has been previously shown to restore long-term recognition memory in APP_{swe}-$PS1_{dE9}$ mice (Balducci et al., 2014), unfortunately, a similar evaluation could not be performed with APP23 mice in study **IV**.

6.6. Future prospects

Amyloid PET imaging and different Aβ targeting PET tracers have greatly improved our understanding of the temporal course of Aβ pathology in AD, as well as provided valuable information on Aβ deposition in the non-demented population. In the future, amyloid imaging will surely continue to have an important role in early detection and in clinical anti-amyloid trials, both for selection of patients and for follow-up of treatment effects. Even though PET tracers with less non-specific binding and improved sensitivity, i.e. [^{18}F]NAV4694 currently in phase 3 validation trials, are still being developed, multiple ^{18}F-labeled amyloid tracers are already commercially available, and thus the most active PET tracer development has been shifted towards other targets, such as tau. In the future, longitudinal multi-tracer imaging studies combining amyloid PET with tau binding radiotracers (e.g. ^{18}F-THK5117 or ^{18}F-AV-1451), tracers for neuroinflammation (e.g. ^{18}F-DPA-714, binding to translocator protein 18kDa upregulated in microglial activation) and with other novel tracers such as the ^{11}C-UCB-J for imaging synaptic density (Finnema et al., 2016) will provide a way to clarify the temporal relationship of these key pathologies, their role in AD pathogenesis and their value for early detection in persons at risk for AD *in vivo*.

As the possibility to follow anti-amyloid treatment effects with *in vivo* μPET using various tg mice and different Aβ targeting PET tracers has been confirmed, similar longitudinal studies could be included in future preclinical evaluations of novel therapeutic compounds to increase the quality of preclinical data. Evaluation of treatment effects *in vivo* in individual animals would help to decrease the error caused by baseline variation and produce translational data with fewer animals, in addition, longitudinal *in vivo* data could be combined to full post-mortem evaluation of pathological changes in the brain. However, high price might still restrict wider use of μPET imaging. Novel tau PET tracers have already been evaluated in tg models (Brendel et al., 2016a), and in the future, a similar approach to use tau PET for evaluation of novel anti-tau interventions could also prove useful in tg models expressing NFTs. In addition, multi-tracer studies could be performed in tg models to obtain a more detailed perspective of the pathological interplay *in vivo,* and for further validation of the present and novel animal models. However, as shown in this thesis, the applicability of preclinical amyloid imaging to date seems to be limited to tg models with a high plaque load and large and dense cored deposits. In addition, the sensitivity of the current tracers is not sufficient to detect the initial early changes in the plaque load, hence the method is suitable for only therapeutic experiments aiming to decrease already existing deposits. In the future, earlier changes might be monitored by novel tracers binding to other Aβ species, such as Aβ protofibrils in the case of recently published Tribody PET ligand which is based on the monoclonal mAb158 antibody (Syvanen et al., 2017).

The amyloid hypothesis has been dominating drug development for AD for the last two decades even though multiple controversies and inconsistencies still surround the role of Aβ in AD (Morris et al., 2014; Selkoe and Hardy, 2016). For the scientific community to be able to accept the amyloid hypothesis and the true causality between Aβ and AD, a successful anti-amyloid trial would be needed where an Aβ targeting pharmaceutical would achieve a significant improvement in the cognitive performance of human AD patients. To date, such true success stories are unfortunately still not on the horizon. Skeptics have speculated that new anti-amyloid trials are like “beating a dead horse”, while others have put forward logical explanations for the previous failures, i.e. it was not necessarily the wrong target, but rather the wrong stage of the disease, wrong dosage of the drug, inefficient mechanism of action, or limited passage of the drug into the brain (Abbott and Dolgin, 2016; Karran

and Hardy, 2014). Concerning the timing of the treatment, the negative results from the recent phase 3 Solanezumab trial with patients with mild AD further support the idea that for amyloidocentric treatment to be effective, it should be initiated during the pre-dementia phase, as downstream neuronal damage could be too widespread even in the mild dementia phase. In this sense, the prevention trials with asymptomatic at-risk subjects could be considered as a true test of the existing compounds. Should such a positive treatment effect be demonstrated, the optimal time for treating patients with more common LOAD could be during the asymptomatic phase when positive diagnostic biomarkers would be present, further highlighting the significance of research into the biomarkers for early detection of this insidious disease.

It is clear that also divergent ways of thinking, distinct from Aβ, are needed for explaining the complicated pathological processes involved in AD, and stimulate novel approaches in this research field in the future. Taking into consideration the extremely complicated and long-lasting pathophysiological processes behind AD, it is easier to imagine that combination therapies, e.g. simultaneously tackling Aβ production, clearance, accompanying inflammatory processes, and/or tangle formation, rather than one single "magic bullet" might prove useful in the future. It will be very interesting to see the outcome of the ongoing prevention trials and novel anti-amyloid approaches; however, it would also be important to pay due attention to differing interpretations and alternative hypotheses, as this is the only way that a deeper understanding of the pathological processes behind AD can be achieved.

"Whenever a theory appears to you as the only possible one, take this as a sign that you have neither understood the theory nor the problem which it was intended to solve"

–Karl Popper (as quoted in Morris et al., 2014)

7. CONCLUSIONS

The studies included in this thesis demonstrated that the investigated Aβ targeting PET tracers, [^{11}C]PIB and [^{18}F]flutemetamol, had suitable properties for μPET imaging. In addition to their value for clinical research purposes, they could be used in preclinical drug development in the evaluation of temporal changes in Aβ deposition in tg animal models. However, positive amyloid PET indicated increased Aβ deposition only in the tg APP23 model, indicating that the usability of the μPET method is limited with tg models expressing lower plaque loads and different plaque morphologies. In addition, early pathological changes cannot be detected with [^{11}C]PIB and [^{18}F]flutemetamol PET.

The key conclusions of the work presented in this thesis are:

1. Pharmacokinetic properties of novel Aβ targeting PET tracer [^{18}F]flutemetamol were suitable for future preclinical imaging studies. [^{18}F]flutemetamol bound to Aβ deposits in Tg2576 mouse brain *ex vivo*, and its pharmacokinetic profile in rodents was similar to [^{11}C]PIB, the present gold standard of amyloid imaging. However, due to its higher lipophilicity, its clearance from the brain was slower.
2. Temporal changes in Aβ deposition were followed in tg mouse brain using *in vivo* PET imaging and [^{11}C]PIB with a moderate SA. However, [^{11}C]PIB retention increased in parallel with age only in the APP23 mouse model of AD, not in the Tg2576 and APP_{swe}-$PS1_{dE9}$ models. Detection of changes in Aβ deposition is possible *in vivo*, however, careful consideration of the phenotype of the mouse model in use is required prior to embarking on longitudinal imaging studies using [^{11}C]PIB.
3. The high SA of [^{18}F]flutemetamol did not confer the expected additional benefit to the *in vivo* PET imaging of Aβ deposition in tg mouse models of AD. Increased [^{18}F]flutemetamol retention was observed only in the brain of aging APP23 mice, whereas no increase was seen in the Tg2576 and APP_{swe}-$PS1_{dE9}$ models. Similar to findings when [^{11}C]PIB was investigated, the mouse model being used and its plaque phenotype had a greater impact on the success of *in vivo* amyloid imaging studies than the SA of the tracer.
4. [^{11}C]PIB binding in APP23 mouse brain correlated well with the existing Aβ pathology and can thus be used as a biomarker to evaluate longitudinal changes in cerebral Aβ deposition *in vivo*. The data from this study further supports the use of longitudinal *in vivo* μPET follow-up of individual APP23 tg mice in the preclinical phase of AD drug development, and represents a foundation for further studies using mApoE-PA-LIPs.

ACKNOWLEDGEMENTS

This work was carried out in Turku PET Centre, Institute of Clinical Medicine, Department of Clinical Physiology and Nuclear Medicine and in MediCity Research Laboratory, University of Turku, Turku, Finland. I want to thank Professor Juhani Knuuti, the Director of Turku PET Centre, Professor Jaakko Hartiala, the Head of the Department of Clinical Physiology and Nuclear Medicine, and Professor Sirpa Jalkanen, the Head of MediCity Research Laboratory, for providing such excellent research facilities for executing this project.

I wish to express my deepest gratitude for the three supervisors of this thesis, Adjunct Professor Merja Haaparanta-Solin, Professor Juha O. Rinne and Professor Olof Solin, it has been a privilege to start my scientific journey with mentors like you. I am most grateful to Merja, thank you for sharing your wide knowledge about PET imaging and preclinical research, and for your kind and encouraging guidance through this whole process. From the very beginning, you have always made me feel like a colleague, rather than a student, and I am grateful for everything I have learned from you during these years. Juha, thank you for introducing me to Alzheimer's research and for giving me the opportunity to begin to work in this project, as well as in the two exciting EU projects. Your positive and encouraging attitude and confidence in me has been motivating throughout this project. Olof, your enthusiasm and passion for science impressed me from the first time I attended your lectures. Thank you for guiding me into the world of radiopharmaceuticals and for all the support and interesting discussions during these years.

I owe my gratitude to the official reviewers of the thesis, Professor Heikki Tanila and Dr. Hervé Boutin. Your excellent comments, suggestions and criticism helped to improve the quality of this thesis significantly. In addition, I want to acknowledge my follow-up committee members, Adjunct Professor Irma Holopainen and Professor Markku Koulu, for all the valuable discussions we have had during the meetings. I also warmly thank the Drug Research Doctoral Programme and Professor Markku Koulu as its director, for the provided financial support and educational possibilities. In addition, I want to acknowledge Eeva Valve for all the assistance in graduate school related matters. I also want to thank all the fellow DRDP students for their excellent company during the annual meetings and other social events. Turku Brain and Mind Center is warmly acknowledged for providing working space for the writing process.

I am deeply grateful for my co-authors for their valuable contributions that enabled the completion of this study. I am most grateful to Johanna Rokka for her irreplaceable role in this work. All the additional syntheses, hard work and extra efforts, especially for study I and for finalizing the liposome work, are highly appreciated. I also want to acknowledge Francisco López-Picón for sharing his wide expertise in neuroscience that both increased the quality of this work, and helped me grow as a neuroscientist. Professor Mika Scheinin is sincerely thanked for his contribution to studies II and III, and for all the excellent comments on the prepared manuscripts. Olli Eskola and Semi Helin are warmly acknowledged for their expertise in radiochemistry, Rea Pihlaja for her contribution to the biochemical analyses, and Eliisa Löyttyniemi for her expertise in statistics. Ian Wilson and Gill Farrar from GE Healthcare are acknowledged for the collaboration in study I.

All the collaborators and co-authors within the NAD project are most warmly acknowledged, I feel privileged having been a part of such a successful project. Professor Massimo Masserini, Francesca Re, Mario Salmona and Gianluigi Forloni are thanked for all their efforts that enabled the execution

of study IV, as well as for providing the APP23 mice that were crucial for this work. In particular, I am grateful for Dr. Salmona for the discussions that helped to significantly improve the last manuscript.

I owe my gratitude for Elisa Riuttala for the valuable work she did in the animal experiments. In addition, I want to thank Marko Vehmanen and Tarja Marttila for their assistance in the animal work, and Aake Honkaniemi, Marko Tirri and Leena Tokoi-Eklund for the excellent work they did in running the small animal PET/CT. In addition, Aake is warmly thanked for scheduling the PET studies, especially for all his efforts that enabled the execution of study IV.

I wish to thank the whole core personnel and colleagues at Turku PET Centre for all the help I have received during these years, as well as the professional and friendly environment I always encountered. I want to acknowledge the personnel of the Accelerator Laboratory for radionuclide production, and the personnel of the Radiopharmaceutical Chemistry Laboratory for the production of the used tracers. Without this valuable work, my work could not have been done. Vesa Oikonen is also warmly thanked for his modelling expertise and advice concerning the PET data analysis.

I want to sincerely thank all the present and former members of the PET MediCity laboratory, I have been lucky to have such skilled and nice colleagues to work with. Tove Grönroos, Kirsi Mikkola, Jonna Sinkkonen, Francisco López-Picón, Jatta Takkinen, Susanne Vainio, Tamiko Ishizu, Rea Pihlaja, Johanna Tuomela, Veronica Fagerholm, Päivi Marjamäki, and all the other researchers, post docs and students that I have got to meet and work with during these years, thank you for a pleasant and professional working environment. Kirsi, thank you for going through these last few months with me. I am happy to get to finish this process with the person that I started it with, and to have found such a good friend along the way.

I am grateful for all the wonderful friends I have in my life, both in and outside science. All the girls from our Tbio2k3 group, thank you for your friendship and all the memorable moments we have shared since 2003. Anu, and our godsons Jami and Joel, thank you for being there, no matter the distance. TYKin tytöt, Pauliina, Nora, Maija, Johanna, Soila and Laura, thank you for your long and valuable friendship and for always keeping it real! I also want to thank the whole big wonderful Snellman family for their interest towards my work and all the help our family has received. Pets and Boys, thank you for bringing more music into my life.

Finally, I owe my deepest gratitude to my family. My parents Pia and Asko, you have always been there when needed, but having confidence in me so I could make my own decisions. I know you, and my brother Aleksi, would have been supportive and proud of me whatever I would have decided to do in my life, thank you for all your love and support. Ronnie, these last months would have been impossible without you in my team. Thank you for putting all your own interests on hold, and taking care of everything while my mind was somewhere else. Your endless love, confidence and belief in me means more than you will ever know. My boys, Vilmer and Alvar, the most important lessons in life I am continuously learning with you and from you. Every single day you make me so happy and proud to be your mother, I hope someday this work will make you proud too.

The research leading to these findings has received funding from the European Community's 6th and 7th framework Programmes under grant agreement no. 511977 (FP6/2005-2010, ADIT), no. 212043 (FP7/2007-2013, NAD) and HEALTH-F2-20011-278850 (INMiND), Finnish Cultural Foundation,

Academy of Finland (project 17652), Sigrid Jusélius Foundation, Maud Kuistila Memory Foundation, Drug Research Doctoral Programme, and state funding for university level health research, Turku University Hospital (ERVA). All this financial support is greatly acknowledged.

Turku, May 2017

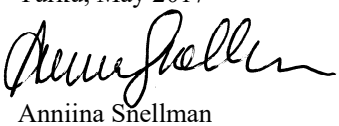

Anniina Snellman

REFERENCES

Abbott, A., and Dolgin, E. (2016). Failed Alzheimer's trial does not kill leading theory of disease. Nature *540*, 15-16.

Agdeppa, E.D., Kepe, V., Liu, J., Flores-Torres, S., Satyamurthy, N., Petric, A., Cole, G.M., Small, G.W., Huang, S.C., and Barrio, J.R. (2001). Binding characteristics of radiofluorinated 6-dialkylamino-2-naphthylethylidene derivatives as positron emission tomography imaging probes for beta-amyloid plaques in Alzheimer's disease. J Neurosci *21*, Rc189.

Agdeppa, E.D., Kepe, V., Petri, A., Satyamurthy, N., Liu, J., Huang, S.C., Small, G.W., Cole, G.M., and Barrio, J.R. (2003). In vitro detection of (S)-naproxen and ibuprofen binding to plaques in the Alzheimer's brain using the positron emission tomography molecular imaging probe 2-(1-[6-[(2-[(18)F]fluoroethyl)(methyl)amino]-2-naphthyl]ethylidene)malononitrile. Neuroscience *117*, 723-730.

Aisen, P.S., Gauthier, S., Ferris, S.H., Saumier, D., Haine, D., Garceau, D., Duong, A., Suhy, J., Oh, J., Lau, W.C*., et al.* (2011). Tramiprosate in mild-to-moderate Alzheimer's disease - a randomized, double-blind, placebo-controlled, multi-centre study (the Alphase Study). Arch Med Sci *7*, 102-111.

Alzheimer's Association (2015). 2015 Alzheimer's disease facts and figures. Alzheimers Dement *11*, 332-384.

Anand, R., Gill, K.D., and Mahdi, A.A. (2014). Therapeutics of Alzheimer's disease: Past, present and future. Neuropharmacology *76 Pt A*, 27-50.

Bacskai, B.J., Hickey, G.A., Skoch, J., Kajdasz, S.T., Wang, Y., Huang, G.F., Mathis, C.A., Klunk, W.E., and Hyman, B.T. (2003). Four-dimensional multiphoton imaging of brain entry, amyloid binding, and clearance of an amyloid-beta ligand in transgenic mice. Proc Natl Acad Sci U S A *100*, 12462-12467.

Balducci, C., Mancini, S., Minniti, S., La Vitola, P., Zotti, M., Sancini, G., Mauri, M., Cagnotto, A., Colombo, L., Fiordaliso, F*., et al.* (2014). Multifunctional liposomes reduce brain β-amyloid burden and ameliorate memory impairment in Alzheimer's disease mouse models. J Neurosci *34*, 14022-14031.

Bana, L., Minniti, S., Salvati, E., Sesana, S., Zambelli, V., Cagnotto, A., Orlando, A., Cazzaniga, E., Zwart, R., Scheper, W*., et al.* (2014). Liposomes bi-functionalized with phosphatidic acid and an ApoE-derived peptide affect Aβ aggregation features and cross the blood-brain-barrier: implications for therapy of Alzheimer disease. Nanomedicine *10*, 1583-1590.

Bartus, R.T., Dean, R.L., 3rd, Beer, B., and Lippa, A.S. (1982). The cholinergic hypothesis of geriatric memory dysfunction. Science *217*, 408-414.

Beekman, F.J., van der Have, F., Vastenhouw, B., van der Linden, A.J., van Rijk, P.P., Burbach, J.P., and Smidt, M.P. (2005). U-SPECT-I: a novel system for submillimeter-resolution tomography with radiolabeled molecules in mice. J Nucl Med *46*, 1194-1200.

Birks, J. (2006). Cholinesterase inhibitors for Alzheimer's disease. Cochrane Database Syst Rev, Cd005593.

Blennow, K., de Leon, M.J., and Zetterberg, H. (2006). Alzheimer's disease. Lancet *368*, 387-403.

Boche, D., and Nicoll, J.A. (2008). The role of the immune system in clearance of Abeta from the brain. Brain Pathol *18*, 267-278.

Borchelt, D.R., Thinakaran, G., Eckman, C.B., Lee, M.K., Davenport, F., Ratovitsky, T., Prada, C.M., Kim, G., Seekins, S., Yager, D*., et al.* (1996). Familial Alzheimer's disease-linked presenilin 1 variants elevate Abeta1-42/1-40 ratio in vitro and in vivo. Neuron *17*, 1005-1013.

Braak, H., and Braak, E. (1991). Neuropathological stageing of Alzheimer-related changes. Acta Neuropathol *82*, 239-259.

Braak, H., and Braak, E. (1997). Frequency of stages of Alzheimer-related lesions in different age categories. Neurobiol Aging *18*, 351-357.

Braak, H., Braak, E., Ohm, T., and Bohl, J. (1989). Alzheimer's disease: mismatch between amyloid plaques and neuritic plaques. Neurosci Lett *103*, 24-28.

Braak, H., and Del Tredici, K. (2015). The preclinical phase of the pathological process underlying sporadic Alzheimer's disease. Brain *138*, 2814-2833.

Brendel, M., Delker, A., Rötzer, C., Böning, G., Carlsen, J., Cyran, C., Mille, E., Gildehaus, F.J., Cumming, P., Baumann, K*., et al.* (2014). Impact of partial volume effect correction on cerebral β-amyloid imaging in APP-Swe mice using [(18)F]-florbetaben PET. Neuroimage *84*, 843-853.

Brendel, M., Jaworska, A., Grießinger, E., Rötzer, C., Burgold, S., Gildehaus, F.J., Carlsen, J., Cumming, P., Baumann, K., Haass, C*., et al.* (2015a). Cross-Sectional Comparison of Small Animal [18F]-Florbetaben Amyloid-PET between Transgenic AD Mouse Models. PLoS One *10*, e0116678.

Brendel, M., Jaworska, A., Herms, J., Trambauer, J., Rötzer, C., Gildehaus, F.J., Carlsen, J., Cumming, P., Bylund, J., Luebbers, T*., et al.* (2015b). Amyloid-PET predicts inhibition of de novo plaque formation upon chronic γ-secretase modulator treatment. Mol Psychiatry *20*, 1179-1187.

Brendel, M., Jaworska, A., Herms, J., Trambauer, J., Rötzer, C., Gildehaus, F.J., Carlsen, J., Cumming, P., Bylund, J., Luebbers, T*., et al.* (2015c). Monitoring of chronic γ-secretase modulator treatment by serial amyloid-PET. Mol Psychiatry *20*, 1141.

Brendel, M., Jaworska, A., Probst, F., Overhoff, F., Korzhova, V., Lindner, S., Carlsen, J., Bartenstein, P., Harada, R., Kudo, Y*., et al.* (2016a). Small-Animal PET

Imaging of Tau Pathology with 18F-THK5117 in 2 Transgenic Mouse Models. J Nucl Med *57*, 792-798.

Brendel, M., Probst, F., Jaworska, A., Overhoff, F., Korzhova, V., Albert, N.L., Beck, R., Lindner, S., Gildehaus, F.J., Baumann, K.*, et al.* (2016b). Glial Activation and Glucose Metabolism in a Transgenic Amyloid Mouse Model: A Triple-Tracer PET Study. J Nucl Med *57*, 954-960.

Buee, L., Bussiere, T., Buee-Scherrer, V., Delacourte, A., and Hof, P.R. (2000). Tau protein isoforms, phosphorylation and role in neurodegenerative disorders. Brain Res Brain Res Rev *33*, 95-130.

Calhoun, M.E., Wiederhold, K.H., Abramowski, D., Phinney, A.L., Probst, A., Sturchler-Pierrat, C., Staufenbiel, M., Sommer, B., and Jucker, M. (1998). Neuron loss in APP transgenic mice. Nature *395*, 755-756.

Chen, C.J., Bando, K., Ashino, H., Taguchi, K., Shiraishi, H., Shima, K., Fujimoto, O., Kitamura, C., Matsushima, S., Uchida, K.*, et al.* (2015). In vivo SPECT imaging of amyloid-beta deposition with radioiodinated imidazo[1,2-a]pyridine derivative DRM106 in a mouse model of Alzheimer's disease. J Nucl Med *56*, 120-126.

Cherry, S., and Dahlblom, M. (2004). PET: Physics, Instrumentation and scanners. In PET Molecular Imaging and Its Biological Applications, M. Phelps, ed. (New York, NY, 10010 USA: Springer).

Chin, J. (2011). Selecting a mouse model of Alzheimer's disease. Methods Mol Biol *670*, 169-189.

Chishti, M.A., Yang, D.S., Janus, C., Phinney, A.L., Horne, P., Pearson, J., Strome, R., Zuker, N., Loukides, J., French, J.*, et al.* (2001). Early-onset amyloid deposition and cognitive deficits in transgenic mice expressing a double mutant form of amyloid precursor protein 695. J Biol Chem *276*, 21562-21570.

Choi, S.H., Kim, Y.H., Hebisch, M., Sliwinski, C., Lee, S., D'Avanzo, C., Chen, H., Hooli, B., Asselin, C., Muffat, J.*, et al.* (2014). A three-dimensional human neural cell culture model of Alzheimer's disease. Nature *515*, 274-278.

Choi, S.R., Golding, G., Zhuang, Z., Zhang, W., Lim, N., Hefti, F., Benedum, T.E., Kilbourn, M.R., Skovronsky, D., and Kung, H.F. (2009). Preclinical properties of 18F-AV-45: a PET agent for Abeta plaques in the brain. J Nucl Med *50*, 1887-1894.

Claeysen, S., Cochet, M., Donneger, R., Dumuis, A., Bockaert, J., and Giannoni, P. (2012). Alzheimer culprits: cellular crossroads and interplay. Cell Signal *24*, 1831-1840.

Cohen, R.M., Rezai-Zadeh, K., Weitz, T.M., Rentsendorj, A., Gate, D., Spivak, I., Bholat, Y., Vasilevko, V., Glabe, C.G., Breunig, J.J.*, et al.* (2013). A transgenic Alzheimer rat with plaques, tau pathology, behavioral impairment, oligomeric aβ, and frank neuronal loss. J Neurosci *33*, 6245-6256.

Cole, G.B., Keum, G., Liu, J., Small, G.W., Satyamurthy, N., Kepe, V., and Barrio, J.R. (2010). Specific estrogen sulfotransferase (SULT1E1) substrates and molecular imaging probe candidates. Proc Natl Acad Sci U S A *107*, 6222-6227.

Colvin, M.T., Silvers, R., Ni, Q.Z., Can, T.V., Sergeyev, I., Rosay, M., Donovan, K.J., Michael, B., Wall, J., Linse, S.*, et al.* (2016). Atomic Resolution Structure of Monomorphic Abeta42 Amyloid Fibrils. J Am Chem Soc *138*, 9663-9674.

Cselényi, Z., Jönhagen, M.E., Forsberg, A., Halldin, C., Julin, P., Schou, M., Johnström, P., Varnäs, K., Svensson, S., and Farde, L. (2012). Clinical validation of 18F-AZD4694, an amyloid-β-specific PET radioligand. J Nucl Med *53*, 415-424.

Dawkins, E., and Small, D.H. (2014). Insights into the physiological function of the β-amyloid precursor protein: beyond Alzheimer's disease. J Neurochem *129*, 756-769.

Deane, R., Du Yan, S., Submamaryan, R.K., LaRue, B., Jovanovic, S., Hogg, E., Welch, D., Manness, L., Lin, C., Yu, J.*, et al.* (2003). RAGE mediates amyloid-beta peptide transport across the blood-brain barrier and accumulation in brain. Nat Med *9*, 907-913.

Do Carmo, S., and Cuello, A.C. (2013). Modeling Alzheimer's disease in transgenic rats. In Mol Neurodegener, p. 37.

Doody, R.S., Raman, R., Farlow, M., Iwatsubo, T., Vellas, B., Joffe, S., Kieburtz, K., He, F., Sun, X., Thomas, R.G.*, et al.* (2013). A phase 3 trial of semagacestat for treatment of Alzheimer's disease. N Engl J Med *369*, 341-350.

Doody, R.S., Thomas, R.G., Farlow, M., Iwatsubo, T., Vellas, B., Joffe, S., Kieburtz, K., Raman, R., Sun, X., Aisen, P.S.*, et al.* (2014). Phase 3 trials of solanezumab for mild-to-moderate Alzheimer's disease. N Engl J Med *370*, 311-321.

Dubois, B., Feldman, H.H., Jacova, C., Hampel, H., Molinuevo, J.L., Blennow, K., DeKosky, S.T., Gauthier, S., Selkoe, D., Bateman, R.*, et al.* (2014). Advancing research diagnostic criteria for Alzheimer's disease: the IWG-2 criteria. Lancet Neurol *13*, 614-629.

Duyckaerts, C. (2011). Tau pathology in children and young adults: can you still be unconditionally baptist? Acta Neuropathol *121*, 145-147.

Duyckaerts, C., Delatour, B., and Potier, M.C. (2009). Classification and basic pathology of Alzheimer disease. Acta Neuropathol *118*, 5-36.

Duyckaerts, C., Potier, M.C., and Delatour, B. (2008). Alzheimer disease models and human neuropathology: similarities and differences. Acta Neuropathol *115*, 5-38.

Dyrks, T., Dyrks, E., Masters, C.L., and Beyreuther, K. (1993). Amyloidogenicity of rodent and human beta A4 sequences. FEBS Lett *324*, 231-236.

Echeverria, V., Ducatenzeiler, A., Dowd, E., Janne, J., Grant, S.M., Szyf, M., Wandosell, F., Avila, J., Grimm, H., Dunnett, S.B.*, et al.* (2004). Altered mitogen-activated

protein kinase signaling, tau hyperphosphorylation and mild spatial learning dysfunction in transgenic rats expressing the beta-amyloid peptide intracellularly in hippocampal and cortical neurons. Neuroscience *129*, 583-592.

Eli Lilly and Company (2016). Lilly Announces Top-Line Results of Solanezumab Phase 3 Clinical Trial (https://investor.lilly.com/releasedetail.cfm?ReleaseID=1000871).

Esparza, T.J., Zhao, H., Cirrito, J.R., Cairns, N.J., Bateman, R.J., Holtzman, D.M., and Brody, D.L. (2013). Amyloid-beta oligomerization in Alzheimer dementia versus high-pathology controls. Ann Neurol *73*, 104-119.

Ferrieri, R.A. (2003). Production and application of synthetic precursors labelled with carbon-11 and fluorine-18. In Handbook of radiopharmaceuticals, radiochemistry and applications, M.J. Welch, and C.S. Redvanly, eds. (Wiley).

Finnema, S.J., Nabulsi, N.B., Eid, T., Detyniecki, K., Lin, S.F., Chen, M.K., Dhaher, R., Matuskey, D., Baum, E., Holden, D.*, et al.* (2016). Imaging synaptic density in the living human brain. Sci Transl Med *8*, 348ra396.

Folkesson, R., Malkiewicz, K., Kloskowska, E., Nilsson, T., Popova, E., Bogdanovic, N., Ganten, U., Ganten, D., Bader, M., Winblad, B.*, et al.* (2007). A transgenic rat expressing human APP with the Swedish Alzheimer's disease mutation. Biochem Biophys Res Commun *358*, 777-782.

Franklin, K.B.J., and Paxinos, G. (2008). The Mouse Brain in Stereotactic Coordinates, Third edition edn (Academic Press).

Furumoto, S., Okamura, N., Iwata, R., Yanai, K., Arai, H., and Kudo, Y. (2007). Recent advances in the development of amyloid imaging agents. Curr Top Med Chem *7*, 1773-1789.

Gambhir, S. (2004). Quantitative Assay Development for PET. In PET - Molecular Imaging and Its Biological Applications, M. Phelps, ed. (Springer-Verlag New York, Inc.).

Garcia-Alloza, M., Robbins, E.M., Zhang-Nunes, S.X., Purcell, S.M., Betensky, R.A., Raju, S., Prada, C., Greenberg, S.M., Bacskai, B.J., and Frosch, M.P. (2006). Characterization of amyloid deposition in the APPswe/PS1dE9 mouse model of Alzheimer disease. Neurobiol Dis *24*, 516-524.

Glenner, G.G., and Wong, C.W. (1984a). Alzheimer's disease and Down's syndrome: sharing of a unique cerebrovascular amyloid fibril protein. Biochem Biophys Res Commun *122*, 1131-1135.

Glenner, G.G., and Wong, C.W. (1984b). Alzheimer's disease: initial report of the purification and characterization of a novel cerebrovascular amyloid protein. Biochem Biophys Res Commun *120*, 885-890.

Goate, A., Chartier-Harlin, M.C., Mullan, M., Brown, J., Crawford, F., Fidani, L., Giuffra, L., Haynes, A., Irving, N., James, L.*, et al.* (1991). Segregation of a missense mutation in the amyloid precursor protein gene with familial Alzheimer's disease. Nature *349*, 704-706.

Gobbi, M., Re, F., Canovi, M., Beeg, M., Gregori, M., Sesana, S., Sonnino, S., Brogioli, D., Musicanti, C., Gasco, P.*, et al.* (2010). Lipid-based nanoparticles with high binding affinity for amyloid-beta1-42 peptide. Biomaterials *31*, 6519-6529.

Gotz, J., Chen, F., van Dorpe, J., and Nitsch, R.M. (2001). Formation of neurofibrillary tangles in P3011 tau transgenic mice induced by Abeta 42 fibrils. Science *293*, 1491-1495.

Green, R.C., Cupples, L.A., Go, R., Benke, K.S., Edeki, T., Griffith, P.A., Williams, M., Hipps, Y., Graff-Radford, N., Bachman, D.*, et al.* (2002). Risk of dementia among white and African American relatives of patients with Alzheimer disease. Jama *287*, 329-336.

Haass, C., Schlossmacher, M.G., Hung, A.Y., Vigo-Pelfrey, C., Mellon, A., Ostaszewski, B.L., Lieberburg, I., Koo, E.H., Schenk, D., Teplow, D.B.*, et al.* (1992). Amyloid beta-peptide is produced by cultured cells during normal metabolism. Nature *359*, 322-325.

Hanzel, C.E., Pichet-Binette, A., Pimentel, L.S., Iulita, M.F., Allard, S., Ducatenzeiler, A., Do Carmo, S., and Cuello, A.C. (2014). Neuronal driven pre-plaque inflammation in a transgenic rat model of Alzheimer's disease. Neurobiol Aging *35*, 2249-2262.

Hardy, J., Bogdanovic, N., Winblad, B., Portelius, E., Andreasen, N., Cedazo-Minguez, A., and Zetterberg, H. (2014). Pathways to Alzheimer's disease. J Intern Med *275*, 296-303.

Hardy, J., and Selkoe, D.J. (2002). The amyloid hypothesis of Alzheimer's disease: progress and problems on the road to therapeutics. Science *297*, 353-356.

Hardy, J.A., and Higgins, G.A. (1992). Alzheimer's disease: the amyloid cascade hypothesis. Science *256*, 184-185.

Hefendehl, J.K., Wegenast-Braun, B.M., Liebig, C., Eicke, D., Milford, D., Calhoun, M.E., Kohsaka, S., Eichner, M., and Jucker, M. (2011). Long-term in vivo imaging of beta-amyloid plaque appearance and growth in a mouse model of cerebral beta-amyloidosis. J Neurosci *31*, 624-629.

Heneka, M.T., Carson, M.J., El Khoury, J., Landreth, G.E., Brosseron, F., Feinstein, D.L., Jacobs, A.H., Wyss-Coray, T., Vitorica, J., Ransohoff, R.M.*, et al.* (2015). Neuroinflammation in Alzheimer's disease. Lancet Neurol *14*, 388-405.

Heurling, K., Leuzy, A., Zimmer, E.R., Lubberink, M., and Nordberg, A. (2016). Imaging beta-amyloid using [(18)F]flutemetamol positron emission tomography: from dosimetry to clinical diagnosis. Eur J Nucl Med Mol Imaging *43*, 362-373.

Hori, Y., Takeda, S., Cho, H., Wegmann, S., Shoup, T.M., Takahashi, K., Irimia, D., Elmaleh, D.R., Hyman, B.T., and Hudry, E. (2015). A Food and Drug Administration-approved asthma therapeutic agent impacts amyloid beta

in the brain in a transgenic model of Alzheimer disease. J Biol Chem *290*, 1966-1978.

Hsiao, K., Chapman, P., Nilsen, S., Eckman, C., Harigaya, Y., Younkin, S., Yang, F., and Cole, G. (1996). Correlative memory deficits, Abeta elevation, and amyloid plaques in transgenic mice. Science *274*, 99-102.

Huang, H., Nie, S., Cao, M., Marshall, C., Gao, J., Xiao, N., Hu, G., and Xiao, M. (2016). Characterization of AD-like phenotype in aged APPSwe/PS1dE9 mice. Age (Dordr) *38*, 303-322.

Ikonomovic, M.D., Klunk, W.E., Abrahamson, E.E., Mathis, C.A., Price, J.C., Tsopelas, N.D., Lopresti, B.J., Ziolko, S., Bi, W., Paljug, W.R*., et al.* (2008). Post-mortem correlates of in vivo PiB-PET amyloid imaging in a typical case of Alzheimer's disease. Brain *131*, 1630-1645.

Jack, C.R., Knopman, D.S., Jagust, W.J., Petersen, R.C., Weiner, M.W., Aisen, P.S., Shaw, L.M., Vemuri, P., Wiste, H.J., Weigand, S.D*., et al.* (2013). Tracking pathophysiological processes in Alzheimer's disease: an updated hypothetical model of dynamic biomarkers. Lancet Neurol *12*, 207-216.

Jack, C.R., Knopman, D.S., Jagust, W.J., Shaw, L.M., Aisen, P.S., Weiner, M.W., Petersen, R.C., and Trojanowski, J.Q. (2010). Hypothetical model of dynamic biomarkers of the Alzheimer's pathological cascade. Lancet Neurol *9*, 119-128.

Jack, C.R., Wiste, H.J., Weigand, S.D., Rocca, W.A., Knopman, D.S., Mielke, M.M., Lowe, V.J., Senjem, M.L., Gunter, J.L., Preboske, G.M*., et al.* (2014). Age-specific population frequencies of cerebral β-amyloidosis and neurodegeneration among people with normal cognitive function aged 50-89 years: a cross-sectional study. Lancet Neurol *13*, 997-1005.

Jankowsky, J.L., Fadale, D.J., Anderson, J., Xu, G.M., Gonzales, V., Jenkins, N.A., Copeland, N.G., Lee, M.K., Younkin, L.H., Wagner, S.L*., et al.* (2004). Mutant presenilins specifically elevate the levels of the 42 residue beta-amyloid peptide in vivo: evidence for augmentation of a 42-specific gamma secretase. Hum Mol Genet *13*, 159-170.

Jankowsky, J.L., Slunt, H.H., Ratovitski, T., Jenkins, N.A., Copeland, N.G., and Borchelt, D.R. (2001a). Co-expression of multiple transgenes in mouse CNS: a comparison of strategies. Biomol Eng *17*, 157-165.

Jicha, G.A., Parisi, J.E., Dickson, D.W., Johnson, K., Cha, R., Ivnik, R.J., Tangalos, E.G., Boeve, B.F., Knopman, D.S., Braak, H*., et al.* (2006). Neuropathologic outcome of mild cognitive impairment following progression to clinical dementia. Arch Neurol *63*, 674-681.

Johnson, A.E., Jeppsson, F., Sandell, J., Wensbo, D., Neelissen, J.A., Juréus, A., Ström, P., Norman, H., Farde, L., and Svensson, S.P. (2009). AZD2184: a radioligand for sensitive detection of beta-amyloid deposits. J Neurochem *108*, 1177-1186.

Johnson, K.A., Minoshima, S., Bohnen, N.I., Donohoe, K.J., Foster, N.L., Herscovitch, P., Karlawish, J.H., Rowe, C.C., Carrillo, M.C., Hartley, D.M*., et al.* (2013). Appropriate use criteria for amyloid PET: a report of the Amyloid Imaging Task Force, the Society of Nuclear Medicine and Molecular Imaging, and the Alzheimer's Association. Alzheimers Dement *9*, e-1-16.

Jonsson, T., Atwal, J.K., Steinberg, S., Snaedal, J., Jonsson, P.V., Bjornsson, S., Stefansson, H., Sulem, P., Gudbjartsson, D., Maloney, J*., et al.* (2012). A mutation in APP protects against Alzheimer's disease and age-related cognitive decline. Nature *488*, 96-99.

Josephs, K.A., Whitwell, J.L., Ahmed, Z., Shiung, M.M., Weigand, S.D., Knopman, D.S., Boeve, B.F., Parisi, J.E., Petersen, R.C., Dickson, D.W*., et al.* (2008). Beta-amyloid burden is not associated with rates of brain atrophy. Ann Neurol *63*, 204-212.

Juréus, A., Swahn, B.M., Sandell, J., Jeppsson, F., Johnson, A.E., Johnström, P., Neelissen, J.A., Sunnemark, D., Farde, L., and Svensson, S.P. (2010). Characterization of AZD4694, a novel fluorinated Abeta plaque neuroimaging PET radioligand. J Neurochem *114*, 784-794.

Kang, J., Lemaire, H.G., Unterbeck, A., Salbaum, J.M., Masters, C.L., Grzeschik, K.H., Multhaup, G., Beyreuther, K., and Muller-Hill, B. (1987). The precursor of Alzheimer's disease amyloid A4 protein resembles a cell-surface receptor. Nature *325*, 733-736.

Karow, D.S., McEvoy, L.K., Fennema-Notestine, C., Hagler, D.J., Jr., Jennings, R.G., Brewer, J.B., Hoh, C.K., and Dale, A.M. (2010). Relative capability of MR imaging and FDG PET to depict changes associated with prodromal and early Alzheimer disease. Radiology *256*, 932-942.

Karran, E., and Hardy, J. (2014). A critique of the drug discovery and phase 3 clinical programs targeting the amyloid hypothesis for Alzheimer disease. Ann Neurol *76*, 185-205.

Kawarabayashi, T., Younkin, L.H., Saido, T.C., Shoji, M., Ashe, K.H., and Younkin, S.G. (2001). Age-dependent changes in brain, CSF, and plasma amyloid (beta) protein in the Tg2576 transgenic mouse model of Alzheimer's disease. J Neurosci *21*, 372-381.

Keene, C.D., Darvas, M., Kraemer, B., Liggitt, D., Sigurdson, C., and Ladiges, W. (2016). Neuropathological assessment and validation of mouse models for Alzheimer's disease: applying NIA-AA guidelines. In Pathobiol Aging Age Relat Dis (United States), p. 32397.

Kemppainen, N.M., Scheinin, N.M., Koivunen, J., Johansson, J., Toivonen, J.T., Någren, K., Rokka, J., Karrasch, M., Parkkola, R., and Rinne, J.O. (2014). Five-year follow-up of 11C-PIB uptake in Alzheimer's disease and MCI. Eur J Nucl Med Mol Imaging *41*, 283-289.

Kitazawa, M., Medeiros, R., and LaFerla, F.M. (2012). Transgenic Mouse Models of Alzheimer Disease:

Developing a Better Model as a Tool for Therapeutic Interventions. Curr Pharm Des *18*, 1131-1147.

Kivipelto, M., Helkala, E.L., Hanninen, T., Laakso, M.P., Hallikainen, M., Alhainen, K., Soininen, H., Tuomilehto, J., and Nissinen, A. (2001). Midlife vascular risk factors and late-life mild cognitive impairment: A population-based study. Neurology *56*, 1683-1689.

Kivipelto, M., Ngandu, T., Laatikainen, T., Winblad, B., Soininen, H., and Tuomilehto, J. (2006). Risk score for the prediction of dementia risk in 20 years among middle aged people: a longitudinal, population-based study. Lancet Neurol *5*, 735-741.

Klunk, W.E., Engler, H., Nordberg, A., Wang, Y., Blomqvist, G., Holt, D.P., Bergström, M., Savitcheva, I., Huang, G.F., Estrada, S*., et al.* (2004). Imaging brain amyloid in Alzheimer's disease with Pittsburgh Compound-B. Ann Neurol *55*, 306-319.

Klunk, W.E., Lopresti, B.J., Ikonomovic, M.D., Lefterov, I.M., Koldamova, R.P., Abrahamson, E.E., Debnath, M.L., Holt, D.P., Huang, G.F., Shao, L*., et al.* (2005). Binding of the positron emission tomography tracer Pittsburgh compound-B reflects the amount of amyloid-beta in Alzheimer's disease brain but not in transgenic mouse brain. J Neurosci *25*, 10598-10606.

Klunk, W.E., Wang, Y., Huang, G.F., Debnath, M.L., Holt, D.P., and Mathis, C.A. (2001). Uncharged thioflavin-T derivatives bind to amyloid-beta protein with high affinity and readily enter the brain. Life Sci *69*, 1471-1484.

Koivunen, J., Pirttilä, T., Kemppainen, N., Aalto, S., Herukka, S.K., Jauhianen, A.M., Hänninen, T., Hallikainen, M., Någren, K., Rinne, J.O*., et al.* (2008). PET amyloid ligand [11C]PIB uptake and cerebrospinal fluid beta-amyloid in mild cognitive impairment. Dement Geriatr Cogn Disord *26*, 378-383.

Koole, M., Lewis, D.M., Buckley, C., Nelissen, N., Vandenbulcke, M., Brooks, D.J., Vandenberghe, R., and Van Laere, K. (2009). Whole-body biodistribution and radiation dosimetry of 18F-GE067: a radioligand for in vivo brain amyloid imaging. J Nucl Med *50*, 818-822.

Kril, J.J., Hodges, J., and Halliday, G. (2004). Relationship between hippocampal volume and CA1 neuron loss in brains of humans with and without Alzheimer's disease. Neurosci Lett *361*, 9-12.

Lalonde, R., Kim, H.D., Maxwell, J.A., and Fukuchi, K. (2005). Exploratory activity and spatial learning in 12-month-old APP(695)SWE/co+PS1/DeltaE9 mice with amyloid plaques. Neurosci Lett *390*, 87-92.

Lambert, M.P., Barlow, A.K., Chromy, B.A., Edwards, C., Freed, R., Liosatos, M., Morgan, T.E., Rozovsky, I., Trommer, B., Viola, K.L*., et al.* (1998). Diffusible, nonfibrillar ligands derived from Aβ1–42 are potent central nervous system neurotoxins. In Proc Natl Acad Sci U S A, pp. 6448-6453.

Landau, S.M., Breault, C., Joshi, A.D., Pontecorvo, M., Mathis, C.A., Jagust, W.J., Mintun, M.A., and Initiative, A.s.D.N. (2013). Amyloid-β imaging with Pittsburgh compound B and florbetapir: comparing radiotracers and quantification methods. J Nucl Med *54*, 70-77.

Leibson, C.L., Rocca, W.A., Hanson, V.A., Cha, R., Kokmen, E., O'Brien, P.C., and Palumbo, P.J. (1997). The risk of dementia among persons with diabetes mellitus: a population-based cohort study. Ann N Y Acad Sci *826*, 422-427.

Leinonen, V., Alafuzoff, I., Aalto, S., Suotunen, T., Savolainen, S., Någren, K., Tapiola, T., Pirttilä, T., Rinne, J., Jääskeläinen, J.E*., et al.* (2008). Assessment of beta-amyloid in a frontal cortical brain biopsy specimen and by positron emission tomography with carbon 11-labeled Pittsburgh Compound B. Arch Neurol *65*, 1304-1309.

Leinonen, V., Rinne, J.O., Virtanen, K.A., Eskola, O., Rummukainen, J., Huttunen, J., von Und Zu Fraunberg, M., Nerg, O., Koivisto, A.M., Rinne, J*., et al.* (2013). Positron emission tomography with [18F]flutemetamol and [11C]PiB for in vivo detection of cerebral cortical amyloid in normal pressure hydrocephalus patients. Eur J Neurol *20*, 1043-1052.

Leon, W.C., Canneva, F., Partridge, V., Allard, S., Ferretti, M.T., DeWilde, A., Vercauteren, F., Atifeh, R., Ducatenzeiler, A., Klein, W*., et al.* (2010). A novel transgenic rat model with a full Alzheimer's-like amyloid pathology displays pre-plaque intracellular amyloid-beta-associated cognitive impairment. J Alzheimers Dis *20*, 113-126.

Levy-Lahad, E., Wijsman, E.M., Nemens, E., Anderson, L., Goddard, K.A., Weber, J.L., Bird, T.D., and Schellenberg, G.D. (1995). A familial Alzheimer's disease locus on chromosome 1. Science *269*, 970-973.

Lewis, J., Dickson, D.W., Lin, W.L., Chisholm, L., Corral, A., Jones, G., Yen, S.H., Sahara, N., Skipper, L., Yager, D*., et al.* (2001). Enhanced neurofibrillary degeneration in transgenic mice expressing mutant tau and APP. Science *293*, 1487-1491.

Li, Y., Rinne, J.O., Mosconi, L., Pirraglia, E., Rusinek, H., DeSanti, S., Kemppainen, N., Någren, K., Kim, B.C., Tsui, W*., et al.* (2008). Regional analysis of FDG and PIB-PET images in normal aging, mild cognitive impairment, and Alzheimer's disease. Eur J Nucl Med Mol Imaging *35*, 2169-2181.

Liu, G., Men, P., Kudo, W., Perry, G., and Smith, M.A. (2009). Nanoparticle-chelator conjugates as inhibitors of amyloid-beta aggregation and neurotoxicity: a novel therapeutic approach for Alzheimer disease. Neurosci Lett *455*, 187-190.

Liu, L., Orozco, I.J., Planel, E., Wen, Y., Bretteville, A., Krishnamurthy, P., Wang, L., Herman, M., Figueroa, H., Yu, W.H*., et al.* (2008). A transgenic rat that develops Alzheimer's disease-like amyloid pathology, deficits in synaptic plasticity and cognitive impairment. Neurobiol Dis *31*, 46-57.

Luurtsema, G., Schuit, R.C., Takkenkamp, K., Lubberink, M., Hendrikse, N.H., Windhorst, A.D., Molthoff, C.F., Tolboom, N., van Berckel, B.N., and Lammertsma, A.A. (2008). Peripheral metabolism of [(18)F]FDDNP and

cerebral uptake of its labelled metabolites. Nucl Med Biol *35*, 869-874.

Maeda, J., Ji, B., Irie, T., Tomiyama, T., Maruyama, M., Okauchi, T., Staufenbiel, M., Iwata, N., Ono, M., Saido, T.C.*, et al.* (2007). Longitudinal, quantitative assessment of amyloid, neuroinflammation, and anti-amyloid treatment in a living mouse model of Alzheimer's disease enabled by positron emission tomography. J Neurosci *27*, 10957-10968.

Maia, L.F., Kaeser, S.A., Reichwald, J., Hruscha, M., Martus, P., Staufenbiel, M., and Jucker, M. (2013). Changes in amyloid-beta and Tau in the cerebrospinal fluid of transgenic mice overexpressing amyloid precursor protein. Sci Transl Med *5*, 194re192.

Maier, F.C., Keller, M.D., Bukala, D., Bender, B., Mannheim, J.G., Brereton, I.M., Galloway, G.J., and Pichler, B.J. (2015). Quantification of β-Amyloidosis and rCBF with Dedicated PET, 7 T MR Imaging, and High-Resolution Microscopic MR Imaging at 16.4 T in APP23 Mice. J Nucl Med *56*, 1593-1599.

Maier, F.C., Wehrl, H.F., Schmid, A.M., Mannheim, J.G., Wiehr, S., Lerdkrai, C., Calaminus, C., Stahlschmidt, A., Ye, L., Burnet, M.*, et al.* (2014). Longitudinal PET-MRI reveals β-amyloid deposition and rCBF dynamics and connects vascular amyloidosis to quantitative loss of perfusion. Nat Med *20*, 1485-1492.

Mancini, S., Minniti, S., Gregori, M., Sancini, G., Cagnotto, A., Couraud, P.O., Ordonez-Gutierrez, L., Wandosell, F., Salmona, M., and Re, F. (2016). The hunt for brain Abeta oligomers by peripherally circulating multi-functional nanoparticles: Potential therapeutic approach for Alzheimer disease. Nanomedicine *12*, 43-52.

Manook, A., Yousefi, B.H., Willuweit, A., Platzer, S., Reder, S., Voss, A., Huisman, M., Settles, M., Neff, F., Velden, J.*, et al.* (2012). Small-Animal PET Imaging of Amyloid-Beta Plaques with [C]PiB and Its Multi-Modal Validation in an APP/PS1 Mouse Model of Alzheimer's Disease. PLoS One *7*, e31310.

Masserini, M. (2013). Nanoparticles for brain drug delivery. ISRN Biochem *2013*, 238428.

Masters, C.L., Simms, G., Weinman, N.A., Multhaup, G., McDonald, B.L., and Beyreuther, K. (1985). Amyloid plaque core protein in Alzheimer disease and Down syndrome. Proc Natl Acad Sci U S A *82*, 4245-4249.

Mathis, C., Lopresti, B., Mason, N., Price, J., Flatt, N., Bi, W., Ziolko, S., DeKosky, S., and Klunk, W. (2007). Comparison of the amyloid imaging agents [F-18]3'-F-PIB and [C-11]PIB in Alzheimer's disease and control subjects. J Nucl Med *48*, 56P.

Mathis, C.A., Bacskai, B.J., Kajdasz, S.T., McLellan, M.E., Frosch, M.P., Hyman, B.T., Holt, D.P., Wang, Y., Huang, G.F., Debnath, M.L.*, et al.* (2002). A lipophilic thioflavin-T derivative for positron emission tomography (PET) imaging of amyloid in brain. Bioorg Med Chem Lett *12*, 295-298.

Mathis, C.A., Holt, D., Wang, Y., Huang, G.-F., Debnath, M., Shao, L., and Klunk, W.E. (2004). Species-dependent formation and identification of the brain metabolites of the amyloid imaging agent [^{11}C]PIB. Neurobiology of ageing *25*, 249.

Mathis, C.A., Wang, Y., Holt, D.P., Huang, G.F., Debnath, M.L., and Klunk, W.E. (2003). Synthesis and evaluation of 11C-labeled 6-substituted 2-arylbenzothiazoles as amyloid imaging agents. J Med Chem *46*, 2740-2754.

Matveev, S.V., Spielmann, H.P., Metts, B.M., Chen, J., Onono, F., Zhu, H., Scheff, S.W., Walker, L.C., and LeVine, H., 3rd (2014). A distinct subfraction of Abeta is responsible for the high-affinity Pittsburgh compound B-binding site in Alzheimer's disease brain. J Neurochem *131*, 356-368.

Maurer, K., Volk, S., and Gerbaldo, H. (1997). Auguste D and Alzheimer's disease. Lancet *349*, 1546-1549.

McKhann, G.M., Knopman, D.S., Chertkow, H., Hyman, B.T., Jack, C.R., Kawas, C.H., Klunk, W.E., Koroshetz, W.J., Manly, J.J., Mayeux, R.*, et al.* (2011). The diagnosis of dementia due to Alzheimer's disease: recommendations from the National Institute on Aging-Alzheimer's Association workgroups on diagnostic guidelines for Alzheimer's disease. Alzheimers Dement *7*, 263-269.

Mills, S.M., Mallmann, J., Santacruz, A.M., Fuqua, A., Carril, M., Aisen, P.S., Althage, M.C., Belyew, S., Benzinger, T.L., Brooks, W.S.*, et al.* (2013). Preclinical trials in autosomal dominant AD: implementation of the DIAN-TU trial. Rev Neurol (Paris) *169*, 737-743.

Minkeviciene, R., Rheims, S., Dobszay, M.B., Zilberter, M., Hartikainen, J., Fülöp, L., Penke, B., Zilberter, Y., Harkany, T., Pitkänen, A.*, et al.* (2009). Amyloid beta-induced neuronal hyperexcitability triggers progressive epilepsy. J Neurosci *29*, 3453-3462.

Minoshima, S., Drzezga, A.E., Barthel, H., Bohnen, N., Djekidel, M., Lewis, D.H., Mathis, C.A., McConathy, J., Nordberg, A., Sabri, O.*, et al.* (2016). SNMMI Procedure Standard/EANM Practice Guideline for Amyloid PET Imaging of the Brain 1.0. J Nucl Med *57*, 1316-1322.

Morris, G.P., Clark, I.A., and Vissel, B. (2014). Inconsistencies and controversies surrounding the amyloid hypothesis of Alzheimer's disease. Acta Neuropathol Commun *2*, 135.

Nelissen, N., Van Laere, K., Thurfjell, L., Owenius, R., Vandenbulcke, M., Koole, M., Bormans, G., Brooks, D.J., and Vandenberghe, R. (2009). Phase 1 study of the Pittsburgh compound B derivative 18F-flutemetamol in healthy volunteers and patients with probable Alzheimer disease. J Nucl Med *50*, 1251-1259.

Nelson, P.T., Alafuzoff, I., Bigio, E.H., Bouras, C., Braak, H., Cairns, N.J., Castellani, R.J., Crain, B.J., Davies, P., Del Tredici, K.*, et al.* (2012). Correlation of Alzheimer disease neuropathologic changes with cognitive status: a review of the literature. J Neuropathol Exp Neurol *71*, 362-381.

Ngandu, T., Lehtisalo, J., Solomon, A., Levälahti, E., Ahtiluoto, S., Antikainen, R., Bäckman, L., Hänninen, T., Jula, A., Laatikainen, T., *et al.* (2015). A 2 year multidomain intervention of diet, exercise, cognitive training, and vascular risk monitoring versus control to prevent cognitive decline in at-risk elderly people (FINGER): a randomised controlled trial. Lancet.

Ni, R., Gillberg, P.G., Bergfors, A., Marutle, A., and Nordberg, A. (2013). Amyloid tracers detect multiple binding sites in Alzheimer's disease brain tissue. Brain *136*, 2217-2227.

Nilsson, P., Saito, T., and Saido, T.C. (2014). New mouse model of Alzheimer's. ACS Chem Neurosci *5*, 499-502.

Norton, S., Matthews, F.E., Barnes, D.E., Yaffe, K., and Brayne, C. (2014). Potential for primary prevention of Alzheimer's disease: an analysis of population-based data. Lancet Neurol *13*, 788-794.

Nyberg, S., Jonhagen, M.E., Cselenyi, Z., Halldin, C., Julin, P., Olsson, H., Freund-Levi, Y., Andersson, J., Varnas, K., Svensson, S., *et al.* (2009). Detection of amyloid in Alzheimer's disease with positron emission tomography using [11C]AZD2184. Eur J Nucl Med Mol Imaging *36*, 1859-1863.

O'Keefe, G.J., Saunder, T.H., Ng, S., Ackerman, U., Tochon-Danguy, H.J., Chan, J.G., Gong, S., Dyrks, T., Lindemann, S., Holl, G., *et al.* (2009). Radiation dosimetry of beta-amyloid tracers 11C-PiB and 18F-BAY94-9172. J Nucl Med *50*, 309-315.

Oakley, H., Cole, S.L., Logan, S., Maus, E., Shao, P., Craft, J., Guillozet-Bongaarts, A., Ohno, M., Disterhoft, J., Van Eldik, L., *et al.* (2006). Intraneuronal beta-amyloid aggregates, neurodegeneration, and neuron loss in transgenic mice with five familial Alzheimer's disease mutations: potential factors in amyloid plaque formation. J Neurosci *26*, 10129-10140.

Oddo, S., Caccamo, A., Shepherd, J.D., Murphy, M.P., Golde, T.E., Kayed, R., Metherate, R., Mattson, M.P., Akbari, Y., and LaFerla, F.M. (2003). Triple-transgenic model of Alzheimer's disease with plaques and tangles: intracellular Abeta and synaptic dysfunction. Neuron *39*, 409-421.

Ono, M., Wilson, A., Nobrega, J., Westaway, D., Verhoeff, P., Zhuang, Z.P., Kung, M.P., and Kung, H.F. (2003). 11C-labeled stilbene derivatives as Abeta-aggregate-specific PET imaging agents for Alzheimer's disease. Nucl Med Biol *30*, 565-571.

Orgogozo, J.M., Gilman, S., Dartigues, J.F., Laurent, B., Puel, M., Kirby, L.C., Jouanny, P., Dubois, B., Eisner, L., Flitman, S., *et al.* (2003). Subacute meningoencephalitis in a subset of patients with AD after Abeta42 immunization. Neurology *61*, 46-54.

Ossenkoppele, R., Tolboom, N., Foster-Dingley, J.C., Adriaanse, S.F., Boellaard, R., Yaqub, M., Windhorst, A.D., Barkhof, F., Lammertsma, A.A., Scheltens, P., *et al.* (2012). Longitudinal imaging of Alzheimer pathology using [11C]PIB, [18F]FDDNP and [18F]FDG PET. Eur J Nucl Med Mol Imaging *39*, 990-1000.

Ostrowitzki, S., Deptula, D., Thurfjell, L., Barkhof, F., Bohrmann, B., Brooks, D.J., Klunk, W.E., Ashford, E., Yoo, K., Xu, Z.X., *et al.* (2012). Mechanism of amyloid removal in patients with Alzheimer disease treated with gantenerumab. Arch Neurol *69*, 198-207.

Ott, A., Stolk, R.P., van Harskamp, F., Pols, H.A., Hofman, A., and Breteler, M.M. (1999). Diabetes mellitus and the risk of dementia: The Rotterdam Study. Neurology *53*, 1937-1942.

Overhoff, F., Brendel, M., Jaworska, A., Korzhova, V., Delker, A., Probst, F., Focke, C., Gildehaus, F.J., Carlsen, J., Baumann, K., *et al.* (2016). Automated Spatial Brain Normalization and Hindbrain White Matter Reference Tissue Give Improved [(18)F]-Florbetaben PET Quantitation in Alzheimer's Model Mice. Front Neurosci *10*, 45.

Ozmen, L., Albientz, A., Czech, C., and Jacobsen, H. (2009). Expression of transgenic APP mRNA is the key determinant for beta-amyloid deposition in PS2APP transgenic mice. Neurodegener Dis *6*, 29-36.

Parsey, R.V., Sokol, L.O., Bélanger, M.J., Kumar, J.S., Simpson, N.R., Wang, T., Pratap, M., Van Heertum, R.L., and John Mann, J. (2005). Amyloid plaque imaging agent [C-11]-6-OH-BTA-1: biodistribution and radiation dosimetry in baboon. Nucl Med Commun *26*, 875-880.

Phelps, M.E. (2000). Positron emission tomography provides molecular imaging of biological processes. Proc Natl Acad Sci U S A *97*, 9226-9233.

Poisnel, G., Dhilly, M., Moustié, O., Delamare, J., Abbas, A., Guilloteau, D., and Barré, L. (2012). PET imaging with [18F]AV-45 in an APP/PS1-21 murine model of amyloid plaque deposition. Neurobiol Aging *33*, 2561-2571.

Poorkaj, P., Bird, T.D., Wijsman, E., Nemens, E., Garruto, R.M., Anderson, L., Andreadis, A., Wiederholt, W.C., Raskind, M., and Schellenberg, G.D. (1998). Tau is a candidate gene for chromosome 17 frontotemporal dementia. Ann Neurol *43*, 815-825.

Prince, M., Bryce, R., Albanese, E., Wimo, A., Ribeiro, W., and Ferri, C.P. (2013). The global prevalence of dementia: a systematic review and metaanalysis. Alzheimers Dement *9*, 63-75.e62.

Prince, M., Bryce, R., and Ferri, C. (2011). World Alzheimer Report 2011: The benefits of early diagnosis and intervention, A.d. international, ed. (Alzheimers disease international).

Radde, R., Bolmont, T., Kaeser, S.A., Coomaraswamy, J., Lindau, D., Stoltze, L., Calhoun, M.E., Jaggi, F., Wolburg, H., Gengler, S., *et al.* (2006). Abeta42-driven cerebral amyloidosis in transgenic mice reveals early and robust pathology. EMBO Rep *7*, 940-946.

Rahmim, A., and Zaidi, H. (2008). PET versus SPECT: strengths, limitations and challenges. Nucl Med Commun *29*, 193-207.

Re, F., Cambianica, I., Sesana, S., Salvati, E., Cagnotto, A., Salmona, M., Couraud, P.O., Moghimi, S.M., Masserini,

M., and Sancini, G. (2010). Functionalization with ApoE-derived peptides enhances the interaction with brain capillary endothelial cells of nanoliposomes binding amyloid-beta peptide. J Biotechnol *156*, 341-346.

Re, F., Cambianica, I., Zona, C., Sesana, S., Gregori, M., Rigolio, R., La Ferla, B., Nicotra, F., Forloni, G., Cagnotto, A.*, et al.* (2011). Functionalization of liposomes with ApoE-derived peptides at different density affects cellular uptake and drug transport across a blood-brain barrier model. Nanomedicine *7*, 551-559.

Re, F., Gregori, M., and Masserini, M. (2012). Nanotechnology for neurodegenerative disorders. Nanomedicine *8 Suppl 1*, S51-58.

Reiman, E.M., Langbaum, J.B., Fleisher, A.S., Caselli, R.J., Chen, K., Ayutyanont, N., Quiroz, Y.T., Kosik, K.S., Lopera, F., and Tariot, P.N. (2011). Alzheimer's Prevention Initiative: a plan to accelerate the evaluation of presymptomatic treatments. J Alzheimers Dis *26 Suppl 3*, 321-329.

Reitz, C., and Mayeux, R. (2014). Alzheimer disease: epidemiology, diagnostic criteria, risk factors and biomarkers. Biochem Pharmacol *88*, 640-651.

Richards, J.G., Higgins, G.A., Ouagazzal, A.M., Ozmen, L., Kew, J.N., Bohrmann, B., Malherbe, P., Brockhaus, M., Loetscher, H., Czech, C.*, et al.* (2003). PS2APP transgenic mice, coexpressing hPS2mut and hAPPswe, show age-related cognitive deficits associated with discrete brain amyloid deposition and inflammation. J Neurosci *23*, 8989-9003.

Rinne, J.O., Brooks, D.J., Rossor, M.N., Fox, N.C., Bullock, R., Klunk, W.E., Mathis, C.A., Blennow, K., Barakos, J., Okello, A.A.*, et al.* (2010). 11C-PiB PET assessment of change in fibrillar amyloid-beta load in patients with Alzheimer's disease treated with bapineuzumab: a phase 2, double-blind, placebo-controlled, ascending-dose study. Lancet Neurol *9*, 363-372.

Rinne, J.O., Frantzen, J., Leinonen, V., Lonnrot, K., Laakso, A., Virtanen, K.A., Solin, O., Kotkansalo, A., Koivisto, A., Sajanti, J.*, et al.* (2013). Prospective Flutemetamol Positron Emission Tomography and Histopathology in Normal Pressure Hydrocephalus. Neurodegener Dis.

Rinne, J.O., Wong, D.F., Wolk, D.A., Leinonen, V., Arnold, S.E., Buckley, C., Smith, A., McLain, R., Sherwin, P.F., Farrar, G.*, et al.* (2012). [(18)F]Flutemetamol PET imaging and cortical biopsy histopathology for fibrillar amyloid β detection in living subjects with normal pressure hydrocephalus: pooled analysis of four studies. Acta Neuropathol *124*, 833-845.

Rodrigue, K.M., Kennedy, K.M., Devous, M.D., Rieck, J.R., Hebrank, A.C., Diaz-Arrastia, R., Mathews, D., and Park, D.C. (2012). β-Amyloid burden in healthy aging: regional distribution and cognitive consequences. Neurology *78*, 387-395.

Rojas, S., Herance, J.R., Gispert, J.D., Abad, S., Torrent, E., Jimenez, X., Pareto, D., Perpina, U., Sarroca, S., Rodriguez, E.*, et al.* (2013). In vivo evaluation of amyloid deposition and brain glucose metabolism of 5XFAD mice using positron emission tomography. Neurobiol Aging *34*, 1790-1798.

Rominger, A., Brendel, M., Burgold, S., Keppler, K., Baumann, K., Xiong, G., Mille, E., Gildehaus, F.J., Carlsen, J., Schlichtiger, J.*, et al.* (2013). Longitudinal assessment of cerebral β-amyloid deposition in mice overexpressing Swedish mutant β-amyloid precursor protein using 18F-florbetaben PET. J Nucl Med *54*, 1127-1134.

Rosenthal, S.L., and Kamboh, M.I. (2014). Late-Onset Alzheimer's Disease Genes and the Potentially Implicated Pathways. In Curr Genet Med Rep (United States), pp. 85-101.

Rossjohn, J., Cappai, R., Feil, S.C., Henry, A., McKinstry, W.J., Galatis, D., Hesse, L., Multhaup, G., Beyreuther, K., Masters, C.L.*, et al.* (1999). Crystal structure of the N-terminal, growth factor-like domain of Alzheimer amyloid precursor protein. Nat Struct Biol *6*, 327-331.

Rowe, C.C., Ackerman, U., Browne, W., Mulligan, R., Pike, K.L., O'Keefe, G., Tochon-Danguy, H., Chan, G., Berlangieri, S.U., Jones, G.*, et al.* (2008). Imaging of amyloid beta in Alzheimer's disease with 18F-BAY94-9172, a novel PET tracer: proof of mechanism. Lancet Neurol *7*, 129-135.

Rowe, C.C., Pejoska, S., Mulligan, R.S., Jones, G., Chan, J.G., Svensson, S., Cselényi, Z., Masters, C.L., and Villemagne, V.L. (2013). Head-to-head comparison of 11C-PiB and 18F-AZD4694 (NAV4694) for β-amyloid imaging in aging and dementia. J Nucl Med *54*, 880-886.

Saito, T., Matsuba, Y., Mihira, N., Takano, J., Nilsson, P., Itohara, S., Iwata, N., and Saido, T.C. (2014). Single App knock-in mouse models of Alzheimer's disease. Nat Neurosci *17*, 661-663.

Salloway, S., Sperling, R., Fox, N.C., Blennow, K., Klunk, W., Raskind, M., Sabbagh, M., Honig, L.S., Porsteinsson, A.P., Ferris, S.*, et al.* (2014). Two phase 3 trials of bapineuzumab in mild-to-moderate Alzheimer's disease. N Engl J Med *370*, 322-333.

Saraiva, C., Praça, C., Ferreira, R., Santos, T., Ferreira, L., and Bernardino, L. (2016). Nanoparticle-mediated brain drug delivery: Overcoming blood-brain barrier to treat neurodegenerative diseases. J Control Release *235*, 34-47.

Savonenko, A., Xu, G.M., Melnikova, T., Morton, J.L., Gonzales, V., Wong, M.P., Price, D.L., Tang, F., Markowska, A.L., and Borchelt, D.R. (2005). Episodic-like memory deficits in the APPswe/PS1dE9 mouse model of Alzheimer's disease: relationships to beta-amyloid deposition and neurotransmitter abnormalities. Neurobiol Dis *18*, 602-617.

Scheinin, N.M., Aalto, S., Koikkalainen, J., Lötjönen, J., Karrasch, M., Kemppainen, N., Viitanen, M., Någren, K., Helin, S., Scheinin, M.*, et al.* (2009). Follow-up of [11C]PIB uptake and brain volume in patients with

Alzheimer disease and controls. Neurology *73*, 1186-1192.

Scheinin, N.M., Tolvanen, T.K., Wilson, I.A., Arponen, E.M., Någren, K.A., and Rinne, J.O. (2007). Biodistribution and radiation dosimetry of the amyloid imaging agent 11C-PIB in humans. J Nucl Med *48*, 128-133.

Schneider, L.S., Mangialasche, F., Andreasen, N., Feldman, H., Giacobini, E., Jones, R., Mantua, V., Mecocci, P., Pani, L., Winblad, B.*, et al.* (2014). Clinical trials and late-stage drug development for Alzheimer's disease: an appraisal from 1984 to 2014. J Intern Med *275*, 251-283.

Selkoe, D.J., and Hardy, J. (2016). The amyloid hypothesis of Alzheimer's disease at 25 years. EMBO Mol Med *8*, 595-608.

Sevigny, J., Chiao, P., Bussière, T., Weinreb, P.H., Williams, L., Maier, M., Dunstan, R., Salloway, S., Chen, T., Ling, Y.*, et al.* (2016). The antibody aducanumab reduces Aβ plaques in Alzheimer's disease. Nature *537*, 50-56.

Sherrington, R., Rogaev, E.I., Liang, Y., Rogaeva, E.A., Levesque, G., Ikeda, M., Chi, H., Lin, C., Li, G., Holman, K.*, et al.* (1995). Cloning of a gene bearing missense mutations in early-onset familial Alzheimer's disease. Nature *375*, 754-760.

Shibata, M., Yamada, S., Kumar, S.R., Calero, M., Bading, J., Frangione, B., Holtzman, D.M., Miller, C.A., Strickland, D.K., Ghiso, J.*, et al.* (2000). Clearance of Alzheimer's amyloid-ss(1-40) peptide from brain by LDL receptor-related protein-1 at the blood-brain barrier. J Clin Invest *106*, 1489-1499.

Shoghi-Jadid, K., Small, G.W., Agdeppa, E.D., Kepe, V., Ercoli, L.M., Siddarth, P., Read, S., Satyamurthy, N., Petric, A., Huang, S.C.*, et al.* (2002). Localization of neurofibrillary tangles and beta-amyloid plaques in the brains of living patients with Alzheimer disease. Am J Geriatr Psychiatry *10*, 24-35.

Sindi, S., Mangialasche, F., and Kivipelto, M. (2015). Advances in the prevention of Alzheimer's Disease. F1000Prime Rep *7*, 50.

Small, G.W., Kepe, V., Ercoli, L.M., Siddarth, P., Bookheimer, S.Y., Miller, K.J., Lavretsky, H., Burggren, A.C., Cole, G.M., Vinters, H.V.*, et al.* (2006). PET of brain amyloid and tau in mild cognitive impairment. N Engl J Med *355*, 2652-2663.

Sperling, R.A., Jack, C.R., and Aisen, P.S. (2011). Testing the right target and right drug at the right stage. Sci Transl Med *3*, 111cm133.

Sperling, R.A., Rentz, D.M., Johnson, K.A., Karlawish, J., Donohue, M., Salmon, D.P., and Aisen, P. (2014). The A4 study: stopping AD before symptoms begin? Sci Transl Med *6*, 228fs213.

Stankoff, B., Freeman, L., Aigrot, M.S., Chardain, A., Dolle, F., Williams, A., Galanaud, D., Armand, L., Lehericy, S., Lubetzki, C.*, et al.* (2011). Imaging central nervous system myelin by positron emission tomography in multiple sclerosis using [methyl-(1)(1)C]-2-(4'-methylaminophenyl)- 6-hydroxybenzothiazole. Ann Neurol *69*, 673-680.

Sturchler-Pierrat, C., Abramowski, D., Duke, M., Wiederhold, K.H., Mistl, C., Rothacher, S., Ledermann, B., Bürki, K., Frey, P., Paganetti, P.A.*, et al.* (1997). Two amyloid precursor protein transgenic mouse models with Alzheimer disease-like pathology. Proc Natl Acad Sci U S A *94*, 13287-13292.

Sturchler-Pierrat, C., and Staufenbiel, M. (2000). Pathogenic mechanisms of Alzheimer's disease analyzed in the APP23 transgenic mouse model. Ann N Y Acad Sci *920*, 134-139.

Syvanen, S., Fang, X.T., Hultqvist, G., Meier, S.R., Lannfelt, L., and Sehlin, D. (2017). A bispecific Tribody PET radioligand for visualization of amyloid-beta protofibrils - a new concept for neuroimaging. Neuroimage *148*, 55-63.

Sérrière, S., Tauber, C., Vercouillie, J., Mothes, C., Pruckner, C., Guilloteau, D., Kassiou, M., Doméné, A., Garreau, L., Page, G.*, et al.* (2015). Amyloid load and translocator protein 18 kDa in APPswePS1-dE9 mice: a longitudinal study. Neurobiol Aging.

Takeuchi, A., Irizarry, M.C., Duff, K., Saido, T.C., Hsiao Ashe, K., Hasegawa, M., Mann, D.M., Hyman, B.T., and Iwatsubo, T. (2000). Age-related amyloid beta deposition in transgenic mice overexpressing both Alzheimer mutant presenilin 1 and amyloid beta precursor protein Swedish mutant is not associated with global neuronal loss. Am J Pathol *157*, 331-339.

Tapiola, T., Alafuzoff, I., Herukka, S.K., Parkkinen, L., Hartikainen, P., Soininen, H., and Pirttila, T. (2009). Cerebrospinal fluid {beta}-amyloid 42 and tau proteins as biomarkers of Alzheimer-type pathologic changes in the brain. Arch Neurol *66*, 382-389.

Teng, E., Kepe, V., Frautschy, S.A., Liu, J., Satyamurthy, N., Yang, F., Chen, P.P., Cole, G.B., Jones, M.R., Huang, S.C.*, et al.* (2011). [F-18]FDDNP microPET imaging correlates with brain Abeta burden in a transgenic rat model of Alzheimer disease: effects of aging, in vivo blockade, and anti-Abeta antibody treatment. Neurobiol Dis *43*, 565-575.

Thal, D.R., Rub, U., Orantes, M., and Braak, H. (2002). Phases of A beta-deposition in the human brain and its relevance for the development of AD. Neurology *58*, 1791-1800.

Thompson, P.M., Hayashi, K.M., de Zubicaray, G., Janke, A.L., Rose, S.E., Semple, J., Herman, D., Hong, M.S., Dittmer, S.S., Doddrell, D.M.*, et al.* (2003). Dynamics of gray matter loss in Alzheimer's disease. J Neurosci *23*, 994-1005.

Tomlinson, B.E., Blessed, G., and Roth, M. (1968). Observations on the brains of non-demented old people. J Neurol Sci *7*, 331-356.

Toyama, H., Ye, D., Ichise, M., Liow, J.S., Cai, L., Jacobowitz, D., Musachio, J.L., Hong, J., Crescenzo, M., Tipre, D., *et al.* (2005). PET imaging of brain with the beta-amyloid probe, [11C]6-OH-BTA-1, in a transgenic mouse model of Alzheimer's disease. Eur J Nucl Med Mol Imaging *32*, 593-600.

Van Dam, D., D'Hooge, R., Staufenbiel, M., Van Ginneken, C., Van Meir, F., and De Deyn, P.P. (2003). Age-dependent cognitive decline in the APP23 model precedes amyloid deposition. Eur J Neurosci *17*, 388-396.

Van Dam, D., and De Deyn, P.P. (2011). Animal models in the drug discovery pipeline for Alzheimer's disease. Br J Pharmacol *164*, 1285-1300.

van der Have, F., Vastenhouw, B., Ramakers, R.M., Branderhorst, W., Krah, J.O., Ji, C., Staelens, S.G., and Beekman, F.J. (2009). U-SPECT-II: An Ultra-High-Resolution Device for Molecular Small-Animal Imaging. J Nucl Med *50*, 599-605.

Vandenberghe, R., Van Laere, K., Ivanoiu, A., Salmon, E., Bastin, C., Triau, E., Hasselbalch, S., Law, I., Andersen, A., Korner, A., *et al.* (2010). 18F-flutemetamol amyloid imaging in Alzheimer disease and mild cognitive impairment: a phase 2 trial. Ann Neurol *68*, 319-329.

Vellas, B., Carrie, I., Gillette-Guyonnet, S., Touchon, J., Dantoine, T., Dartigues, J.F., Cuffi, M.N., Bordes, S., Gasnier, Y., Robert, P., *et al.* (2014). MAPT STUDY: A MULTIDOMAIN APPROACH FOR PREVENTING ALZHEIMER'S DISEASE: DESIGN AND BASELINE DATA. J Prev Alzheimers Dis *1*, 13-22.

Verhoeff, N.P., Wilson, A.A., Takeshita, S., Trop, L., Hussey, D., Singh, K., Kung, H.F., Kung, M.P., and Houle, S. (2004). In-vivo imaging of Alzheimer disease beta-amyloid with [11C]SB-13 PET. Am J Geriatr Psychiatry *12*, 584-595.

Vieira, D.B., and Gamarra, L.F. (2016). Getting into the brain: liposome-based strategies for effective drug delivery across the blood-brain barrier. Int J Nanomedicine *11*, 5381-5414.

Villemagne, V.L., Mulligan, R.S., Pejoska, S., Ong, K., Jones, G., O'Keefe, G., Chan, J.G., Young, K., Tochon-Danguy, H., Masters, C.L., *et al.* (2012). Comparison of 11C-PiB and 18F-florbetaben for Aβ imaging in ageing and Alzheimer's disease. Eur J Nucl Med Mol Imaging *39*, 983-989.

von Reutern, B., Grünecker, B., Yousefi, B.H., Henriksen, G., Czisch, M., and Drzezga, A. (2013). Voxel-based analysis of amyloid-burden measured with [(11)C]PiB PET in a double transgenic mouse model of Alzheimer's disease. Mol Imaging Biol *15*, 576-584.

Waldron, A.M., Verhaeghe, J., wyffels, L., Schmidt, M., Langlois, X., Van Der Linden, A., Stroobants, S., and Staelens, S. (2015). Preclinical Comparison of the Amyloid-beta Radioligands [(11)C]Pittsburgh compound B and [(18)F]florbetaben in Aged APPPS1-21 and BRI1-42 Mouse Models of Cerebral Amyloidosis. Mol Imaging Biol *17*, 688-696.

Walsh, D.M., Klyubin, I., Fadeeva, J.V., Cullen, W.K., Anwyl, R., Wolfe, M.S., Rowan, M.J., and Selkoe, D.J. (2002). Naturally secreted oligomers of amyloid beta protein potently inhibit hippocampal long-term potentiation in vivo. Nature *416*, 535-539.

Walti, M.A., Ravotti, F., Arai, H., Glabe, C.G., Wall, J.S., Bockmann, A., Guntert, P., Meier, B.H., and Riek, R. (2016). Atomic-resolution structure of a disease-relevant Abeta(1-42) amyloid fibril. Proc Natl Acad Sci U S A *113*, E4976-4984.

Waterhouse, R.N. (2003). Determination of lipophilicity and its use as a predictor of blood-brain barrier penetration of molecular imaging agents. Mol Imaging Biol *5*, 376-389.

Weissler, B., Gebhardt, P., Dueppenbecker, P.M., Wehner, J., Schug, D., Lerche, C.W., Goldschmidt, B., Salomon, A., Verel, I., Heijman, E., *et al.* (2015). A Digital Preclinical PET/MRI Insert and Initial Results. IEEE Trans Med Imaging *34*, 2258-2270.

Whitwell, J.L., Josephs, K.A., Murray, M.E., Kantarci, K., Przybelski, S.A., Weigand, S.D., Vemuri, P., Senjem, M.L., Parisi, J.E., Knopman, D.S., *et al.* (2008). MRI correlates of neurofibrillary tangle pathology at autopsy: a voxel-based morphometry study. Neurology *71*, 743-749.

Wilcock, G.K. (2003). Memantine for the treatment of dementia. Lancet Neurol *2*, 503-505.

Willuweit, A., Velden, J., Godemann, R., Manook, A., Jetzek, F., Tintrup, H., Kauselmann, G., Zevnik, B., Henriksen, G., Drzezga, A., *et al.* (2009). Early-onset and robust amyloid pathology in a new homozygous mouse model of Alzheimer's disease. PLoS One *4*, e7931.

Wilson, B., Samanta, M.K., Santhi, K., Kumar, K.P., Paramakrishnan, N., and Suresh, B. (2008). Poly(n-butylcyanoacrylate) nanoparticles coated with polysorbate 80 for the targeted delivery of rivastigmine into the brain to treat Alzheimer's disease. Brain Res *1200*, 159-168.

Wimo, A., Ballard, C., Brayne, C., Gauthier, S., Handels, R., Jones, R.W., Jonsson, L., Khachaturian, A.S., and Kramberger, M. (2014). Health economic evaluation of treatments for Alzheimer's disease: impact of new diagnostic criteria. J Intern Med *275*, 304-316.

Winkler, D.T., Bondolfi, L., Herzig, M.C., Jann, L., Calhoun, M.E., Wiederhold, K.H., Tolnay, M., Staufenbiel, M., and Jucker, M. (2001). Spontaneous hemorrhagic stroke in a mouse model of cerebral amyloid angiopathy. J Neurosci *21*, 1619-1627.

Wisniewski, T., Ghiso, J., and Frangione, B. (1991). Peptides homologous to the amyloid protein of Alzheimer's disease containing a glutamine for glutamic acid substitution have accelerated amyloid fibril formation. Biochem Biophys Res Commun *179*, 1247-1254.

Wolk, D.A., Grachev, I.D., Buckley, C., Kazi, H., Grady, M.S., Trojanowski, J.Q., Hamilton, R.H., Sherwin, P.,

McLain, R., and Arnold, S.E. (2011). Association between in vivo fluorine 18-labeled flutemetamol amyloid positron emission tomography imaging and in vivo cerebral cortical histopathology. Arch Neurol *68*, 1398-1403.

Wong, D.F., Moghekar, A.R., Rigamonti, D., Brašić, J.R., Rousset, O., Willis, W., Buckley, C., Smith, A., Gok, B., Sherwin, P.*, et al.* (2013). An in vivo evaluation of cerebral cortical amyloid with [18F]flutemetamol using positron emission tomography compared with parietal biopsy samples in living normal pressure hydrocephalus patients. Mol Imaging Biol *15*, 230-237.

Wong, D.F., Rosenberg, P.B., Zhou, Y., Kumar, A., Raymont, V., Ravert, H.T., Dannals, R.F., Nandi, A., Brasić, J.R., Ye, W.*, et al.* (2010). In vivo imaging of amyloid deposition in Alzheimer disease using the radioligand 18F-AV-45 (florbetapir [corrected] F 18). J Nucl Med *51*, 913-920.

Zhang, W., Oya, S., Kung, M.P., Hou, C., Maier, D.L., and Kung, H.F. (2005). F-18 Polyethyleneglycol stilbenes as PET imaging agents targeting Abeta aggregates in the brain. Nucl Med Biol *32*, 799-809.

Ziegler, S. (2011). PET and SPECT. In Small Animal Imaging Basics and Practical Guide, F. Kiessling, B. Pichler, and P. Hauff, eds. (Berlin-Heidelberg: Springer).

Annales Universitatis Turkuensis

Turun yliopisto
University of Turku

ISBN 978-951-29-6865-7 (PRINT)
ISBN 978-951-29-6866-4 (PDF)
ISSN 0355-9483 (Print) | ISSN 2343-3213 (Online)

Painosalama Oy, Turku, Finland 2017